

UV Curing and Micromolding of Polymer Coatings

A DISSERTATION
SUBMITTED TO THE FACULTY OF THE GRADUATE SCHOOL
OF THE UNIVERSITY OF MINNESOTA
BY

Yuyang Du

IN PARTIAL FULFILLMENT OF THE REQUIREMENTS
FOR THE DEGREE OF
DOCTOR OF PHILOSOPHY

Lorraine F. Francis and Alon V. McCormick, Advisors

August 2018

© Yuyang Du 2018

Acknowledgments

I would like to begin by thanking my advisors, Lorraine Francis and Alon McCormick for their advice, guidance, and support. I am thankful to them for letting me join their groups in the first place, helping me become an independent researcher, and giving me support in developing my career. I could not have completed my research without their encouragement and efforts during this great period of personal growth. I would also like to gratefully acknowledge the Industrial Partnership for Research in Interfacial and Materials Engineering (IPRIME) for financial support of this project. Parts of this work were performed at the Nano-Fabrication Center and the Characterization Facility, the University of Minnesota, which receives partial support from NSF through the MRSEC program.

I would also like to thank the members of the Francis Research Group, the McCormick Research Group, and the Coating Process Fundamentals Program. They are invaluable to the success of my research. Specially acknowledgments go to my colleagues: Kyle Price, Bryce Williams, Tuoqi Li, David Riehm, Ankit Mahajan, Woo Jin Hyun, Yan Wu, Robert Lade, Motao Cao, Noah Holzman. I appreciated the help of undergrad researchers working with me: John Sakizadeh, Donovan Weiblen, Nitika Thakral, and Danish Syed. I would also like to thank Rui Ding for his nice contribution to the 3D printable UV system and thank Krystopher Jochem for his great help with the roll-to-roll experiments. Thanks to Dr. David Giles and Dr. Wieslaw Suzynski for their advice and support in designing rheological measurements and coating processes, respectively.

Finally, I would like to thank my friends and family for being by my side throughout this journey. Special thanks go to Jun, Motao, Tianqi, Qile, Tuoqi, Lian, Yiming, Yan, En, Hongyun, Han, and Kailong. Thank you all for making grad school a memorable experience for me. Whole-hearted thanks to my host

family, Sue & Pete, for making me feel at home. To my family, I owe much of my success to you for your love with no conditions and for your faith in me.

Abstract

UV curable films and coatings have a wide range of applications in everyday life and various industrial sectors. With surface microstructures, patterned coatings can be used as a general way to provide surface textures or serve critical design purposes, such as providing engineered optical performances and altering the surface hydrophobicity. This thesis addresses key challenges in the UV curing process and their patterning applications, aiming to make UV curing faster, better, and cheaper.

Firstly, the UV curing speed is the bottleneck of the process throughput for many applications. Traditionally, high-intensity light sources are used to achieve fast cure but bring with potential problems, e.g. significant heat accumulation. In this thesis, the intense pulsed light was investigated as an alternative curing method, where the UV energy is delivered in discrete pulses with a dark period between pulses. A systematic study was performed on a model acrylate system to understand the curing conversion as a function of various processing parameter, including illumination conditions, the photoinitiator concentration, and the curing temperature. It was revealed that sufficient curing of acrylates was achieved within seconds without significant heat built-up in the substrate.

Second, this thesis investigates the fabrication of surface microstructures with UV curable materials. The UV micromolding process is used for pattern replication, where a liquid coating is brought into contact with a patterned mold and then UV cured to obtain surface microstructures. However, the wide application of this process is limited the stringent material requirements of the process: low viscosities, fast cure, low surface energy, and tunable mechanical properties. This thesis describes the design of thiol-ene based coating formulations for the UV micromolding process. The coating system allows for

the preparation of microstructured coatings within seconds and significantly expands the achievable mechanical and surface properties of cured materials.

Finally, continuous fabrication of microstructured coatings was explored to move the process a step further towards mass production. The roll-to-roll imprinting process with thiol-ene based formulations was discussed. In the process, a roller mold was used for pattern replication on large-area substrates. The coating formulations were optimized for a fast cure and high curing extents. In addition, the influences of processing variables on the curing extents were studied systematically.

Table of Contents

1	Introduction.....	1
1.1	Motivation.....	1
1.2	Thesis outline	3
2	Background Information	6
2.1	UV curable systems	6
2.1.1	<i>Free Radical Photopolymerization</i>	<i>6</i>
2.1.2	<i>Cationic Photopolymerization</i>	<i>9</i>
2.1.3	<i>Thiol-ene reaction</i>	<i>10</i>
2.2	Photopolymerization kinetics.....	11
2.2.1	<i>Basic process</i>	<i>11</i>
2.2.2	<i>Initiation Efficiency.....</i>	<i>12</i>
2.2.3	<i>Curing speed</i>	<i>14</i>
2.2.4	<i>Achievable conversion</i>	<i>15</i>
2.2.5	<i>Influence of atmospheric oxygen</i>	<i>17</i>
2.3	Surface Replication Technologies	18
2.3.1	<i>Applications of microstructured coatings and films</i>	<i>19</i>
2.3.2	<i>Overview of surface replication techniques.....</i>	<i>21</i>
3	Pulsed Irradiation for High-throughput Curing Applications*.....	25
3.1	Background and Motivation	25

3.2	Experimental.....	28
3.2.1	<i>Materials</i>	28
3.2.2	<i>Curing Conditions</i>	29
3.2.3	<i>Conversion Measurement</i>	30
3.2.4	<i>Heat Transfer Analysis</i>	34
3.2.5	<i>UV-Vis spectroscopy</i>	35
3.3	Results and Discussion	36
3.3.1	<i>Comparison of acrylate and epoxy curing kinetics with a mercury lamp</i> 36	
3.3.2	<i>Single pulse curing</i>	38
3.3.3	<i>Multiple pulse curing</i>	41
3.3.4	<i>Effects of irradiation dose rate</i>	43
3.3.5	<i>Effects of PI concentration</i>	45
3.3.6	<i>Effects of temperature</i>	47
3.3.7	<i>PI Consumption</i>	49
3.3.8	<i>Depthwise curing gradient</i>	51
3.4	Summary	53
4	Modulus- and Surface Energy-Tunable Thiol-ene for UV Micromolding of Coatings*	55
4.1	Background and Motivation	55

4.3	Materials and Methods.....	60
4.3.1	<i>Thiol-Ene-Acrylate Coating Formulation.....</i>	<i>60</i>
4.3.2	<i>Coating Formulation Preparation.....</i>	<i>61</i>
4.3.3	<i>Synthesis of F-PMMA</i>	<i>62</i>
4.3.4	<i>Kinetic Analysis</i>	<i>62</i>
4.3.5	<i>Analyses of Cured Materials Properties.....</i>	<i>63</i>
4.3.6	<i>Mold Fabrication.....</i>	<i>65</i>
4.3.7	<i>Micromolding Experiments.....</i>	<i>67</i>
4.3.8	<i>Patterned Coating Imaging.....</i>	<i>68</i>
4.3.9	<i>Peel Strength Measurement.....</i>	<i>68</i>
4.4	Results and Discussion	70
4.4.1	<i>Photopolymerization Kinetics.....</i>	<i>70</i>
4.4.2	<i>Tunability of Thermomechanical Properties</i>	<i>73</i>
4.4.3	<i>Surface Energy Reduction.....</i>	<i>77</i>
4.4.4	<i>Thermal stability of thiol-ene(-acrylate) coatings</i>	<i>82</i>
4.4.5	<i>Pattern Fidelity</i>	<i>84</i>
4.4.6	<i>Demolding Analysis</i>	<i>87</i>
4.4.7	<i>One illustration of the promise of this approach: fabricating superhydrophobic microstructured TEF coatings</i>	<i>92</i>
4.5	Summary	94

5	Roll-to-Roll Micromolding of UV Curable Coatings	95
5.1	Background and Motivation	95
5.2	Materials and Methods.....	98
5.2.1	<i>Materials</i>	98
5.2.2	<i>Dynamic Viscosity Measurement</i>	99
5.2.3	<i>FTIR spectroscopy</i>	99
5.2.4	<i>Photo-rheology measurement</i>	100
5.2.5	<i>Dynamic mechanical analysis</i>	101
5.2.6	<i>Preparation of roller mold</i>	101
5.2.7	<i>Roll-to-roll imprinting line operation</i>	103
5.3	Results and Discussion	103
5.3.1	<i>Characteristics of Liquid Formulations</i>	105
5.3.2	<i>Curing kinetics</i>	106
5.3.3	<i>Mechanical properties of cured materials</i>	112
5.4	R2R UV Imprinting	114
5.4.1	<i>Effects of thiol and oligomer contents on conversions</i>	114
5.5	Summary	124
6	Summary and Future Directions.....	125
6.1	Summary	125
6.2	Future Directions	127

6.2.1	<i>Metal-polymer nanocomposite</i>	127
6.2.2	<i>Inorganic-organic hybrid materials</i>	128
6.2.3	<i>Fluorinated mold materials</i>	129
6.2.4	<i>Multilevel patterns</i>	130
7	References	131

LIST OF TABLES

Table 2.1 Different types of UV-curable resins.....	7
Table 3.1 Hypothesis tests for the equality of sample means of single pulse curing (SP) and multiple pulse curing (MP) at different net illumination times (t).....	42
Table 3.2 Base case experimental conditions	43
Table 3.3 Irradiation dose rate and achievable conversion.....	43
Table 4.1 Composition of coating formulations	61
Table 4.2 Thermomechanical properties of UV-cured thiol-ene(-acrylate) films	77
Table 4.3 Surface properties of cured TE and TEF coatings.....	81
Table 4.4 Modulus and surface energy values of elastomeric mold materials used in UV micromolding processes.....	87
Table 5.1 Compositions of R2R UV imprinting formulations	99
Table 5.2 Gel times of coating formulations at different light intensities.	111
Table 5.3 Base processing conditions for UV R2R Imprinting.....	119

LIST OF FIGURES

Figure 2.1 Mechanism of thiol-ene reaction.	10
Figure 2.2 Schematic of photoinitiated radical polymerization.	12
Figure 2.3 Schematic of the inhibitory effect of oxygen on free radical photopolymerization	17
Figure 2.4 Applications of microstructured films and coatings.....	19
Figure 2.5 Imprinting process with UV curable coatings	22
Figure 2.6 Schematic of R2R Impring process.....	24
Figure 3.1 Chemical structure of UV curable coatings.....	28
Figure 3.2 Schematic of the illumination mode for multiple pulses of flash lamp curing.	29
Figure 3.3 Spectrum of the xenon lamp.....	29
Figure 3.4 Schematic of real-time FTIR measurement.....	31
Figure 3.5 Schematic of ATR measurement.....	33
Figure 3.6 Real-time FTIR spectra of acrylates under UV illumination.	36
Figure 3.7 Comparison of curing kinetics of acrylate and epoxy under the exposure of a mercury lamp.....	37
Figure 3.8 Conversion versus the net illumination time for the single pulse curing and the multiple pulses curing of TMPTA coatings.	38
Figure 3.9 Conversion versus PI concentration for TMPTA coatings.....	46
Figure 3.10 Temperature profile in IPL curing of a TMPTA film sandwiched between two NaCl plates.	47
Figure 3.11 Conversion versus curing temperature for TMPTA coatings.....	49
Figure 3.12 PI loss during UV curing for TMPTA coatings.	50
Figure 3.13 Depth profiles of curing conversion of TMPTA coatings cured with a mercury UV lamp and a xenon flash lamp, respectively.	51
Figure 3.14 Top and bottom conversions measured with the FTIR-ATR technique.	52
Figure 4.1 Chemical structures of materials employed in coating formulations. .	60
Figure 4.2 UV-visible spectrum of the PDMS mold.	67
Figure 4.3 Schematic representation and picture of the apparatus for the peel strength measurement.	69

Figure 4.4 Functional group conversion vs. time for a TEA10 coating. The sample contains 0.25 wt.% DMPA and was exposed to UV light at 100 mW/cm ²	70
Figure 4.5 Thiol group conversion as a function of the irradiation time in thiol-ene(-acrylate) photopolymerizations monitored by real-time FTIR.	72
Figure 4.6 DSC curves of the first and second heating cycles of TE.	74
Figure 4.7 DSC curves of thiol-ene(-acrylate) networks at a 10°C/min heating rate.....	75
Figure 4.8 Stress-strain curves of UV-cured thiol-ene(-acrylate) coatings under ambient conditions.	76
Figure 4.9 SEC trace of F-PMMA.....	78
Figure 4.10 ¹ H NMR trace of F-PMMA	79
Figure 4.11 Contact angle measurement of TE and TEF coatings.	80
Figure 4.12 XPS survey spectra for cured TE and TEF coating surfaces.....	81
Figure 4.13 TGA thermograms of thiol-ene(-acrylate) cured coatings.	82
Figure 4.14 Modulus tunability of thiol-ene(acrylate) coating system.....	83
Figure 4.15 Surface energy tunability of the thiol-ene(acrylate) coating.	83
Figure 4.16 SEM images of the surface microstructures of thiol-ene(-acrylate) coatings with different moduli.	84
Figure 4.17 SEM images of microstructured TEF coatings with various grating heights: (a) 20 μm, (b) 50 μm, and (c) 100 μm.....	86
Figure 4.18 Representative peel strength versus displacement of the peel front of patterned TEA10 and TEF, which have different surface energies but similar moduli. Grating height: 50 μm.....	88
Figure 4.19 (a) Clean release of the TEF coating and (b) demolding failure of the TEA10 coating.	89
Figure 4.20 Averaged peel strength of TEA10 and TEF at grating heights of 20 μm, 50 μm, and 100 μm.	90
Figure 4.21 Representative peel strength versus displacement for TEAx coatings with various moduli but similar surface energies.	91
Figure 4.22 Averaged peel strength plotted against TEAx coatings at grating heights of 20 μm and 50 μm.	92
Figure 4.23 SEM image of the surface patterns of TEF.	93
Figure 4.24 Static water contact angle for TEF coatings patterned with micrograting arrays. Inset: photograph of a blue-dyed water droplet on the surface of a patterned TEF coating.....	93

Figure 5.1 Roll-to-roll UV imprinting pilot line at the University of Minnesota.	102
Figure 5.2 Materials of R2R UV imprinting coating formulations.	98
Figure 5.3 Dynamic viscosity for coating formulations with different ratios of thiol groups and acrylate double bonds.	105
Figure 5.4 Dynamic viscosity for formulations with various UAO contents.	105
Figure 5.5 Double bond conversion for formulations with different thiol-to-ene ratio recorded by real-time FTIR.	108
Figure 5.6 Thiol conversion for formulations with different thiol-to-ene ratio recorded by real-time FTIR.	109
Figure 5.7 Double bond conversion coating formulations with various UAO content.	109
Figure 5.8 Thiol group conversion for coating formulations with various UAO content.	110
Figure 5.9 Dynamic storage and loss moduli versus UV exposure time measured by photo-rheology.	111
Figure 5.10 Storage modulus as a function of temperature for cured materials with different UAO concentrations.	113
Figure 5.11 $\tan\delta$ as a function of temperature for cured materials with different UAO concentrations.	114
Figure 5.12 Double bond conversions of thiol-ene coatings plotted against the web speed of R2R imprinting for formulations with different thiol-to-ene ratios.	115
Figure 5.13 Double bond conversions of thiol-ene coatings plotted against the web speed of R2R imprinting for formulations with different oligomer contents.	117
Figure 5.14 (a)UV imprinting unit of the R2R pilot coating line. (b) Schematic of the imprinting unit.	118
Figure 5.15 Effect of lamp power on conversion of imprinted coatings.	119
Figure 5.16 Effect of lamp distance on the imprinted coating conversion at a lamp power of 100% and a web speed of 0.34 cm/s.	120
Figure 5.17 Effect of web speed on the imprinted coating conversion at a lamp power of 100% and lamp distance of 0.34 cm.	121
Figure 5.18 Influence of exposure dosage on the imprinted coating conversion.	122
Figure 5.19 R2R micromolding fabricated patterns with the 20-80_UAO50 coating formulation.	123

1 Introduction

1.1 Motivation

UV curable films and coatings are ubiquitous in everyday life and various industrial applications, including protection layers¹, adhesives² and dental materials³. With surface microstructures, patterned coatings can serve critical design purposes, such as providing engineered optical properties like anti-reflection films⁴, altering surface properties of a substrate like superhydrophobic coatings⁵, or delivering specific functionality like microfluidic devices^{6, 7} and flexible electronics⁸⁻¹⁰.

A UV curable system typically contains monomers or oligomers, photoinitiators, and additives like rheology modifiers and surfactants. The coating is applied to a substrate in the liquid state and then solidified upon UV illumination to form crosslinked polymer networks. Fast photopolymerization is highly demanded to enable large-volume and low-cost manufacturing processes with UV curable materials. At the same time, a high curing extent is required to ensure low levels of residue monomers for safety and long-term stability concerns. The curing rate and extent are strongly dependent on the monomer chemical structures, light sources, curing temperatures, and photoinitiator loadings. One of the main objectives of this research is to understand the curing kinetics of UV curable coatings and to investigate how to boost the curing speed without compromising the curing extent.

UV micromolding (imprinting) is one of the most promising techniques to fabricate surface microstructures on UV curable coatings. It involves three steps: mold filling, UV curing, and demolding. First, a liquid UV curable material is coated on a substrate and a mold with surface patterns is brought into contact with the liquid coating. Then, the coating is solidified by UV exposure with the mold in place. Finally, the mold is peeled off to obtain a patterned coating. Because UV micromolding is a contact process, a grand technical challenge of the UV micromolding process is the defect rate. Defects may generate in each step of the process. For example, incomplete mold filling can lead to bubble defects, uncured materials can result in a tacky surface or poor pattern fidelity, and adhesion failure may occur during demolding. In traditional integrated circuit manufacturing, the acceptable error rate of functioning devices is below 0.1 defects/cm².¹¹ However, the demonstrated defect density is roughly 1 defects/cm² for micromolding processes.¹² Closing the gap in the defect density between conventional lithographic techniques and the micromolding (imprinting) process calls for the optimization of material properties (kinetics, rheological and mechanical properties), a systematic understanding of their influences on the pattern quality, and critically engineered product functionalities.

For the application of UV micromolding in mass manufacturing, a high throughput is required to reach a given annual avenue. Towards this end, micromolding is moving roll-to-roll. With the roller mold, it is possible to fabricate patterned coatings and films on a moving web at large volume and thus significantly enhance the throughput. In roll-to-roll processing, the mold filling,

curing, and demolding take place continuously and complete within seconds, putting forward even more stringent requirements on materials properties. Therefore, it is of great importance to design a UV curable material system with tunable material properties and to demonstrate its scale-up capability in roll-to-roll imprinting processes.

1.2 Thesis outline

The results presented in this thesis advance the understanding of UV curing kinetics and extend the application of UV curable materials to the fabrication of microstructured coatings in roll-to-roll processing. Chapter 2 provides some of the essential background information on UV curing and gives an overview of surface replication techniques.

In this research, the UV curing process of acrylate coatings was investigated under intense pulsed light irradiation conditions using a xenon flash lamp. The curing extents of a model acrylate system were monitored using the Fourier transform infrared spectroscopy (FTIR). The results are discussed in Chapter 3. FTIR results revealed that the use of a single pulse of intense illumination achieved sufficient curing extents within milliseconds. For the curing with multiple pulses, the total UV dose is the dominant factor of curing extents. However, the curing speed is a function of various processing variables including the dose rate, the PI concentration, and the curing temperature. In addition, the depthwise curing gradient in flash lamp curing was studied and compared with that obtained with a traditional mercury lamp.

Chapter 4 discusses the design of UV curable coatings for the surface replication technology of UV micromolding. A ternary thiol-ene-acrylate coating system was developed for the fabrication of surface microstructures at high throughput. The elastic modulus of cured materials was tuned over two orders of magnitude by adjusting the crosslinking density of cured polymer networks through the acrylate content. A fluorinated polymer additive was designed and synthesized to modify the surface property of the thiol-ene-acrylate system. Combining UV LED curing and the thiol-ene-acrylate coating system, the preparation of microstructured coatings was achieved within 10 seconds. In addition, the fabrication of challenging patterns, dense and tall microchannel arrays, was demonstrated with the fluorinated coating formulation.

Chapter 5 presents the fast and continuous fabrication of microscale structures by roll-to-roll UV imprinting on a 150 mm wide web. This process is enabled by a UV curable thiol-ene-acrylate resin system. A series of formulations were developed with fast curing speeds at ambient conditions, low viscosities, and tunable mechanical properties. The rate and extent of curing in the roll-to-roll process were investigated with Fourier transform infrared spectroscopy as a function of the formulation composition and the processing variables. All the prepared thiol-ene-acrylate formulations show improved curing speeds compared to a commercial benchmark and reached high double bond conversions (>80%). The thiol-ene-acrylate coating is demonstrated to be a versatile material system for patterning applications and roll-to-roll imprinting is a powerful tool that

allows continuous and large-area fabrication of microstructured coatings and films. Finally, Chapter 6 offers possible directions for future research.

2 Background Information

2.1 UV curable systems

UV curing is a method to synthesize thermoset materials from liquid monomers or oligomers into highly crosslinked polymers with UV light. The advantage of using UV light to initiate polymerization is mainly the fast reaction speed under intense illumination. In addition, UV curing only occurs in the illuminated area, which allows spatial resolution and thus complex relief patterns to be produced. Furthermore, UV curing presents other desirable features, including ambient temperature operation, low energy consumption, and solvent-free formulations.


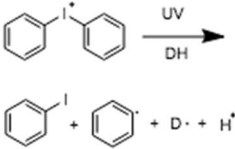
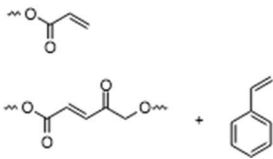
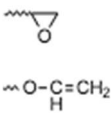
UV curing has found a wide range of applications in various industrial sectors. This technology is commonly used to solidify protective coatings, adhesives, and films in the automotive and infrastructure sectors.¹³ In addition, in the semiconductor industry, high-resolution images are fabricated with UV illumination by photolithography to manufacture microcircuits.¹⁴

2.1.1 *Free Radical Photopolymerization*

Free radicals can be generated upon UV illumination of photoinitiators either by homolytic cleavage of C-C bonds or by hydrogen abstraction. Acrylates are by far the most widely used UV curable materials mainly due to their fast

reaction speed. In addition, acrylate-based materials exhibit remarkable mechanical, optical and chemical properties. A vast variety of acrylate monomers and oligomers are commercially available to allow for the tunability of mechanical properties.

Table 2.1 Different types of UV-curable resins¹⁵⁻¹⁷

Mechanism	Radical	Cationic	Thiol-ene click reaction
Photoinitiator	Aromatic ketone 	Aryliodonium salt 	Aromatic ketone or no photoinitiator
Monomers and oligomers	(1) Acrylate (2) Unsaturated polyester/styrene 	(1) Epoxide (2) Vinyl ether 	(1) thiol and ene $R-SH + H_2C=CHR$
Advantages	(1) Fast cure (2) Excellent mechanical, optical, and chemical properties (2) Commercial availability	(1) Not sensitive to oxygen (2) Small curing contraction (3) Good thermal and chemical stability	(1) Fast cure (2) No oxygen inhibition (3) Low volume shrinkage
Drawbacks	(1) Oxygen inhibition (2) High shrinkage	(1) Slow cure	(1) Unpleasant odor (2) Short shelf-life

Besides acrylates, the copolymerization of unsaturated polyesters and styrene is another resin to be used in large-scale applications. Although this

system shows inferior product properties and lowers curing speed compared to acrylate resins, it is still widely used because of its low cost.

However, it is well known that free radical photopolymerization is inhibited by oxygen, which significantly lowers the curing speed in the presence of air and may result in tacky surfaces.¹³ To resolve this issue, inert atmosphere¹⁸ (e.g. nitrogen blanketing) and intensive irradiation¹⁹ have long been utilized in practical applications. Furthermore, increasing the photoinitiator concentration has been utilized to deal with oxygen inhibition in acrylate systems²⁰, which is similar to using intensive irradiation in that both lead to more initiating radicals and thus a rapid consumption of oxygen. Additionally, new photoinitiators have been developed and reported to effectively hinder oxygen inhibition. For example, photoinitiators with covalently bonded fluorinated²¹ or alkylsiloxane²² groups result in improved surface cure in air because they tend to collect on the top surface due to the reduced surface energy. These hydrophobic photoinitiators have potential negative effects, such as enhancing the oxygen solubility in coatings and incompatibility with printing inks. Type II photoinitiators (radicals are produced in a bimolecular reaction between sensitizer and co-initiator) has been frequently reported to outperform Type I photoinitiators (radicals are generated in a monomolecular reaction through bond cleavage) in overcoming oxygen inhibition.^{23, 24 25} Co-initiators (typically amine, thiol, and alcohol) that act as the hydrogen donors can react with oxygen or peroxide to decrease the concentration of oxygen. Besides co-initiators, a few sensitizers used in Type II

photoinitiator systems could also directly contribute to oxygen consumption, e.g. 2-ethylanthraquinone (EAQ).²⁶

In addition to oxygen inhibition, volume shrinkage of acrylic materials (as high as 10%²⁷) can raise problems in patterning applications because of the resulting dimensional inaccuracy of cured products. Associated with volume shrinkage, stress development within UV cured materials will lead to defects, e.g. curling and cracking.²⁸

2.1.2 *Cationic Photopolymerization*

The most efficient cationic photoinitiators are diaryliodonium or triaryl sulfonium salts.^{29, 30} In the presence of hydrogen donors, cationic photoinitiators undergo photolysis reaction, generating protonic acids and free radicals. Cationic photopolymerization is used to cure monomers that are insensitive towards free radicals, in particular, epoxides and vinyl ethers. Upon UV illumination, the ring-opening reaction of epoxides proceeds efficiently in the presence of protonic acids to produce a polyether. The curing of epoxides is generally an order of magnitude lower than acrylates, probably due to a lower propagating rate constant.³¹ For vinyl ethers, their electron-rich double bonds are not reactive towards free radicals but undergo a fast and complete cationic polymerization. Vinyl-ether terminated oligomers containing urethane, ester, or ether structures offer a wide range of tailor-made properties.

There are three main differences between free radical and cationic photopolymerization.^{32, 33} First, cationic curing is not sensitive towards

atmospheric oxygen. Second, cationic curing shows significant dark reaction, i.e. living character, due to the lack of bimolecular termination. Third, the volume contraction of cationic cured systems is less compared to acrylates.

2.1.3 Thiol-ene reaction

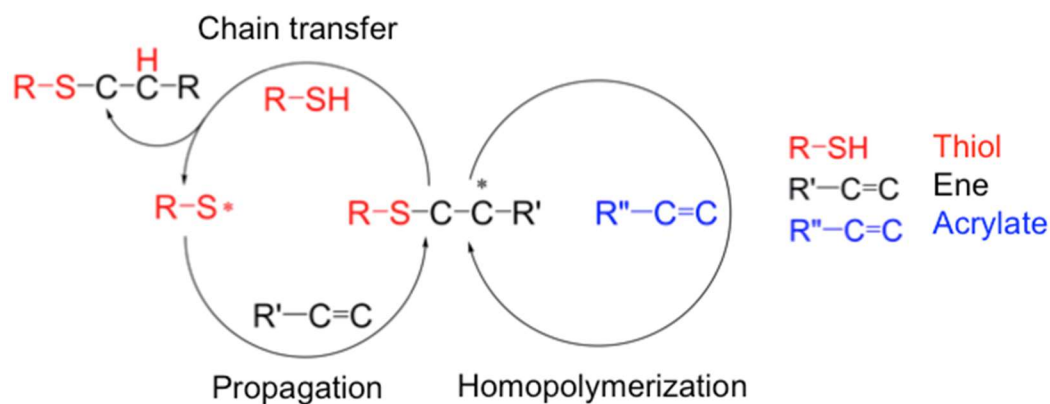


Figure 2.1 Mechanism of thiol-ene reaction.

Mechanism adapted from literature¹⁷.

Classical radical- or cationic-based photopolymerization involving acrylates and epoxies provides both temporal and spatial control of the reaction and finds a plethora of applications, from coatings, adhesives, to photolithography processes. However, traditional UV curing processes and materials are plagued by their inherent limitations in balancing curing speed, internal stress, and sensitivity to oxygen and air, as discussed in the above sections.

Recently, a new class of UV curable materials based on thiol-ene has drawn increasing attention.³⁴⁻³⁶ The light-mediated thiol-ene reaction undergoes a radical-mediated step-growth mechanism where the thiol radicals add across the ene double bonds and cause the molecular weight growth. Similar to free-radical

photopolymerization, the thiol-ene reaction proceeds as fast as acrylates under UV illumination, which can be controlled at specific times and locations. Unlike classical radical-based process, this reaction enjoys a high yield with less by-product generation. Moreover, the thiol-ene reaction takes place in mild conditions without requirements of high temperature or inert environment curing. Additionally, the developed polymer networks show a high degree of homogeneity and thus exhibit a narrower glass transition range, which is highly desirable in applications focusing on excellent mechanical properties, for example, energy absorbing materials. Beneficial from the uniform network structure, the shrinkage and stress of cured materials are significantly reduced, lowering the possibility of defect formation common in classical UV curable materials.

These advantages have made thiol-ene based materials the focus of extensive research efforts and practical applications. They have been successfully used for fundamental research purposes such as basic chemical synthesis and polymer surface modifications.^{37, 38} In recent years, their applications have been extended to new areas in microfluidic devices^{39, 40} and nano-imprinting⁴¹⁻⁴³. However, the wide use of thiol-ene in large-scale manufacturing processes is still plagued by several limitations such as the unpleasant odor of thiols and the relatively short shelf-life, which needs to be addressed in future research.

2.2 Photopolymerization kinetics

2.2.1 Basic process

The basic photopolymerization process involves autoacceleration, propagation, and vitrification.^{16, 44} At the very beginning of the irradiation,

photopolymerization exhibits an autoacceleration characteristic until reaching a maximum reaction rate. This is due to the rapid increase of viscosity and the resulting mobility restriction of free radicals. As the termination step becomes diffusion controlled, the radical concentration builds up and leads to an increase in the polymerization rate. Following the autoacceleration process, the propagation step also becomes diffusion controlled. As a result, the reaction slows down and ultimately stops due to vitrification. Because most of the UV curable resins are based on acrylate monomers and oligomers, in this section, the discussion will be focused on free radical photopolymerization kinetics.

2.2.2 Initiation Efficiency

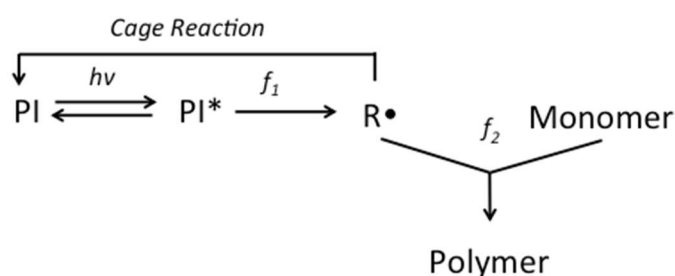


Figure 2.2 Schematic of photoinitiated radical polymerization.

Mechanism adapted from Reference [44].

The photoinitiator (PI) plays a key role in UV curable systems regarding both the curing speed and the achievable conversion. In the selection of appropriate photoinitiators, desirable features include strong absorption of UV light in the range of illumination wavelengths, a fast photolysis reaction, and photobleaching behavior for sufficient cure depth.⁴⁵ Upon UV illumination,

photoinitiators go through the excited state to generate free radicals and then react with monomers to initiate photopolymerization (Figure 2.2). The effectiveness of a photoinitiator can be evaluated by the initiation efficiency, which is defined as the number of radicals generated per PI molecule. It can be expressed by the product $f_1 \cdot f_2$, where f_1 is the fraction of PI excited states that produce free radicals and f_2 is the fraction of radicals that combine with monomers. By definition, the initiation rate, r_i , is proportional to the loss rate of PI ($\frac{d[PI]}{dt}$) and the initiation efficiency as shown in Equation 2.1. In addition, it can be expressed as a function of the polymerization rate (R_p) according to Equation 2.2:

$$r_i = \frac{d[PI]}{dt} \cdot f_1 \cdot f_2 \quad \text{Equation 2.1}$$

$$r_i = \frac{2k_t \cdot R_p^2}{k_p^2 \cdot [M]^2} \quad \text{Equation 2.2}$$

where k_p is the propagation rate constant, k_t is the termination rate constant, and $[M]$ is the molar concentration of functional groups. Combining the above equations leads to the following equation:

$$f_1 \cdot f_2 = \frac{2k_t \cdot R_p^2}{k_p^2 \cdot [M]^2 \cdot \frac{d[PI]}{dt}} \quad \text{Equation 2.3}$$

Therefore, the initiation efficiency can be quantitatively evaluated from the initial polymerization rate recorded with real-time FTIR and the initial PI loss rate measure with real-time UV spectroscopy, respectively.⁴⁴ It was reported that the initiation efficiency of diphenyl(2,4,6-trimethyl benzoyl) phosphine oxide (TPO) was 1.3 radicals per TPO, which is close to the theoretical value of 2 and explains

the great reactivity of TPO towards acrylate double bonds.⁴⁴ However, it should be pointed out that although the fast decomposition of photoinitiators upon UV illumination is beneficial for increasing the polymerization speed, the depletion of photoinitiators might result in the premature ending of the curing process. Thus optimizing both the type and concentration of photoinitiators is critical to achieving fast curing speed as required in various applications.

2.2.3 Curing speed

The rate of photopolymerization, R_P , can be expressed as:

$$R_P = \frac{k_p}{(2k_t)^{0.5}} [M]r_i^{0.5} \quad \text{Equation 2.4}$$

$$r_i = \Phi_i \cdot I_a \quad \text{Equation 2.5}$$

where k_p is the propagation rate constant, k_t is the termination rate constant, $[M]$ is the molar concentration of functional groups, r_i is the rate of initiation, Φ_i is the initiation quantum yield, and I_a is the absorbed light intensity.⁴⁴ It should be noted that Equation 2.4 is derived based the steady state of radical concentration and bimolecular termination, which holds true for the early stage of curing until vitrification takes place. According to Equation 2.4, first of all, the reaction speed depends on the chemical structure of a UV curable resin. It explains why acrylate resins have a high polymerization rate: the high propagation rate constant ($k_p \approx 10^4 \text{ l} \cdot \text{mol}^{-1} \cdot \text{s}^{-1}$) and the relatively low termination rate constant ($k_t \approx 10^5 \text{ l} \cdot \text{mol}^{-1} \cdot \text{s}^{-1}$) contribute to the observed fast reaction upon UV illumination.⁴⁶

Second, the reaction speed increases with the molar concentration of functional groups. Therefore, materials with high functionalities and/or lower molar mass typically exhibit fast curing characteristics. Third, the photopolymerization proceeds faster upon intense UV illumination because of a higher initiation rate.

2.2.4 *Achievable conversion*

It is well known that for most UV curable systems, the final conversions are less than 100%, which might raise concern in long-term stabilities such as hardening or coloration upon heat or UV aging. There are different factors affecting the achievable UV curing conversions, mainly including the chemical structure, light intensity, and the curing temperature.^{27, 44, 47}

First, different types of chemical structures significantly affect the curing process by controlling the mobility of reactive species during curing, the polymer network structure, and the final properties. High degree of conversions (approaching 100%) can be reached with aliphatic telechelic acrylate oligomers, leading to the formation of elastomeric materials with a glass transition temperature lower than the room temperature, well suited for adhesive and footwear applications.⁴⁸⁻⁵⁰ By contrast, with aromatic acrylates or multi-functional crosslinkers, glassy materials can be prepared which typically show a conversion far from 100% and a T_g higher than room temperature.²⁸ In the latter case, the polymerization stops prematurely after vitrification because the molecular mobility becomes restricted.

Second, increasing the sample temperature either during or after curing is another way to achieve complete curing in photopolymerization.⁵¹ During UV curing, the mobility of reactive species increases with the sample temperature, so the reaction can proceed to a higher conversion. After UV curing, thermal aging can restore the mobility of trapped radicals, leading to additional curing with unreacted functional groups. Additionally, the higher conversion after thermal aging can be attributed to the decomposition of hydroxides previously formed by the reaction of free radicals with oxygen and therefore the generation of more initiating radicals such as hydroxyl and alkoxy radicals.⁵² It should be mentioned that curing at elevated temperature can also lead to changes in the final properties of cured materials. As a result of more complete conversions, the T_g of the cured material is higher and, concomitantly, the polymer hardness increases. Furthermore, it is expected that the long-term stability is enhanced in cases of curing at elevated temperatures because of less residual photoinitiator fragments and less uncured double bonds.

Third, a complete photopolymerization can be achieved by performing UV curing at higher light intensity, which could be explained by two possible hypotheses: a greater excess free volume^{27, 53, 54} and a rise of the sample temperature⁵⁵. According to the former theory, as the polymerization rate increases with the light intensity, the actual specific volume of the polymer network is not able to shrink as fast as the thermodynamic equilibrium specific volume. The generated excess free volume enhances the mobility of reactive species and therefore leads to a higher maximum achievable conversion. For the

latter hypothesis, a temperature rise typically associates with the intense light curing and explains the observed conversion increase. Because of the fast reaction rate at high UV intensity, the heat generated from photopolymerization is significant within a short period of time, resulting in resorted molecular mobility high temperatures and increased conversions as discussed previously. Evidence in favor of this process was obtained by developing a novel method based on real-time FTIR, where the sample temperature was monitored in situ using a polypropylene film as a temperature probe and the sample conversion was recorded by the spectrometer during UV curing.⁵⁶ Results showed that samples developed a higher maximum temperature when exposed to more intense UV light and the final conversion was linear with the maximum temperature.

2.2.5 Influence of atmospheric oxygen

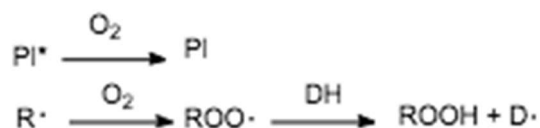


Figure 2.3 Schematic of the inhibitory effect of oxygen on free radical photopolymerization

Adapted from reference [44]

It is well known that the free radical photopolymerization suffers from the oxygen inhibition problem.^{16, 44} The presence of oxygen can quench the excited state of PI, lowering the photoinitiator efficiency. In addition, the formed free radicals can react with oxygen to form peroxy radicals, which is inactive towards acrylate double bonds. The peroxy radicals further undergo hydrogen abstraction

with other monomers or polymers, yielding hydroperoxides and alkoxy radicals, which can also be scavenged by oxygen. Therefore, upon UV illumination, the generated free radicals first need to consume the dissolved oxygen in the system. The UV curing will only start until the oxygen concentration is sufficiently low to allow for monomers to successfully compete with oxygen for initiating radicals.

There are several factors affecting the inhibitory effect of oxygen during UV curing: photoinitiator efficiency, formulation viscosity, film or coating thickness, and the light intensity. Using PI with higher photoinitiator efficiency can suppress the influence of oxygen during curing because the oxygen will be removed faster at a high flux of initiating radicals.¹⁶ Increasing formulation viscosity leads to a reduced oxygen inhibition effect due to slower oxygen diffusion into the UV curable materials.⁵⁷ Similarly, oxygen diffusion is limited in cases of thick film or coatings although insufficient cure of the surface layer can also be a problem due to its direct contact with air.⁵⁸ Increasing the light intensity is commonly used in the industrial environment to address the oxygen problem by raising the overall reaction rate.¹⁹ As a result of the fast reaction, the formulation viscosity builds up faster under intense illumination, reducing the exposure time during which oxygen diffuses into the system. Besides intense UV exposure, curing under an inert environment is sometimes necessary to achieve efficient curing.⁵⁹ Nitrogen and carbon dioxide have been used to protect UV curable materials from the influence of atmospheric oxygen.

2.3 Surface Replication Technologies

2.3.1 Applications of microstructured coatings and films

Broad applications of microstructured coatings and films have been witnessed. For example, patterned coatings can be used to produce surface textures in the wood finishing industry. In addition, surface microstructures impart materials with new functionalities for applications in functional optical films⁶⁰, hydrophobic characteristic⁵, and flexible electronics⁶¹. (See Figure 2.4)

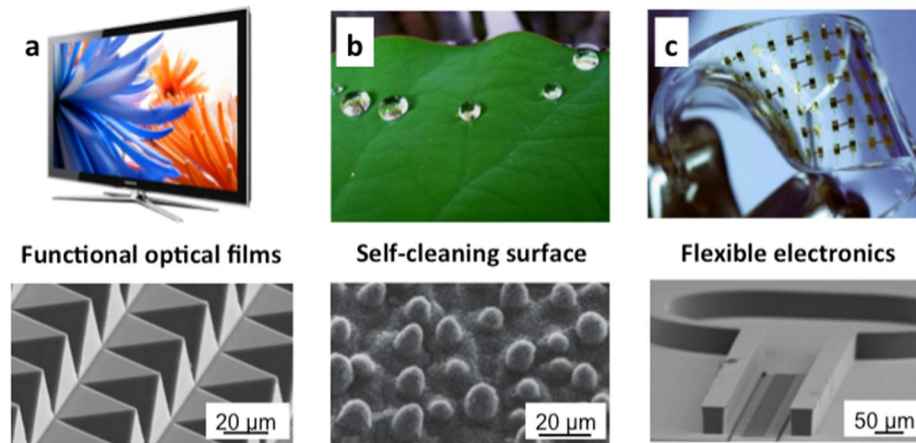


Figure 2.4 Applications of microstructured films and coatings.

Pictures adapted from references⁶¹⁻⁶³.

A. Optical applications

Materials with surface nano/microstructures are widely adopted to fabricate optical tools including optical data storage devices^{64, 65}, flat panel displays⁶⁶, and fiber coupling⁶⁷. Chang *et al.*⁶⁸ fabricated microlens arrays with a UV curable material and a soft mold with micro-holes. With the proper combination of imprinting pressure, imprinting duration, and UV curing dosage, the shape and height of microlens can be well controlled. Taniguchi *et al.*⁶⁹

demonstrated the fabrication of self-supporting antireflection structures using a UV curable material. In addition to surface structures, the elimination of interface reflection reduces reflection to 0.2-0.3% in the optical spectrum range of 430-950 nm. Inspired by the moth-eye structures, optical films with excellent optical transparency were achieved with the incorporation of surface microstructures.⁷⁰ However, it should be mentioned that the overall film thickness (including the height of microstructures and the thickness of a residual layer underneath the raised features on the mold) strongly influences the light absorption of films and can restrict optical applications like light-enhancing films and solar cells. Therefore, a thin film with minimized residual layer thickness is typically desirable in these optical applications.

B. Medical applications

The capability to fabricate surface nano/microstructures with high precision and throughput makes it possible to manipulate protein, DNA, small molecules and nanoparticles, which is suitable for applications in protein delivery, drug delivery, and biosensors.^{71, 72} Microneedle arrays are used as an efficient drug delivery tool, which can be readily prepared with the inclined/rotated UV lithography process. Based on spatially controlled UV exposure, the microneedle fabrication process can be significantly simplified and at the same time achieve higher precision and reduced cost.^{73, 74} Moreover, complex nano/microstructures like microchannels and microcups are basic components of biosensors, especially

useful for state-of-art cancer diagnosis where large panels of molecular markers have to be evaluated.^{75, 76}

C. Electronic applications

Due to the flexibility and low cost of polymer materials, polymeric coatings and films with surface nano/micropatterns are raising increasing interest as an alternative technology to replace conventional silicon-based photovoltaic devices. Patterned polymeric materials have found various electronic applications including electro-optic modulators⁷⁷, wire-grid polarizers⁷⁸, silver electrodes⁷⁹, and organic electronics⁸⁰. Mahajan *et al.*⁶¹ achieved a self-aligned strategy for the fabrication of flexible electronic devices. Multilevel trench networks were fabricated on a polymer substrate and silver ink was then deposited into the networks using capillary force, achieving the fabrication of major building blocks of integrated circuits such as transistors, resistors, and capacitors. In addition, Ahn *et al.*⁷⁸ pioneered the continuous fabrication of surface nanograting structures using roll-to-roll imprinting process with UV curable resins and demonstrated its application as wire-grid polarizers.

2.3.2 Overview of surface replication techniques

Optical photolithography is by far the dominant technology in the semiconductor industry to manufacture devices with increasing levels of functionality in smaller spaces. In photolithography, UV illumination transfers geometric patterns to a UV curable material (photoresist) through a photomask.

Modern photolithography tools, using 193 nm of illumination, are capable of fabricating features at a resolution of 38 nm within an uncertainty of 2.5 nm.¹¹ Achieving such a high resolution of photolithography requires careful engineering of the mask and precise control of the illumination incident on the mask, which relies heavily on available computing power and even multiple masks at a high cost. However, because of the inherent limitation in resolution due to light diffraction, extreme ultraviolet lithography (EUV) evolves as an alternative lithography tool, which operates at a wavelength of 13.5 nm, for the fabrication of devices with greater circuit densities.⁸¹ EUV brings higher costs related to complexity and the use of much shorter wavelength but greatly reduces the difficulty in mask design. As impressive as the current state-of-art photolithography technologies are, it should be pointed out that there is a significant trade-off between the resolution and cost and therefore the technology only needs to be as good as it needs to be considering the economic gain with increasing circuit densities. In addition, the accurate layer-to-layer overlay is more critical compared to the absolute dimensions of integrated circuit applications. Thus, certain variations in the overall size and shape up to a few percentages are acceptable in practical applications.

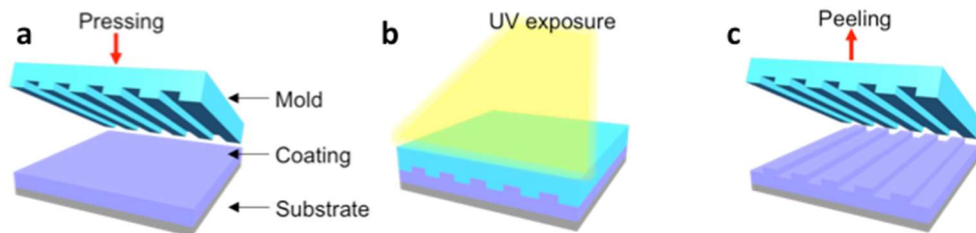


Figure 2.5 Imprinting process with UV curable coatings

(a) a liquid coating forms conformal contact with a patterned mold, (b) the coating

is exposed to UV light through the mold, and (c) the cured coating obtains surface microstructures after the mold is peeled off.

Imprinting lithography uses an imprint stamp with relief patterns for the fabrication of surface micro/nanostructures. Based on the characteristics of imprinted materials, there are two main imprinting methods: thermal-imprinting and UV-imprinting.^{82, 83} For thermal imprinting, thermoplastic materials are softened and patterned at high temperatures, followed by solidification through a cooling cycle. Due to the high viscosities of thermoplastic materials at elevated temperatures, high pressures are needed for successful pattern transfer. For UV imprinting (Figure 2.5), the imprint stamp is brought into contact with a liquid UV curable material, which is cured with the mold in place to lock the surface features. Different from thermal imprinting, UV imprinting process can be operated at room temperature and ambient pressure, potentially lowering the process cost. Because the pattern replication of imprinting processes is based on mechanical deformation rather than spatially selective UV illumination as in optical photolithography, the resolution of imprinting can be pushed to less than 10 nm. Another benefit comes from the ability of imprinting lithography to fabricate multilevel patterns simultaneously, which significantly reduces the complexity of device fabrication.

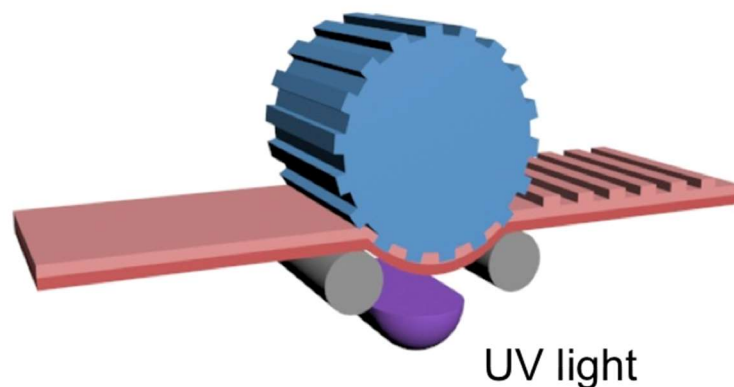


Figure 2.6 Schematic of R2R imprint process.

An attractive feature of the imprinting technology is its compatibility with the roll-to-roll system (Figure 2.6); by using a roller mold, it is possible to fabricate nano/microstructured films and coatings in a continuous way. This can significantly increase throughput and reduce the cost to a range between 0.1 \$/m² to 1 \$/m².¹¹ It is especially suitable to applications where single-level structures are used such as holographic wrapping paper⁸⁴ and superhydrophobic surfaces⁸⁵. Extending to nanoscale features, the roll-to-roll imprinting process would enable a wide range of applications including wire-grid polarizers⁷⁸, organic photovoltaic devices⁸⁶, and antireflective coatings⁸⁷.

3 Pulsed Irradiation for High-throughput Curing Applications*

3.1 Background and Motivation

A xenon flash lamp was used to create intense pulsed light (IPL) irradiation to cure acrylate coatings at very high rates and ambient temperature. In this chapter, we studied the ambient temperature IPL curing of an acrylate monomer system that is known to present a limited attainable cure with low-intensity UV irradiation. The capability of xenon flash lamps for fast photopolymerization of acrylate resins was investigated using a single pulse and a multiple pulse pattern. We wished to determine whether the achievable cure and cure rate can be increased with IPL and as the IPL parameters are changed to increase the net rate of irradiation dose - with more intense pulses, with longer pulses, and with shorter pulse periods (i.e., more closely timed pulses). We also examined whether the achievable cure depends on the PI concentration and the curing temperature.

High-powered mercury lamps are widely used to provide high UV intensities in order to increase the rate of cure. However, mercury lamps can result in temperature increases - both from nonselective irradiation and from high reaction rate - ozone production and excessive power consumption⁸⁸.

*Reproduced in part with permission from (Y. Du, et al., "Pulsed irradiation for high-throughput curing applications", *Prog. Org. Coat.* **2017**, 104, 104-109)

Lasers, attractive for emitting monochromatic high-intensity light, produce reactions in a localized area, so are limited to applications like microlithography and 3D printing. With recent advancements in the UV LED technology, UV LED systems can provide UV light of a tight, specific range of wavelengths without ozone production or IR radiation, but they put forward more stringent requirements on formulating compatible UV curable coatings.

A promising alternative light source that might avoid the disadvantages of mercury lamps is the xenon flash lamp, which can produce intense pulsed irradiation at ambient temperature over large areas. In this approach, termed "Intense Pulsed Light" (IPL) ⁸⁹, the high pulse intensity enables rapid generation of reactive species, while the dark periods between pulses can allow dissipation of the heat of reaction and of nonselective light absorption. These systems are used in the manufacture of medical devices, optical fibers, and electronics, and it has been suggested that xenon flash lamp can reduce the curing time to a few minutes (in some cases within seconds) for automotive coatings ^{88, 90, 91}. Recently, IPL curing has become attractive to researchers working on the roll-to-roll processing of printed electronics, where fast cure and low temperature are highly valued. Xenon flash lamps have been employed in the fabrication of dielectric capacitors ⁹² and electrically conductive adhesives ⁹³ on a laboratory scale, achieving complete cure much faster than the current mainstream methods of continuous UV curing.

There are only a few studies, though, quantitatively examining the factors that affect the speed and the extent of cure in IPL curing processes. Previous IPL

curing investigations show the curing processes are completed within several minutes, determined by the number of pulses necessary for the achievable conversion ^{88, 90, 91}. We aim to explore whether the curing speed can be further enhanced by carefully tuning a full range of processing variables in a model UV curable system. Work so far ^{90, 91} illustrates a general pattern that the cure conversion increases with the number of pulses, but it reaches a plateau at a maximum "achievable" conversion when the mobility of reactive groups becomes too limited for further reaction. Following the excess free volume hypothesis suggested by Kloosterboer and coworkers ⁵³, we are interested in whether the achievable conversion might be higher with higher irradiation dose rate. Previous work by Decker *et al.* ⁵⁵ suggested that increasing intensity with continuous mercury lamp irradiation might raise the achievable conversion, but they noted the strong possibility that temperature rise due to the reaction and to radiation absorption might be the cause.

This chapter presents a systematic investigation of the curing conversions of UV curable coatings as a function of pulsed light processing parameters, temperature, and the PI concentration. Conversion of coatings was measured using Fourier transform infrared (FTIR) spectroscopy.

3.2 Experimental

3.2.1 Materials

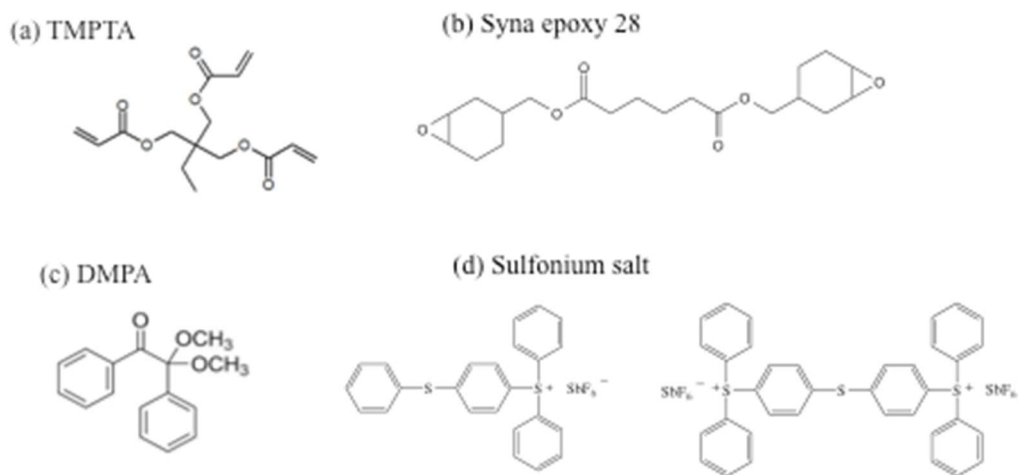


Figure 3.1 Chemical structure of UV curable coatings

In this chapter, trimethylolpropane triacrylate (TMPTA; Sigma-Aldrich, St. Louis, MO) was the monomer and 2,2-dimethoxy-2 phenylacetophenone (DMPA; Sigma-Aldrich, St. Louis, MO) was the PI for the acrylate system. For the epoxy coating system, bis (3,4-epoxycyclohexyl) methyl) adipate (Syna epoxy 28) was the monomer and a mixed triaryl sulfonium hexafluoroantimonate salt was used as the cationic PI. Their chemical structures are shown in Figure 3.1. DMPA has UV absorption peaks at 252 nm and 335 nm, the molar absorption coefficients of which are $16510 \text{ L} \cdot \text{M}^{-1} \cdot \text{cm}^{-1}$ and $266 \text{ L} \cdot \text{M}^{-1} \cdot \text{cm}^{-1}$, respectively⁹⁴. Coating formulations were prepared by dissolving PI into monomers and then stirring in the dark for 1 h. The amount of PI varied from 0.05 mol% to 5 mol% (expressed as the ratio of moles of PI molecules to the moles of monomer functional groups in the formulation).

3.2.2 Curing Conditions

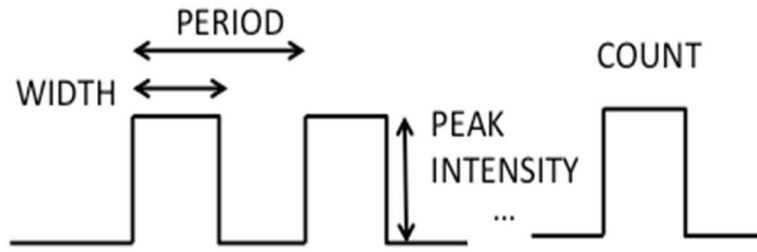


Figure 3.2 Schematic of the illumination mode for multiple pulses of flash lamp curing.

The light source utilized was a xenon flash lamp (Sinteron 2010, Xenon Corp., Wilmington, MA) in the burst mode, where a predetermined number of pulses was emitted. As shown in Figure 3.2, the time-varying irradiation pattern is determined by four processing parameters: the number of pulses (count), voltage (setting the energy level per unit time during pulses), the pulse width (the time duration of each pulse), and the pulse period (the delay from the leading edge of one pulse to that of the next pulse).

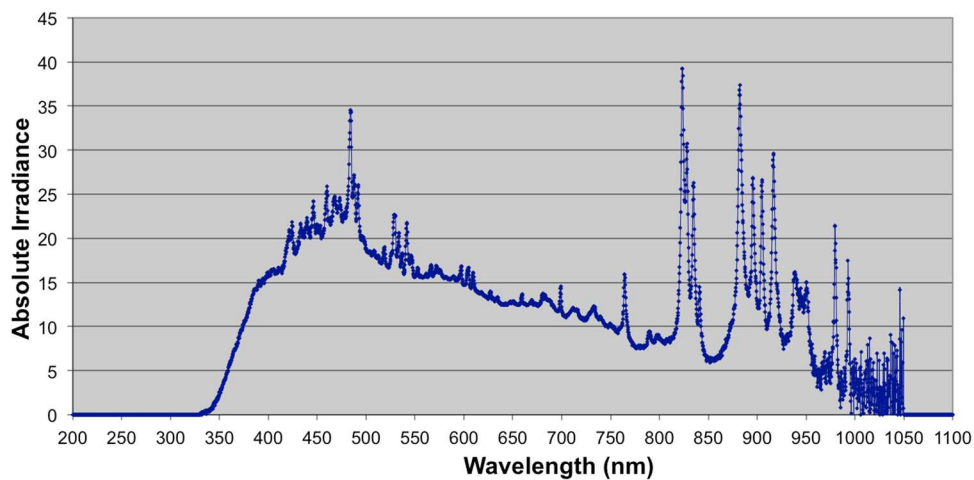


Figure 3.3 Spectrum of the xenon lamp.

Figure provided by the manufacturer.

According to the information provided by the manufacturer, the peak irradiation dose rate increases linearly with the lamp voltage. In addition to the pulsed irradiation mode, the xenon flash lamp is different from a conventional mercury lamp in both spectrum distribution and light intensity; it is energy-rich from 246 nm to 1000 nm with intensity on the order of 10 mW/cm² (Figure 3.3, Courtesy of Xenon Corp.). The lamp-to-sample distance was fixed at 25.4 mm.

3.2.3 Conversion Measurement

An FTIR spectrometer (Magna IR-750, Nicolet Instrument Co., Madison, WI) in transmission mode was used to measure the extent of cure of TMPTA coatings. Spectra were recorded with 32 scans and a resolution of 2 cm⁻¹ at room temperature. The Thermo Scientific OMNIC software package was used for spectra collection and data analysis. A background spectrum was collected before each sample measurement and subtracted from the sample spectrum. The uncured resin was sandwiched between two sodium chloride plates separated by a 0.025 × 25 mm steel spacer (McMaster-Carr, Chicago, IL), which was then exposed to pulsed irradiation. This arrangement permits UV transmission during curing due to the fact that sodium chloride is transparent to UV light from 200 nm to 400 nm⁹⁵ and effectively avoids oxygen inhibition problems associated with free-radical photopolymerization. Coating thickness was 25 μm, controlled by the thickness of spacers but with certain variance among samples.

A. Real-time FTIR measurement

The curing kinetics of UV curable acrylates and epoxies was analyzed with the real-time FTIR technique, as shown in shown in **Figure 3.4**. UV irradiation from a mercury lamp with a light intensity of $200 \mu\text{W}/\text{cm}^2$ was introduced to the FTIR chamber. A UV curable film was sandwiched between two salt plates separated by a $25 \mu\text{m}$ spacer as described above. The liquid film was exposed to UV light and IR spectra were taken continuously during UV curing, enabling the analysis of curing kinetics in real-time.

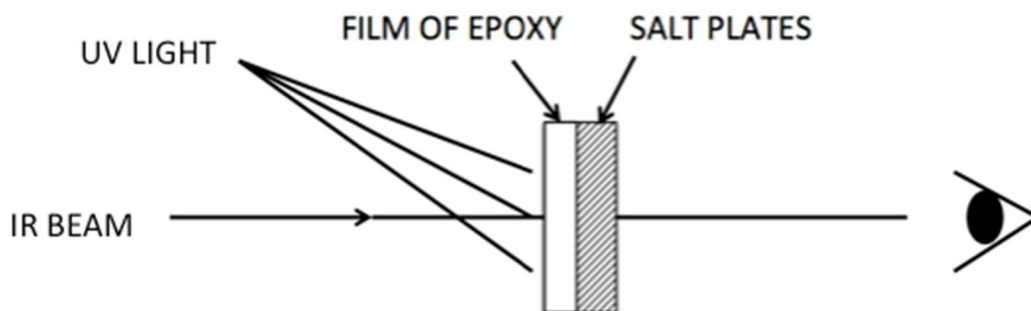


Figure 3.4 Schematic of real-time FTIR measurement

The extent of cure (x), measured by the fractional conversion of acrylate double bonds, was calculated from the drop in the absorption of C=C characteristic peaks at 1635 and 1619 cm^{-1} (symmetric C=C stretch and asymmetric C=C stretch) :

$$x = \frac{A_0 - A_t}{A_t} \times 100\% \quad \text{Equation 3.1}$$

where A_0 represents the absorption of double bonds before IPL curing and A_t represents that after IPL curing^{28, 96}. The absorption value, proportional to the double bond concentration in the sample, was calculated by integrating the area

under both peaks from 1660 to 1580 cm^{-1} (where the photoinitiator has negligible IR absorption) for acrylates. For epoxy-based coatings, the epoxy functional group shows a characteristic peak at 790 cm^{-1} , which was used for the conversion analysis.

B. Final conversion measurement

In the evaluation of conversions for coatings cured with the xenon flash lamp, IR spectra of each sample were recorded before and after IPL curing, respectively. It should be noted that to eliminate the effects of coating thickness on the IR signal and thus the calculated conversion. The C=O peak at 1720 cm^{-1} was used as an internal reference peak because the concentration of carbonyl groups remain constant during UV curing. Additionally, the final conversions measured with the transmission mold are the averaged conversion across the coating thickness.

C. Evaluation of the conversion gradient

Both FTIR-ATR and confocal Raman microscopy could be used for the evaluation of the conversion gradient across the coating thickness. In the FTIR-ATR measurement, samples are pressed against the ATR crystal. IR beam hits the sample surface and the reflected IR signal was measured, as is shown in **Figure 3.5**. Due to the limited penetration depth of IR beam within samples (typically on the order of 100 μm), the measured conversion corresponds to the curing extent of the surface layer. In this chapter, the top and bottom surfaces of a

cured coating were measured with the ATR technique and compared to evaluate the uniformity in the degree of cure.

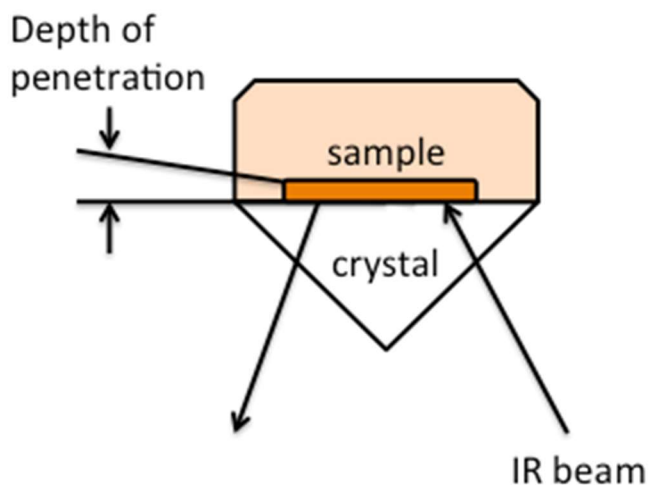


Figure 3.5 Schematic of ATR measurement.

Confocal Raman microscopy is another powerful tool to study the depthwise conversion gradient of UV curable materials. It combines the spatial resolution of confocal microscopy with the chemical information of vibrational spectroscopy.⁹⁷ The Raman intensities of a functional group scale with its concentration and also depend on the position of the characteristic peak in the Raman spectrum. By comparing the Raman spectrum of the uncured coating formulation with that of a cured coating, we can calculate the relative conversion of a functional group. In this section, the Raman microscope is equipped with an argon laser (Omnichrome, CA) at a wavelength of 532 nm. The spectrum was collected using a grating with 600 g/mm. Computer controlled movement in the z-direction of the microscope results in a depth profiling of the UV crosslinking reaction. The double bond conversion was analyzed using its characteristic peak

at 1635 cm⁻¹. In addition, the peak for the carbonyl group at 1725 cm⁻¹ was utilized as an internal reference.

3.2.4 Heat Transfer Analysis

The heat transfer equations describing the heat generation during IPL curing of the TMPTA coatings were solved using a heat transfer model within the COMSOL software package (version 4.4) in a similar manner to ⁹⁸. The model substrate configuration used for simulations comprised, from top to bottom, a 4 mm NaCl layer, a 25 µm TMPTA layer, and a 4 mm NaCl layer. Upon these geometries, the maximum element sizes were limited to 0.1 µm in the TMPTA layer and 20 µm in the NaCl layers. The top surface of the structure was allowed to cool through convective heat transfer with the surroundings at a temperature of 293.15 K with an assumed heat transfer coefficient of 10 W/m²·K. The bottom surface of the model structure was assumed to be held at a constant temperature, T = 293.15 K, due to its contact with a solid surface which acts as a heat sink. The pulse duration of 100 µs and the pulse period of 1 s were used to simulate heating from 10 lamp pulses during IPL curing. The heat generation from nonselective light absorption was negligible compared to the heat from the reaction. The heat flux \dot{q} resulting from polymerization was calculated according to the following equations:

$$\dot{q} = \frac{\alpha \Delta H_{TMPTA}}{\Delta t} \quad \text{Equation 3.2}$$

$$\Delta H_{TMPTA} = \Delta H_{C=C} \times \frac{\rho}{M} \times f \quad \text{Equation 3.3}$$

where α is the degree of conversion (using results from FTIR experiments), ΔH_{TMPTA} is the heat of polymerization of TMPTA monomers per unit volume (0.872 kJ/cm³), Δt is the flash duration (100 μ s), $\Delta H_{C=C}$ is the molar heat of polymerization of carbon double bonds (78.2 kJ/mol), ρ is the monomer density (1.102 g/cm³), M is the monomer molecular weight (296.32 g/mol), and f is the acrylate functionality of TMPTA (3).

The temperature profile during 10 pulses was simulated with the following heat flux values for each pulse: 1.57×10^{12} , 1.31×10^{12} , 4.36×10^{11} , 4.36×10^{11} , 4.36×10^{11} , 5.23×10^{10} , 5.23×10^{10} , 5.23×10^{10} , 5.23×10^{10} , 5.23×10^{10} W/cm². These values were calculated with Equation 3.2. To accurately model the rapid transient heating during each pulse, the simulation time-steps during pulses were set to 10^{-6} s; time steps were increased to 50 ms when the pulse was off.

3.2.5 UV-Vis spectroscopy

A thin layer of UV curable formulation containing 0.05 mol% PI was placed between two salt plates separated by a 25 μ m thick spacer. The UV-vis spectra were measured on both uncured and cured samples. Samples cured with a xenon flash lamp curing and the mercury lamp were compared. The sample was placed into a UV spectrometer and the UV absorption in the wavelength range of 200 to 800 nm was measured. Because of our acrylate coating system the photoinitiator DMPA shows strong UV absorption at 250 nm, this peak was utilized to quantify the concentration of PI in the system.

3.3 Results and Discussion

3.3.1 Comparison of acrylate and epoxy curing kinetics with a mercury lamp

The curing kinetics of both acrylate and epoxy-based coatings were investigated with real-time FTIR. It should be noted that in this section, UV curing was carried out with a low-intensity mercury lamp at a light intensity of $200 \mu\text{W}/\text{cm}^2$ and a peak wavelength of 365 nm. This light source was selected to allow for real-time measurements and the trend observed can shed light on the interpretation of results obtained with a xenon flash lamp. Figure 3.6 shows the FTIR spectrum of TMPTA before UV curing and the inset shows the characteristic peaks for acrylate double bonds. Upon UV illumination, the peak intensity decreased because the double bonds were consumed during the photopolymerization process. Plotting the double bond conversion as a function of UV curing time gives us the curing kinetics curves shown in Figure 3.7.

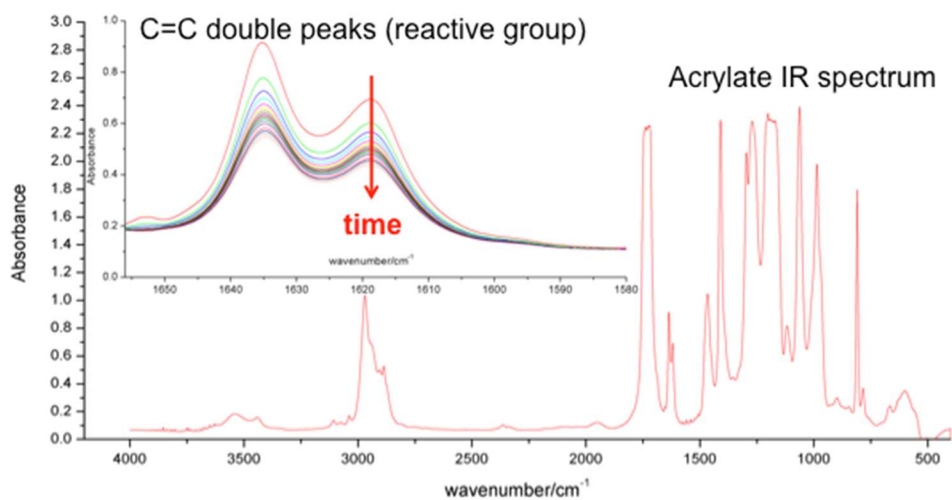


Figure 3.6 Real-time FTIR spectra of acrylates under UV illumination.

The inset shows the characteristic peaks for acrylate double bonds at 1620 and 1635 cm^{-1} , the peak intensity of which decreases with the curing time due to the consumption of double bonds.

From Figure 3.7, we noticed that the polymerization of acrylate monomers proceeded very rapidly upon illumination and then slowed down due to solidification of the system, characteristic of the curing of multifunctional monomers.⁹⁹ Solidification conversion could be found at the inflection point of the curve and was determined to be ca. 35%. Furthermore, the conversion of the acrylate system leveled off at around 52%, because the mobility of reactive species was severely restricted in the highly cross-linked polymer networks. These results are consistent with previous kinetic studies on TMPTA coatings, where the final conversion was found to be in a range from 46% to 48%.²⁸

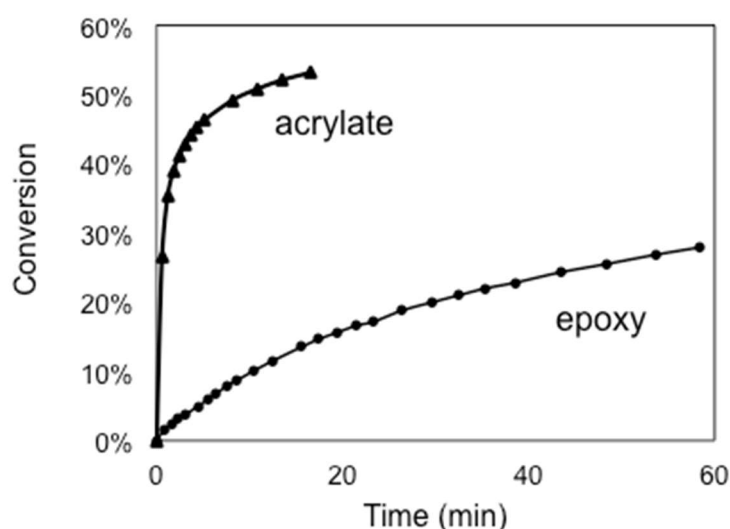


Figure 3.7 Comparison of curing kinetics of acrylate and epoxy under the exposure of a mercury lamp.

For both the acrylate and the epoxy samples, the coating thickness was 25 μm and the curing conditions were mercury lamp curing at 365 nm and 200 $\mu\text{W}/\text{cm}^2$ intensity.

The measurement of conversion in the epoxy system was based on changes in the concentration of epoxide rings. The absorbance of the characteristic peak at 790 cm^{-1} was monitored to track the conversion of epoxy

resin by real-time FTIR. As expected, the epoxy system based on cationic polymerization cured much slower than the acrylate system. As depicted in Figure 3.7, the conversion increased gradually throughout curing process and reached 28% after 1h. A previous study on the same epoxy system showed a similar conversion profile but a lower final conversion due to different curing conditions.²⁹ Therefore, the UV curing of epoxies under ambient conditions were much slower compared to acrylates, which is in good agreement with previous studies.

3.3.2 Single pulse curing

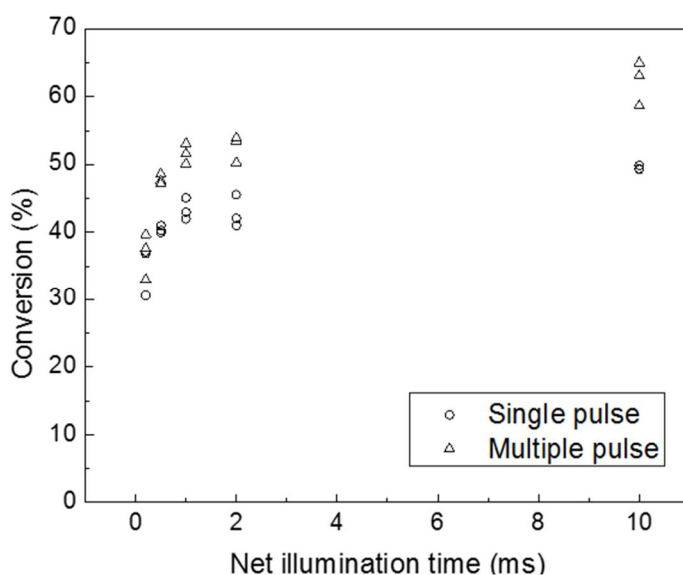


Figure 3.8 Conversion versus the net illumination time for the single pulse curing and the multiple pulses curing of TMPTA coatings.

Single pulse exposed coating was cured at 2.2 kV lamp voltage and 0.5 mol% PI concentration. Multiple pulse cured coating contained 0.5 mol% PI and was illuminated at 2.2 kV lamp voltage, 100 μ s pulse width and 1 s pulse period. Three samples were tested for each irradiation condition.

A single pulse with various pulse duration was used to cure the TMPTA coating and the resulting extent cure of a coating was measured with FTIR. As is shown in **Figure 3.8**, the double bond conversion of acrylate coatings depends on the net illumination time, which develops rapidly at early stages of curing and then increases much slower after 1 ms of irradiation. Such a trend in conversion development is typical of the UV curing of acrylate systems ^{27, 28, 100}. It is thought that free radicals grow extensively upon illumination, after which cross-linking will slow down the diffusion of radicals and monomers, resulting in a drop in the conversion rate ⁴⁴.

The double bond conversion of single pulse curing reached a maximum achievable value of 50% with only 10 ms of illumination. To our knowledge, it is the first time that the xenon flash lamp curing of UV curable resins within milliseconds has been reported. In comparison, the achievable conversion recorded for a less powerful light source (a mercury lamp with a wavelength of 365 nm and an intensity of 4 mW/cm²) is 48.8% after 5.2 minutes of exposure, measured using photo-differential scanning calorimetry under nitrogen ²⁷. The IPL curing speed is several orders of magnitude higher than that of mercury lamps, as fast as the ultrafast polymerizations induced by laser beams ⁴⁴. Such a high curing speed could be attributed to a much higher light intensity in consideration of the following expressions of the polymerization rate (R_p):

$$R_p = \frac{k_p}{(2k_t)^{0.5}} [M] R_i^{0.5} \quad \text{Equation 3.4}$$

$$R_i = 2\phi_i I_a \quad \text{Equation 3.5}$$

where k_p is the propagation rate constant, k_t the termination rate constant, $[M]$ the monomer functional group concentration, R_i the initiation rate, φ_i the composite initiation quantum yield, and I_a the absorbed light intensity. These idealized equations assume a pseudo-steady state and bimolecular termination only. They clearly reveal that the curing speed is enhanced in a wide range by simply increasing the light intensity. We do not employ these equations directly however, because I_a is unknown.

The results also suggest that IPL does not significantly improve the achievable conversion of TMTPA monomers. Previous studies carried out with conventional mercury lamps, however, have shown the achievable conversion increases with the light intensity and explained it by two possible hypotheses: a greater excess free volume^{27, 53, 54} and a rise of the sample temperature⁵⁵. According to the excess free volume theory, as the polymerization rate increases with the light intensity, the actual specific volume of the polymer network is not able to shrink as fast as the thermodynamic equilibrium specific volume. The generated excess free volume enhances the mobility of reactive species and therefore leads to a higher maximum achievable conversion. The hypothesis concerning the temperature rise suggests that the intensity effect on conversion results from a higher sample temperature, which increases molecular mobility. In our experiments with IPL, the failure to observe higher achievable conversions supports the latter hypothesis. Although the pulsed light intensity is much higher than that of mercury lamps, the sample temperature remains nearly constant during IPL curing because of the effective heat transfer from coating to salt plates

and of the fact that a measured single pulse can avoid significant heat accumulation from excessive exposure.

3.3.3 *Multiple pulse curing*

In an industrial roll-to-roll process, coatings are exposed to short periods of UV light from successive UV lamps to achieve sufficient curing dose at high web speeds, so the curing of coatings actually takes place under a multiple-pulse irradiation condition. A comparison between single pulse curing and multiple pulse curing based on the same irradiation dose was made to investigate the effect of dark periods on the curing of TMPTA coatings (**Figure 3.8**). In the experiment, samples were exposed to different numbers of pulses, with a pulse duration of 100 μ s and a pulse period of 1 s. The irradiation dose is directly proportional to the net illumination time, which is the product of the pulse duration and the pulse number according to:

$$\text{Irradiation dose} = f(\text{voltage}) \times \text{pulse duration} \times \text{number of pulses} \quad \text{Equation 3.6}$$

where f is a linear function relating the dose rate with the lamp voltage. Similar to the trend observed in single pulse curing, the conversion of multiple pulse curing increases with the net illumination time and then reaches a plateau value at 2 ms of illumination (20 pulses), which agrees with previous results of Stropp⁹⁰ and Magg⁹¹.

Hypothesis tests were performed to justify whether the average conversions curing at the same irradiation dose are the same for the single pulse

curing and the multiple pulse. A difference in mean test based on t-statistic was used, where the null hypothesis is that two averages are the same. Test results, shown in Table 3.1, suggest that the average conversions are statistically different for the two curing patterns, except for the case of the shortest illumination time. For the multiple pulse curing, the achievable conversion at a given irradiation dose is higher due to the introduction of dark periods between pulses. This might be explained by two reasons: the possibility of bimolecular termination of free radicals is reduced compared to the single pulse curing, where a large number of radicals are initiated in an extremely short period of time; the free radical polymerization proceeds efficiently during dark periods.

Table 3.1 Hypothesis tests for the equality of sample means of single pulse curing (SP) and multiple pulse curing (MP) at different net illumination times (t).

t, ms	Average conversion, %		Standard error, %		Degree of freedom	Calculated t-statistic	Critical t-value	Test result
	SP	MP	SP	MP				
0.2	35	37	2.2	2.0	6	0.65	1.9	Accept
0.5	40	48	0.30	0.42	5	14	2.0	Reject
1	43	52	0.91	0.87	6	6.5	1.9	Reject
2	43	53	1.4	1.1	6	5.4	1.9	Reject
10	50	62	0.19	1.9	3	6.8	2.4	Reject

^a The critical t-values are obtained from the t-table at 10% level of significance with the corresponding degree of freedom.

The following discussion focuses on IPL curing where the total irradiation dose is delivered in multiple pulses and explore the effects of various processing variables on the extent and speed of curing, including the lamp voltage, the pulse duration, the pulse period, PI concentration, and temperature. To facilitate

discussion, experimental conditions of a base case are listed in Table 3.2; thereafter, the effects of changing processing variables from the base case are discussed.

Table 3.2 Base case experimental conditions

Pulse number	Voltage	Pulse width	Pulse period	PI concentration	Temperature
20	2.2 kV	100 μ s	1 s	0.5 mol%	25 °C

3.3.4 Effects of irradiation dose rate

The irradiation dose rate in IPL curing is determined by three processing variables, the light intensity, the pulse duration and the pulse period:

$$\text{Irradiation dose rate} = f(\text{voltage}) \times \text{pulse duration} / \text{pulse period} \quad \text{Equation 3.7}$$

The effects of irradiation dose rate on the speed and the extent of cure were evaluated by tuning these three variables independently.

Table 3.3 Irradiation dose rate and achievable conversion

Curing condition	Voltage, kV	Pulse period, s	Pulse duration, ms	Pulse number	Curing time, s	Conv. 1, %	Conv. 2, %	Conv. 3, %	Average conv., %
Base case	2.2	1	0.1	20	20	51.4	50.1	50.6	51
Voltage-1	1.8	1	0.1	20	20	45.8	48.0	46.5	47
Voltage-2	2.6	1	0.1	20	20	53.3	50.9	55.0	53
Voltage-3	3	1	0.1	20	20	53.2	54.7	54.0	54
Period-1	2.2	0.1	0.1	20	2	53.7	47.1	51.0	51
Period-2	2.2	0.5	0.1	20	10	51.9	50.2	51.6	51
Period-3	2.2	5	0.1	20	100	50.1	53.5	52.7	52
Duration-1	2.2	0.1	0.2	10	1	49.6	52.8	54.9	52
Duration-2	2.2	0.5	0.2	10	5	53.2	54.3	53.7	54
Duration-3	2.2	1	0.2	10	10	52.3	53.5	54.5	53

^a The base case is included in the discussion of each independent variable (voltage, pulse period and pulse duration).

As the average dose rate rises with an increase in voltage, as is shown in Table 3.3 curing conditions of voltage-1, 2 and 3, the average double bond conversion is hardly changed. A similar result was observed previously in continuous intense UV light curing systems^{44, 56}, while for UV curing at low intensities it was shown that the increasing the light intensity is more effective in enhancing the achievable conversion²⁷. Considering the decomposition of DMPA proceeds rapidly under intense illumination, one of the possible reasons for the saturation of the intensity effect is that PI is exhausted at a relatively low voltage (2.2 kV), leaving the polymerization reaction insensitive to any further increase in voltage.

In roll-to-roll applications, the pulse duration is determined by the lamp geometry and the pulse period depends on the distance between lamps, and therefore the optimization of these two variables has significant practical implications for the design of coating production lines. In IPL curing of the TMPTA coatings, we used various pulse periods and kept all the other curing variables the same (curing conditions of period-1, 2 and 3 in Table 3.3 Irradiation dose rate and achievable conversion). In additional experiments to evaluate the role of pulse duration, the pulse duration was doubled while the number of pulses was reduced by half to keep the total dose invariant, i.e. 10 flashes of 200- μ s-long pulses were used to cure coatings (curing conditions of duration-1, 2 and 3 in Table 3.3). Despite a wide variation in the pulse period and the pulse duration, the conversion data cluster tightly around a value of 50%. The result reveals that the details of how the energy is delivered in IPL do not significantly affect the

final conversions of TMPTA coatings. Similarly, Vaessen *et al.* studied the effects of lamp cycling in the UV-cured TMPTA coating system with longer cycle times of several minutes, suggesting that the curing conversion did not change with the cycle time ²⁸.

The IPL curing speed, however, increases significantly with the average curing rate - higher lamp voltage, longer pulses, and shorter pulse duration - considering the irradiation dose to attain the maximum achievable conversion is approximately constant for curing a specific coating system at ambient temperature. For instance, under the curing condition of duration-1, coatings can be fully cured in only a second without sacrificing the extent of cure, which is the fastest IPL curing case in our Sinteron-cured TMPTA system. It is possible that some other multiple pulse patterns (e.g., with shorter dark periods and fewer pulses) may still have benefits, but we have not sought to optimize this. These experimental results present a simple rule for the selection of variables in IPL curing processes to improve curing throughput and serve to practically guide the design of industrial roll-to-roll lines.

3.3.5 *Effects of PI concentration*

Approaches to cure coatings with low PI concentrations or without PI have been attractive to researchers to reduce the formulation cost, toxic PI residues and the depthwise conversion gradients in cured coatings ²⁹. We investigated the effects of PI concentration in IPL curing, varying the PI concentration from 0.05 mol% to 5 mol% and keeping all the other curing

conditions the same. As is shown in Figure 3.9, for TMPTA coatings containing 0.05 mol% PI, 41% of double bonds on average are consumed after 20 pulses of illumination; the reaction continues given more UV light, yielding an average conversion of 48% at 40 pulses. At such a low PI concentration, it is suggested that the photopolymerization evolves at a lower speed due to a decreased initiation rate, but it will reach a similar achievable conversion. For coatings containing 5 mol% PI, the 10-fold increase in PI concentration leads to only a 4% increase in the averaged conversion compared to the base case (53% vs. 57%). It is suggested that IPL curing process has the potential to attain the same achievable cure with low PI concentrations, which could be attributed to high initiation efficiency with such a bright light source.

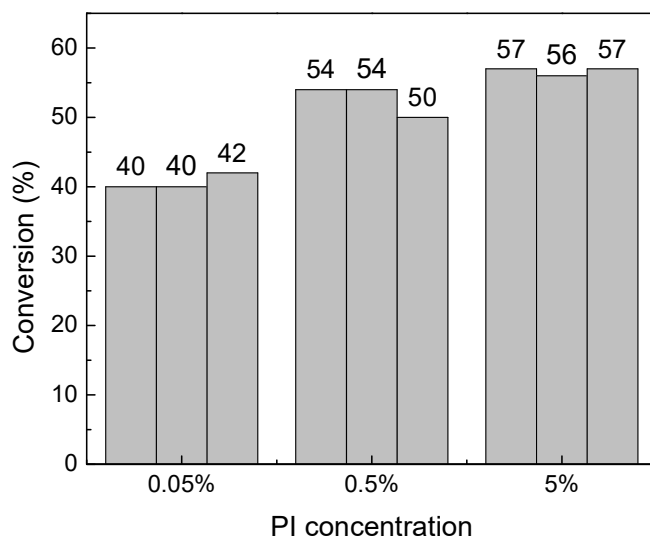


Figure 3.9 Conversion versus PI concentration for TMPTA coatings.

Coatings were cured at 2.2 kV, 100 μ s pulse width, 1 s pulse period and 20 pulses. The three bars for each PI concentration are results of parallel measurements on different samples. All samples were irradiated to the same total dose.

3.3.6 Effects of temperature

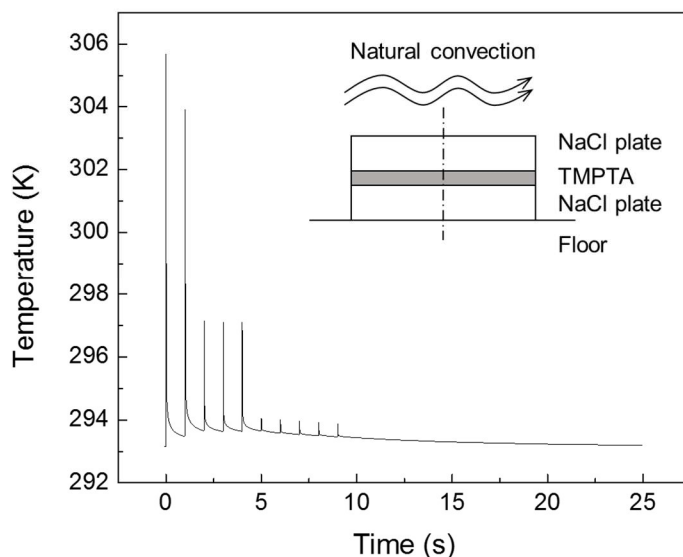


Figure 3.10 Temperature profile in IPL curing of a TMPTA film sandwiched between two NaCl plates.

Curing conditions: 2.2 kV, 100 μ s pulse width, 1 s pulse period, 10 pulses and 0.5 mol% PI concentration. Inset: schematic of the theoretical heat transfer model for calculation of the temperature of IPL cured TMPTA film.

During IPL curing process, the intense pulses initiate photopolymerization that generates a great amount of heat in a very short time, while the dark periods between pulses facilitate cooling of the sample. Knowledge of the sample temperature evolution is critical to UV curing processes at that temperature has a strong influence on both the curing speed and the curing extent ⁴⁴.

Figure 3.10 shows the temperature profile of a TMPTA coating between two salt plates during 10 pulses of exposure, simulated using the finite element method (FEM). According to Figure 3.10, the coating temperature rises instantaneously upon illumination and returns rapidly to ambient temperature between pulses due to an effective heat transfer to NaCl plates as well as air-

cooling. During each pulse, IPL is a largely adiabatic process because the heat generation within the sample is much faster than the heat transfer between the sample and the environment. Thus, the released heat of polymerization is converted to the heat inside the coating, resulting in a temperature rise proportional to the polymerization rate. In our system, the highest temperature is reached during the first pulse, leading to a maximum temperature increase of 13 degrees. After 5 pulses, a nearly flat temperature profile is obtained upon illumination. Therefore, it is proved that the combination of extremely short pulses and dark periods of IPL can effectively avoid heat build-up on the substrate.

Experiments have been carried out to investigate the effects of temperature on the achievable conversions of IPL cured acrylate coatings. TMPTA coatings were irradiated at 25°C, 40°C, 55°C and 70°C, respectively, and the net temperature rise during curing was expected to be similar in all cases. A higher achievable conversion was observed when the curing temperature was raised to 55°C, as is shown in Figure 3.11. According to past work on continuous irradiation of low-viscosity UV-curable systems, the kinetics of photopolymerization is similar at different temperatures and the achievable conversion is closely related to the maximum temperature in sample ⁵⁵. For the TMPTA coating cured at 55°C under IPL, the estimated maximum temperature (estimated to be 68°C from the FEM simulation) exceeds the typical glass transition temperature of cured TMPTA coatings (62°C), so the higher achievable conversion may result from the softening of polymerized coating networks and therefore an enhanced mobility of reactive species.

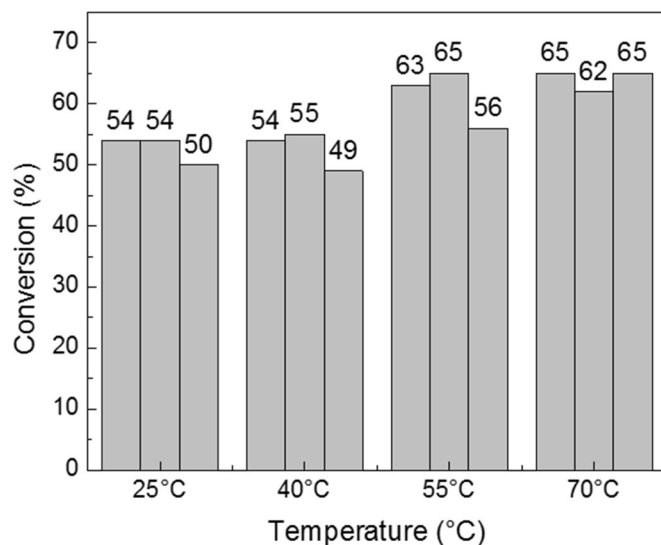


Figure 3.11 Conversion versus curing temperature for TMPTA coatings.

Coatings were cured at 2.2 kV, 100 μ s pulse width, 1 s pulse period, 20 pulses and 0.5 mol% PI concentration. The three bars for each temperature are results of parallel measurements on different samples. All samples were irradiated to the same total dose.

However, a further increase in temperature shows a negligible effect on improving the achievable conversion. Such a temperature saturation effect could be attributed to the strong steric hindrance rooted in the chemical structure of the polymer networks or the fact that the chain transfer reaction dominates over chain propagation at high temperatures ¹⁰¹.

3.3.7 PI Consumption

Upon UV illumination, photoinitiators will undergo photolysis to generate free radicals and initiate photopolymerization. Considering the process throughput, a high PI concentration is desired because the resulting higher radical concentration leads to increased reaction speed. However, as a result of high PI

concentrations, the residual PI concentration is also higher, which can affect the long-term stability of UV curable materials. Upon further illumination to UV light, residual PI can cause hardening of the materials, degradation, or yellowing of the cured material. Therefore, complete consumption of PI is a critical criterion for UV curable system.

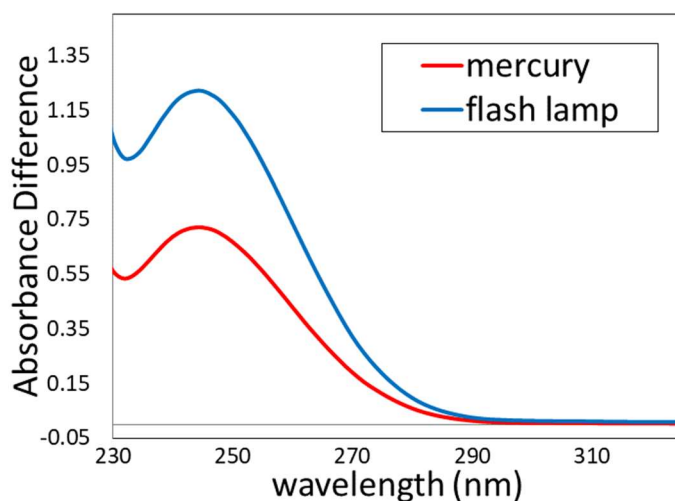


Figure 3.12 PI loss during UV curing for TMPTA coatings.

The curves shown in this figure correspond to the absorption difference between uncured and cured TMPTA coatings due to the photolysis of DMPA upon UV exposure. Different curing conditions were compared: mercury lamp curing for 15 min at $200 \mu\text{W}/\text{cm}^2$ and flash lamp curing for 20 flashes with a flash duration of $100 \mu\text{s}$ and a flash spacing of 1 s.

The UV-vis spectra of both uncured and cured TMPTA coatings were characterized. DMPA has a strong UV absorption at a wavelength of 250 nm. Upon UV illumination, DMPA undergoes a photobleaching process where the PI molecules decompose and the produced photoproducts have negligible absorption in this range. Therefore, the intensity of the absorption peak at 250 nm decreased after UV curing. By comparing the UV-vis spectra before and after UV curing, the absorption difference is proportional to the PI loss during UV curing.

According to Figure 3.12, the absorption difference was larger for the flash lamp cured coating compared to that cured with a mercury lamp, suggesting that more PI was consumed during flash lamp curing. This can be explained by the fact that the high intensity of Sinteron leads to a higher initiation rate and a lower residual level of DMPA, which is beneficial for various applications with high requirements in the long-term stability.

3.3.8 Depthwise curing gradient

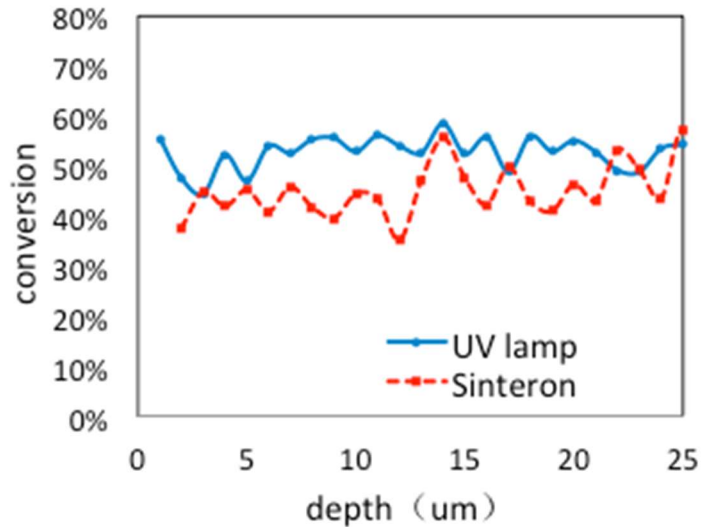


Figure 3.13 Depth profiles of curing conversion of TMPTA coatings cured with a mercury UV lamp and a xenon flash lamp, respectively.

For UV curable coatings, depthwise curing gradient may develop due to two main reasons: oxygen inhibition and UV light attenuation. First, it is widely known that a potential problem with UV curable acrylate coatings is the insufficient surface cure resulting from the oxygen inhibition problem. As the result, the coating surface might be tacky or the elastic modulus is lower

compared to the bulk modulus of the materials. Second, according to the Beer-Lambert law, the UV light intensity decreases with the penetration depth into the system, leading to a reduced curing content with increase in the coating thickness. The conversion gradient across the coating thickness can lead to the development of internal stress and thus wrapping or cracking of UV curable coatings.

In the xenon flash lamp curing, the depthwise conversion gradient is expected to be lower because of a high light intensity and emission of long-wavelength UV irradiation. The high UV intensity can lead to fast polymerization, which suppresses the diffusion of oxygen into the materials. In addition, the emission spectrum of a xenon lamp covers the long wavelength irradiation that penetrates deeper into the coating.

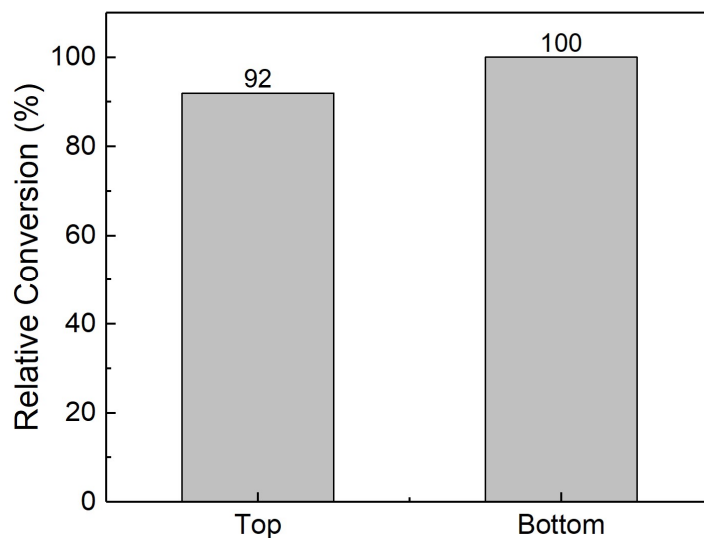


Figure 3.14 Top and bottom conversions measured with the FTIR-ATR technique.

Coatings were exposed to a xenon flash lamp for 20 pulses at a pulse width of 100 μ s and a pulse duration of 1 s.

Raman microscopy was used to evaluate the conversion of the TMPTA coating as a function of the depth. The effects of the light source on the conversion gradient were investigated by comparing coatings cured with a xenon flash lamp and a mercury pencil lamp, respectively. In both cases, coatings were exposed to sufficient dosage to ensure the UV curing was complete. For the xenon lamp curing, the sample was exposed to 20 pulses at a pulse width of 100 μ s and a pulse width of 1 s. For the mercury lamp curing, the sample was exposed to the UV pencil lamp for 15 min at a light intensity of 200 μ W/cm². Figure 3.13 show that the curing extent was constant across the coating thickness for TMPTA coatings cured with the mercury UV lamp and Sinteron. It is suggested that for clear formulations at a small coating thickness (25 μ m), sufficient cure throughout the coating is not a problem. This was further confirmed using the FTIR-ATR technique where the top and the bottom of a cured coating was characterized respectively. As is shown in Figure 3.14, relative to the bottom conversion, the curing extent of the coating surface is 92%, indicating a high degree of uniformity across the coating thickness.

3.4 Summary

In this chapter, IPL curing of a model acrylate system of TMPTA monomers has been investigated with a xenon flash lamp and FTIR spectroscopy. In all cases, cure conversion increases with the number of pulses until it plateaus at the maximum achievable value when the reduced mobility of reactive species prevents further reaction. Changing the pulse intensity, the pulse duration, and

the pulse period - and even changing the photoinitiator loading - do not appreciably affect the achievable conversion at ambient temperature. Increasing the temperature can result in somewhat higher achievable conversion, but with the loss of advantages of ambient temperature cure. Consistent with the expectation that the cure rate should depend strongly on intensity, a single measured pulse with high dose rate can achieve millisecond-timescale cure of acrylate coatings, providing adequate curing dose while avoiding damage to the substrate from excessive exposure. In multiple pulse patterns, the achievable cure can be attained more quickly with higher dose rate; as opposed to a single pulse irradiation, the introduction of dark periods can reduce the total irradiation dose needed to attain the achievable cure conversion.

4 Modulus- and Surface Energy-Tunable Thiol-ene for UV Micromolding of Coatings*

4.1 Background and Motivation

The fabrication of nano/micro scale surface structures is essential to a variety of applications, including textured coatings^{102, 103}, optical films¹⁰⁴, superhydrophobic surfaces¹⁰⁵, and flexible electronics^{61, 79}. Photolithography, a conventional nanofabrication technique, involves curing through a photomask to achieve the spatially selective reaction of photoresists and a subsequent developing step to remove unreacted materials. The development of photolithography for the mass production of structured surfaces is limited due to the waste involved with etching and its stringent requirements on processing conditions. Nanoimprint lithography has received growing research interests as an alternative lithographic technique.^{82, 83} Unlike photolithography, it creates a surface pattern based on the mechanical deformation of materials using a stamp with surface relief structures, followed by pattern solidification assisted with either heat or ultraviolet (UV) exposure.

*Reproduced in part with permission from (Y. Du, et al., “Modulus- and surface energy-tunable thiol-ene for UV micromolding of coatings”, *ACS Appl. Mater. Interfaces* **2017**, 9(29), 24976-24986.)

While nanoimprint lithography mainly focuses on the fabrication of nanostructures and involve etching to transfer patterns from photoresists to the underlying rigid substrate, micromolding of UV curable materials (UV micromolding) is promising for microscale applications in which the final structured coating is the aim of the process. In micromolding, a liquid UV curable coating is deposited onto a substrate, a flexible mold with microscale features is then pressed into conformal contact with the coating, UV exposure solidifies the coating with the mold in place, and the mold is peeled off to obtain a coating with surface structure.¹⁰⁶ With the application of roller molds, UV micromolding is compatible with continuous roll-to-roll (R2R) processes and large area substrates.^{107, 108} Although processing rates on the order of meters-per-minute have been reported for continuous versions of imprint processes¹⁰⁹, improvements in throughput are needed for UV micromolding processes to be viable for mass production. Key challenges in boosting the throughput include the complete filling of mold cavities, the fast curing of coatings, and the clean release of surface microstructures, all of which are closely related to the development of new UV-curable materials with specific characteristics.⁸³

Acrylates and epoxies are the widely used UV curable materials for coating applications and potential candidates for UV micromolding. Acrylates have high curing speeds and desirable physical properties, such as hardness, and a large variety of acrylate monomers and oligomers are commercially available to fulfill application-specific requirements.^{19, 110, 111} For UV micromolding, however, acrylates have two main disadvantages. First, due to their free-radical, chain-

growth photopolymerization mechanism, the curing of acrylates is inhibited by oxygen and thus may lead to uncured edges under ambient curing conditions. Second, high levels of volume shrinkage during curing limit the accuracy of replicated patterns and leads to stress that can cause cracking or distortion of the final product. The photoreaction of epoxy, proceeding via the cationic, step-growth photopolymerization, is insensitive to oxygen and develops less shrinkage during curing.¹¹² However, the curing speeds of epoxy resins are generally lower, and their viscosities are higher compared to those of acrylates.

As an alternative class of UV curable materials, the thiol-ene chemistry is mediated by the free-radical, step-growth photopolymerization and displays many properties desirable for high-throughput UV micromolding applications.^{17, 99} Beneficial from the free-radical scheme, thiol-ene systems undergo a rapid photopolymerization process at ambient temperatures. At the same time, due to the step-growth nature, photoreactions of thiol-ene are insensitive to oxygen and generate polymer networks with a high homogeneity and less volume shrinkage. Furthermore, acrylates can be incorporated into the thiol-ene reactions, which homopolymerize among acrylate double bonds or partly react with thiol groups, depending on the specific chemistries utilized.^{34, 35, 113} While preserving the advantages of the thiol-ene chemistry, thiol-ene-acrylate coatings enjoy an extended range of material properties provided by a large number of commercially available acrylates.

Previously, Carter and coworkers^{42, 43, 114} have reported the pattern replication capability of thiol-ene coatings in imprint lithography, while Lin et

al.^{41, 115} extended the coating chemistry to siloxane-containing monomers to fabricate microstructures with enhanced etch resistance and thermal stability. However, these studies have not focused on the optimization of curing conditions and thus do not fully reflect the compatibility of thiol-ene with R2R processing. Quite recently, Stadlober and coworkers¹¹⁶ utilized coating systems based on polyurethane acrylate oligomers and thiol monomers in R2R imprinting processes and fabricated surface patterns with multi-length scales at large areas. Furthermore, most previous studies only addressed the fabrication of shallow features (less than 1 μm in height) and the complete displacement of liquid UV curable materials from beneath the stamp to facilitate subsequent etching. The replication of microscale features with high aspect ratios still presented a substantial processing challenge. Patterned coatings can be deformed or torn off from the substrate due to the strong interaction between the coating and the mold in the presence of interfacial microstructures. Although coatings with low surface energies were utilized to reduce demolding-related defects for nanoscale features^{115, 116}, the roles of material properties in replicating features in micron size scales were not fully understood. Experimental investigations of the demolding force have been limited to nanoimprinting processes, where the whole mold is separated from a nanostructured coating in a normal separation direction.¹¹⁷⁻¹¹⁹ In practical applications, especially a roll-to-roll process, the peeling separation is preferred over the normal separation because of a much smaller peeling force and the roller geometries. Peel tests have been widely used in determining the interfacial strength between polymer-polymer surfaces and a

recent work successfully applied it to study the geometrical effects in the peeling of a commercial adhesive from patterned PDMS surfaces.¹²⁰ Therefore, conventional peel tests provide an effective method to measure the demolding strength in UV micromolding processes.

In this chapter, a pattern replication approach utilizing the thiol-ene photopolymerization and the micromolding process with a UV LED light source was reported. With 10 seconds of UV LED exposure, microscale gratings with a high pattern density were replicated at high accuracy in thiol-ene coatings. The thermomechanical properties of cured coatings were easily adjusted over a wide range by changing the acrylate content in the formulation, covering properties of stiff polymer networks and soft materials. The surface energy of a thiol-ene coating was significantly reduced through the introduction of a fluorinated polymer at a 1 wt% loading. Surface microstructures with higher aspect ratios were attainable with the fluorinated coating formulation, which were subject to failures during demolding in coatings without the fluorinated additive. The demolding behaviors of micro-gratings were quantitatively evaluated in 90° peel tests, while the coating properties and the pattern geometries were adjusted in isolation. It was found that the demolding strength increased with the coating surface energy, Young's modulus, and the pattern height.

4.3 Materials and Methods

4.3.1 Thiol-Ene-Acrylate Coating Formulation

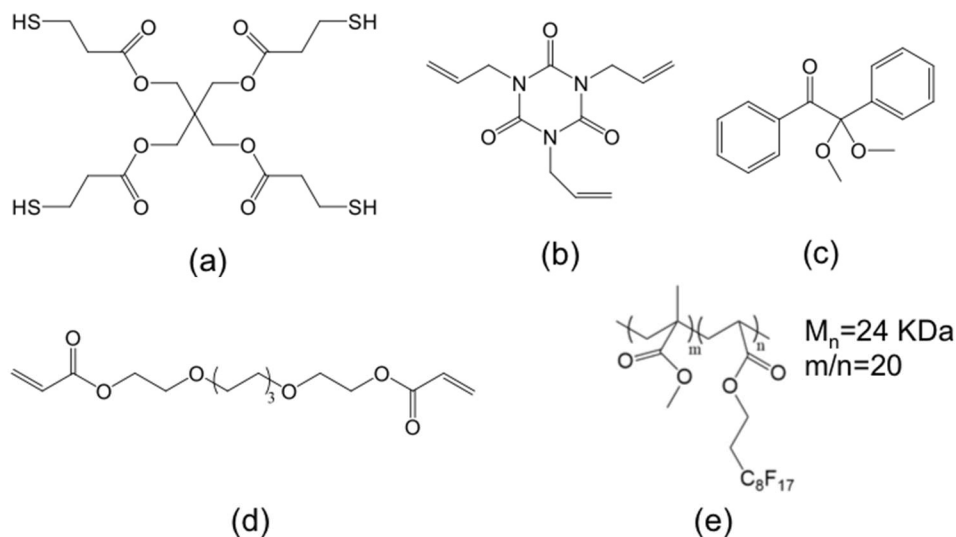


Figure 4.1 Chemical structures of materials employed in coating formulations.

(a) pentaerythritol tetrakis(3-mercaptopropionate) (PTMP), (b) 1,3,5-triallyl-1,3,5-triazine-2,4,6(1H,3H,5H)-trione (TTT), (c) 2,2-dimethoxy-2-phenylacetophenone (DMPA) (d) 1,6-hexanediol ethoxylate diacrylate (HEDA), and (e) fluorinated acrylate copolymer (F-PMMA).

Figure 4.1 shows the chemical structures of materials. Pentaerythritol tetrakis(3-mercaptopropionate) (PTMP), 1,3,5-triallyl-1,3,5-triazine-2,4,6(1H,3H,5H)-trione (TTT), and 2,2-dimethoxy-2-phenylacetophenone (DMPA) were purchased from Sigma-Aldrich. 1,6-Hexanediol ethoxylate diacrylate (HEDA) was provided by Sartomer. All the materials were used as received. Fluorinated acrylate copolymers were synthesized by free radical polymerization. See Supporting Information for more details.

Table 4.1 Composition of coating formulations

Formulation	T _f (mol%)	E _f (mol%)	A _f (mol%)	F _f (wt%)
TE	50	50	-	-
TEA5	47.5	47.5	5	-
TEA10	45	45	10	-
TEA25	37.5	37.5	25	-
TEF	50	50	-	1

[a] All formulations include 0.25 wt% of DMPA.

4.3.2 Coating Formulation Preparation.

The coatings were formulated based on a stoichiometric balance of thiol functional groups (T_f) and ene functional groups (E_f). In the preparation of thiol-ene(-acrylate) coatings, acrylate functionalities (A_f) were added to the base thiol-ene mixture, with the molar percentages of all three functional groups (T_f, E_f, and A_f) totaling 100%.¹²¹ The fluorinated additive (F_f) and DMPA were added at concentrations of 1 wt% and 0.25 wt% of the coating mixture, respectively. Compositions of all the UV-curable coating formulations employed in this study are summarized in Table 4.1 Composition of coating formulations. All the components of a formulation were added into a glass vial and stirred at room temperature for 4 h. The glass vials were wrapped in aluminum foil to avoid any pre-polymerization. In the preparation of TEF, F-PMMA was dissolved in 2 mL tetrahydrofuran (THF) and then added to the mixture of other components.

Unpatterned Coating Preparation. Unpatterned coatings were prepared by casting coating formulations on glass substrates using a wire-wound rod. Especially, the applied fluorinated formulation was allowed to dry under ambient conditions for 5 min to ensure the removal of THF. Liquid coatings were exposed to UV light (at a wavelength of 365 nm and an intensity of 100 mW/cm²) from a

LED source (Tangent Industries Inc.) at room temperature. The thickness of the obtained coating was approximately 100 μm . Cured coatings were directly used for subsequent characterizations unless otherwise noted.

4.3.3 *Synthesis of F-PMMA*

The synthesis of F-PMMA is described elsewhere.¹²² Methyl methacrylate (MMA) and 2-(perfluorooctyl) ethyl acrylate (CFA) were obtained from Sigma-Aldrich. MMA and CFA monomers were passed through alumina powder to remove inhibitors prior to use. Then 8g MMA and 2g CFA were added into a 50mL flask along with 0.1g recrystallized AIBN and 20 mL dioxane. The reaction was conducted at 70 °C for 6h under purified argon atmosphere after 20 min of degassing by argon purge. The reaction was terminated by quenching in ice water and the polymer was precipitated in cold methanol followed by methanol washing for 6 times. The polymer was dried in vacuum oven for 24h.

4.3.4 *Kinetic Analysis*

Real-time Fourier transform infrared spectroscopy (FTIR) was performed to monitor the photopolymerization kinetics of prepared coatings on a Magna IR-750 FTIR spectrometer (Nicolet Instrument Co.) in the transmission mode.^{34, 123} Samples were prepared by sandwiching a thin layer of the uncured formulation ($\sim 25\ \mu\text{m}$) between two sodium chloride plates separated by around steel spacer ($0.025 \times 25\ \text{mm}$) and then polymerized in the sample chamber. The UV light ($365\ \text{nm}$, $200\ \mu\text{W}/\text{cm}^2$) for initiating reactions was from a mercury pencil lamp

(Spectronics Corp.) placed inside the IR main chamber. The polymerization processes were monitored in real-time by the FTIR spectrometer operated at 5 scans per spectrum and a 2 cm⁻¹ resolution. Resulting conversions of functional groups were analyzed using the Thermo Scientific OMNIC software package by integrating the area under characteristic IR absorption peaks (the thiol peak at 2570 cm⁻¹, the ene peak at 3083 cm⁻¹, and the acrylate double bond peak at 810 cm⁻¹). Integrated values of the peak area were proportional to the corresponding concentrations of the functional group in the sample. The functional group conversions (x) at various curing times were calculated from the peak area after curing for time t (A_t) and that at the start of curing (A_0):

$$x = \frac{A_0 - A_t}{A_0} \times 100\% \quad (1)$$

4.3.5 Analyses of Cured Materials Properties

A. Thermal Analysis

Differential scanning calorimetry (DSC) was used to characterize thermal properties of cured coatings on a TA Q1000 calorimeter (TA instrument).

Samples (5 - 10 mg) were sealed in aluminum pans and heated from -50°C to 100°C at a heating rate of 10°C/min. The second heating scan was used to determine the glass transition temperatures.

B. Mechanical Properties

Standard tensile tests were conducted to measure the moduli of UV cured free-standing films on an RSA G2 solid analyzer (TA Instruments) according to

ASTM D638. Samples were prepared from coatings on silicone release films and cut into 2.5 cm × 1 cm × 100 μm specimens. Stress-strain behaviors were recorded at a crosshead speed of 1 mm/min under ambient conditions.

C. Surface Analysis

Contact angle measurements were performed to measure the static contact angles of cured coatings using a drop shape analyzer (Krüss). The equipment was enclosed in a transparent plastic box to reduce exposure to organic solvents. Water and diiodomethane (Sigma-Aldrich) were used as solvents with a droplet size of 2 μL. Two specimens were prepared for each coating formulation, and three drops were made on each specimen. The contact angle of a droplet was measured at room temperature using the Advance software. The surface energy of the surface of a cured coating was analyzed according to ASTM D7490 based the Owens-Wendt-Kaelble equation:

$$\frac{\gamma_l(1 + \cos \theta)}{2} = (\gamma_l^d \gamma_s^d)^{1/2} + (\gamma_l^p \gamma_s^p)^{1/2} \quad \text{Equation 4.1}$$

$$\gamma_s = \gamma_s^d + \gamma_s^p \quad \text{Equation 4.2}$$

where θ is the contact angle of the testing liquid on the tested coating surface, γ_l and γ_s are the surface tension of the testing liquid and the surface energy of the solid coating, respectively, and γ^d and γ^p are the dispersion component and the polar component, respectively. The surface tension values for water and diiodomethane are known (water: $\gamma_l = 72.8$ dyn/cm, $\gamma_l^d = 21.8$ dyn/cm, and $\gamma_l^p =$

51.0 dyn/cm; diiodomethane: $\gamma_l = 50.8$ dyn/cm, $\gamma_l^d = 49.5$ dyn/cm, and $\gamma_l^p = 1.3$ dyn/cm). X-ray photoelectron spectroscopy (XPS) measurements were performed on an SSX-100 XPS system (Surface Science Laboratories) equipped with a monochromatic Al K_α X-ray source operating at 200 W under 10^{-9} Torr. All spectra were recorded with the Esca Capture software. Binding energies were calibrated with respect to C 1s at 285 eV.

4.3.6 Mold Fabrication

A. Master mold fabrication

Silicon wafers were deep cleaned with a Piranha solution (1:1 H_2SO_4 with H_2O_2) at 120°C for 10 min and rinsed with deionized water and dried. The master mold with a feature height of 20 μm was prepared by spin-coating a silicon wafer with SU-8 2010 photoresist (MicroChem Corp.) at 500 rpm for 10 s followed by 1000 rpm for 30 s. The coated wafer was soft-baked at 95°C for 4 min and then exposed to UV light through a patterned Chrome photomask for 16 s using an MA-6 Karl Süss contact aligner. The exposed wafer was post-baked at 95°C for 5 min. The wafer was developed with the SU-8 developer for 3 min, and then rinsed with isopropanol (IPA) thoroughly, and dried. The completed wafer was baked at 150°C for 5 min.

In the preparation of 50- μm -tall features, SU-8 2050 photoresist was spin-coated on a wafer at 500 rpm for 5 s followed by 3000 rpm for 30 s. Soft baking was conducted at 65°C for 3 min and at 95°C for 7 min. The coated wafer was exposed through a Chrome photomask for 24 s. The exposed silicon wafer was

post-baked at 65°C for 1 min and at 95°C for 7 min. The wafer was immersed in the SU-8 developer for 5 min and rinsed with IPA and dried. The developed wafer was hard-baked at 150°C for 5 min.

For 100- μm -tall feature preparation, SU-8 2075 photoresist was spin-coated on a wafer at 500 rpm for 10 s followed by 2200 rpm for 30 s, followed by soft baking at 65°C for 5 min and 95°C for 20 min. The exposure time was set at 30 s. The post-baking step was 5 min at 65°C and 10 min at 95°C. The wafer was slowly cooled down under ambient conditions for 20 min and then immersed in the SU-8 developer for 20 min. After rinsing with IPA and drying, the developed wafer was hard-baked at 150°C for 5 min.

B. PDMS Mold Fabrication

The PDMS prepolymer and its curing agent (Sylgard-184, Dow Corning) were mixed at a 10:1 weight ratio and then vacuum degassed for approximately 20 min until the mixture was clear. The mixture was poured onto the SU-8 master mold and degassed for another 20 min to remove any entrapped air bubbles. See Supporting Information for the photolithography fabrication processes of SU-8 master molds. The PDMS layer was cured in an atmospheric oven at 90°C for 2 h. After cooling down to room temperature, the cured PDMS was peeled off from the SU-8 master to obtain the PDMS mold.

The light transmittance property of the PDMS mold (with a thickness of 1.7 mm) was characterized with a UV-visible spectrometer (Thermo Scientific, Evolution 220). Figure 4.2 shows that the PDMS mold has a high transmittance

(> 90%) from 300 nm to 800 nm. In the wavelength range corresponding to the emission spectrum of the UV LED light source, 365 ± 5 nm, the average transmittance is higher than 95%, suggesting the mold does not significantly affect the photopolymerization of coatings during micromolding experiments.

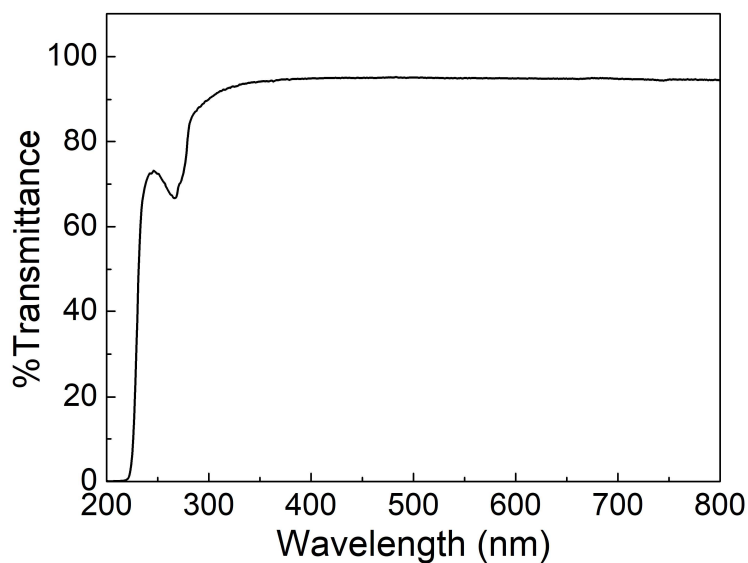


Figure 4.2 UV-visible spectrum of the PDMS mold.

PDMS thickness was 1.7 mm.

4.3.7 Micromolding Experiments

The prepared coating formulation was applied to a 100- μ m-thick PET substrate (3M) using a wire-wound bar with a wet film thickness of approximately 100 μ m. Before the coating application, the substrates were roughened with silicone carbide powders, rinsed with acetone and water, and blow-dried with air. The PDMS mold was placed on the liquid coating from one end of the mold to the other with the patterned side facing down. The wetting front of the liquid coating moved along the grating direction to avoid air entrapment between the liquid coating and the mold. The coating was cured through the PDMS mold by UV

LED light (365 nm and 100 mW/cm²). After UV curing, the mold was peeled off by hand to obtain the microstructured coating.

4.3.8 Patterned Coating Imaging

A Hitachi S4700 scanning electron microscopy (SEM) was used for obtaining images of the fabricated microstructures in an oblique view and a cross-sectional view. The coating cross-sections were cryo-microtomed at -120°C using a Leica UC6 microtome instrument equipped with a diamond knife. Samples were sputter-coated with a thin layer (5 nm) of Iridium before imaging.

4.3.9 Peel Strength Measurement.

The peel strength was measured with 90° peel tests on an RSA G2 solid analyzer, which operated in the spring mode using an upper tension fixture and a 3D-printed test stage. The assemblies of a cured coating and a PDMS mold were subjected to peel testing without any post-cure treatment. The coating on a PET substrate was attached to a piece of aluminum foil, which connected to the force sensor. The PDMS mold was mounted on a glass slide that provided rigid support and fixed on the test stage. See Figure 4.3. During a test, a cured coating on the substrate was peeled off from the mold on the solid analyzer during which the peel force was recorded as a function of the displacement of the crosshead. A photo of the peeling apparatus midway through the demolding step. In our experimental set-up, the peeling rate equals the crosshead speed, 30 mm/min, and

the peeling angle is approximately 90°. The peel force (F) was normalized with respect to the sample width (w), yielding the peel strength (P):

$$P = F/w$$

Equation 4.3

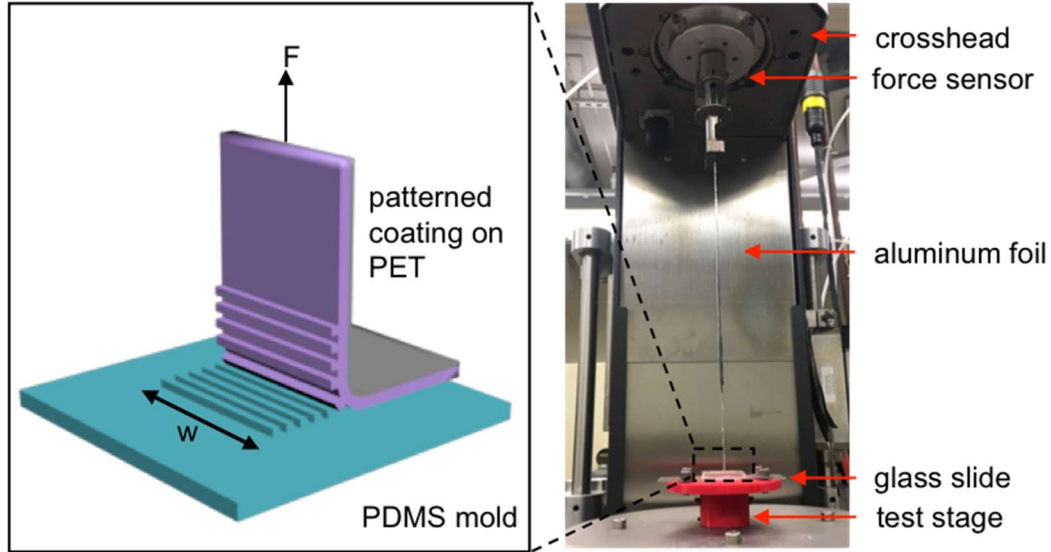


Figure 4.3 Schematic representation and picture of the apparatus for the peel strength measurement.

Samples were peeled off at 90° and 30 mm/min.

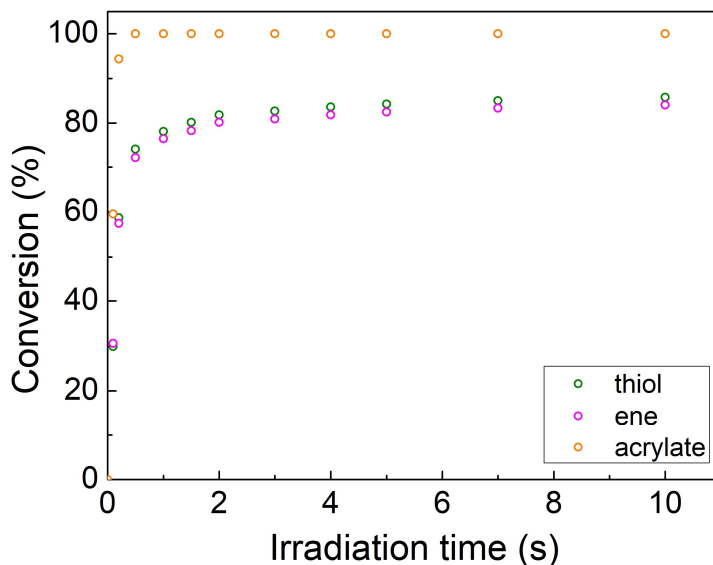
In the present work, the value of the peeling strength was calculated using the area method¹²⁴. For each measured curve of peeling strength versus displacement, the area under the plateau region was integrated (the work done by the external peel force per unit width) and then divided by the corresponding displacement. The middle part of the plateau region ($D = 5$ mm) was used for the calculation to remove any influences of the instabilities at the edge of the patterned area. The long and flexible aluminum foil could reduce the systematic error in peeling angles by increasing the distance between the force sensor and the

sample ($d = 120$ mm). The theoretical change of the peeling angle during a test was $\pm 1.2^\circ [\tan^{-1}(\frac{D}{2} \div d)]$.

4.4 Results and Discussion

4.4.1 Photopolymerization Kinetics

The curing kinetics of the TEA10 coating were investigated with the FTIR under UV exposure at an intensity of 100 mW/cm^2 . The characteristic peaks of all functional groups in the coating were followed as a function of time, including the thiol peak at 2570 cm^{-1} , the ene peak at 3083 cm^{-1} , and the acrylate peak at 810 cm^{-1} .



(4.4 Functional group conversion vs. time for a TEA10 coating. The sample contains 0.25 wt.% DMPA and was exposed to UV light at 100 mW/cm^2 .

As shown in (4.4, the acrylate conversion reaches 100% immediately after UV exposure, indicating that acrylate double bonds mainly react through

homopolymerization at the initial stage of curing. Thiol and ene groups polymerize rapidly initially and then both reach plateau conversions. The thiol groups have a slightly higher limiting conversion compared with that of ene groups, which could be due to the fact that a small portion of thiol radicals undergo the chain transfer reaction with acrylate double bonds.¹²¹ Furthermore, the real-time FTIR results show that, for all the thiol-ene(-acrylate) formulations, the acrylate oligomers attained full conversions immediately upon UV exposure, while the conversions of thiol and ene functional groups increased rapidly initially and then both reached a limiting conversion value (shown in (4.4)). Bowman *et al.* observed similar results in thiol-allyl ether-acrylate ternary systems and attributed it to the reactivity difference of between acrylates and allyl ethers.¹²¹ Because the electron density of the acrylate double bond is higher than that of the ene double bond, the chain polymerization of acrylates dominates the initial stage of the curing process, generating acrylate oligomers. Following this stage, thiol and ene functional groups react to form crosslinked networks. The limiting curing extent of thiol groups is slightly higher than that of ene groups because a proportion of thiols undergo chain transfer reaction with the acrylate double bonds.

We investigated the effects of acrylate addition on the curing kinetics of coatings, represented by the conversion of thiol functional groups. It should be noted that real-time FTIR measurements were conducted with a low-intensity UV lamp, but the observed trend in the curing kinetics should be similar to that with a higher intensity LED lamp.

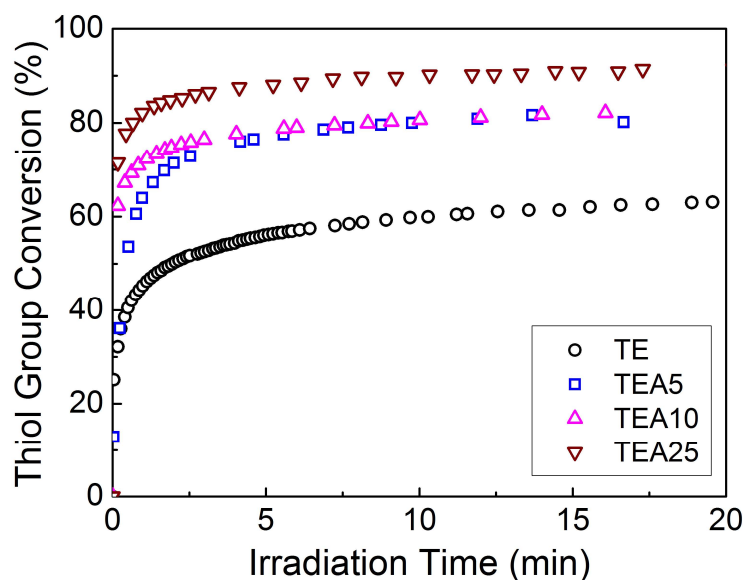


Figure 4.5 Thiol group conversion as a function of the irradiation time in thiol-ene(-acrylate) photopolymerizations monitored by real-time FTIR.

The curing kinetics of TEF was identical to that of TE and thus not shown in the plot. Samples contained 0.25 wt% DMPA and were exposed to a 365 nm mercury lamp at $200 \mu\text{W}/\text{cm}^2$.

As shown in Figure 4.5, all the formulations exhibited high photopolymerization rates even at a low light intensity ($200 \mu\text{W}/\text{cm}^2$) and achieved limiting conversions at around 10 minutes of exposure. According to the light intensity and the exposure time, the curing dosage of the thiol-ene(-acrylate) coating system is approximately $120 \text{ mJ}/\text{cm}^2$, which is among the lowest dosage values for UV coatings used in micromolding applications. The curing dosage of a urethane acrylate coating⁶² is reported to be $300 \text{ mJ}/\text{cm}^2$ and the lowest reported value is $80 \text{ mJ}/\text{cm}^2$ for an epoxy silicone coating¹¹². Therefore, the thiol-ene(-acrylate) coating system shows great promise for use in high-throughput micromolding applications.

The limiting conversion, however, increased with the acrylate concentration. In the case of TE, the relatively low limiting conversion (~60%) results from the fact that highly crosslinked networks restrict the mobility of the reactive species and thus further reactions of functional groups, which is in good agreement with the previous results¹²³. High limiting conversions (80 – 90%) were attained in coatings containing acrylate oligomers, due to an enhanced mobility afforded by the flexible ether linkage along with a lower functionality of acrylate oligomers.

4.4.2 *Tunability of Thermomechanical Properties*

It has been well documented that thermomechanical properties of thiol-ene(-acrylate) coatings depend on the chemical structures of monomers, the crosslinking density, and the curing extent. For instance, flexible ether groups lead to low glass transition temperatures and low moduli, and ring structures result in stiff materials with glass transitions at higher temperatures.¹²⁵ Moreover, the moduli of cured coatings increase with the crosslinking densities of polymer networks, which can be achieved by decreasing the length of spacer between functional groups, increasing the monomer functionality, or increasing the concentration of crosslinkers.^{114, 126} Additionally, the curing extent of functional groups also has an effect on mechanical properties due to the plasticization effect of unreacted dangling chains.

Based on our current knowledge of the thermomechanical properties of thiol-ene(-acrylate) coatings, we selected a tetrafunctional thiol monomer (PTMP)

and a trifunctional ene monomer (TTT), which photopolymerize into materials presenting a high T_g and a high modulus, along with a diacrylate oligomer (HEDA) with a long and flexible spacer between functional groups. In the curing of samples, a LED light source was used considering that its high intensity (100 mW/cm^2) could increase the curing speed and that the narrow wavelength distribution ($365 \pm 5 \text{ nm}$) could reduce the heat generation during curing.¹²⁷ Samples were exposed to a sufficient dosage of UV light (10 seconds) to ensure limiting conversions were attained and cured samples were not subject to any thermal annealing process after UV curing.

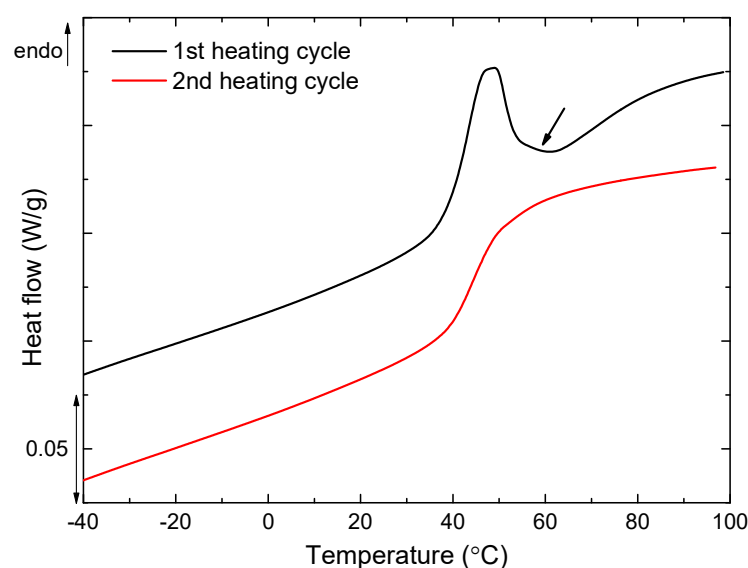


Figure 4.6 DSC curves of the first and second heating cycles of TE.

Experiments were performed at a heating rate of 10°C/min .

The effects of the acrylate addition on the thermal properties of thiol-ene(-acrylate) coatings were investigated using DSC. For TE, an exothermic peak was observed during the first heating cycle and disappeared in the second (See **Figure 4.6**), which could be due to the continued polymerization of residual monomers at

elevated temperatures, further confirming the limited conversion value of TE from the FTIR experiment. In cases of coatings containing acrylates, the first and the second heating cycles overlapped since almost complete conversions were reached in these coatings. The second heating cycles were used for the comparison of the glass transition behaviors of the coating system.

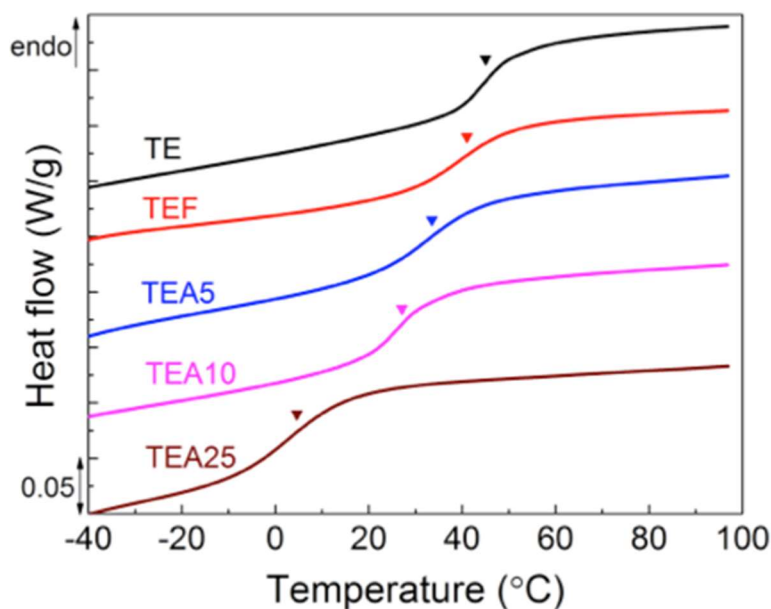


Figure 4.7 DSC curves of thiol-ene(-acrylate) networks at a 10°C/min heating rate.

Results from the second heating cycle were presented.

Shown in Figure 4.7, the DSC curves of all the coatings exhibited a distinct and narrow glass transition region ($\sim 15^\circ\text{C}$ in width), indicating that the polymer networks were homogenous upon acrylate addition. The obtained T_g of the thiol-ene coating (45°C) was in agreement with the literature value (45°C)¹²⁵. Furthermore, the glass transition temperatures decreased with increasing acrylate concentrations as summarized in Table 4.2. The observed trend in T_g could be attributed to a combined effect of the chemical structures and the network

crosslink densities. It is inferred that acrylate oligomers introduce flexible ether linkage into polymer networks and thus enhance the segmental mobility; at the same time, the lower functionality of acrylates reduces the crosslinking density, resulting in a less restricted segment movement.

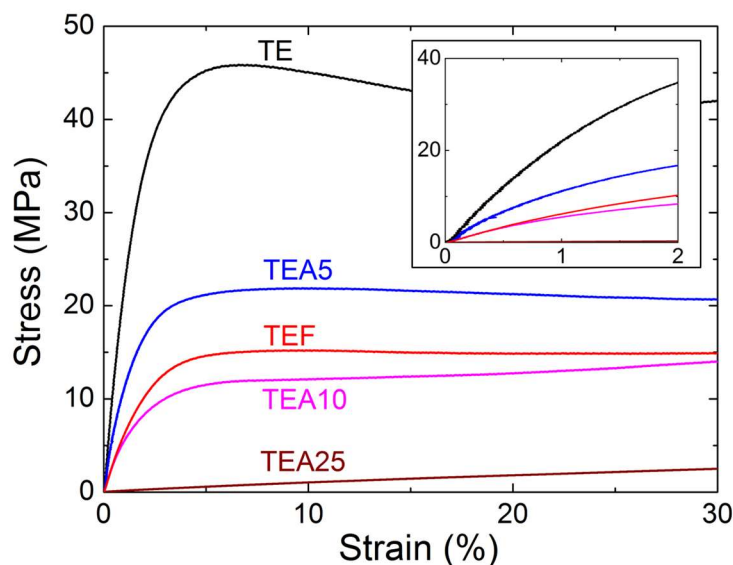


Figure 4.8 Stress-strain curves of UV-cured thiol-ene(-acrylate) coatings under ambient conditions.

The inset shows the region of elastic deformation used for the modulus calculation. The crosshead speed was 1mm/min.

The mechanical properties of cured thiol-ene(-acrylate) films were investigated by tensile testing under ambient temperature, providing information on coating performances under typical processing conditions and application environments. In the cases of TE, TEA5, and TEA10, the stress increased linearly with the strain and then exhibited a maximum followed by a broad interval of nearly constant stress values (Figure 4.8). On the contrary, the stress of TEA25 developed linearly with the strain up to relatively large strain values. The difference in stress-strain behaviors could be explained by previous DSC T_g

results: samples based on TE, TEA5, and TEA10 exhibited yielding as ductile materials because the testing temperature was slightly lower than their T_g values, while TEA25 showed typical characteristics of elastic materials when tested above its T_g .

The elastic moduli of cured films, as calculated from the slope of the stress-strain curve at small strains (0 - 2%), decreased by two orders of magnitude with increasing the acrylate concentration. Consistent with previous results^{113, 125}, TE-based samples showed a high modulus of 1.74 GPa, which is comparable to those of common thermoplastics¹²⁸ (PMMA and PS) and epoxy resins³³. With the addition of acrylate oligomers, the significantly decreased modulus was due to the flexibility of acrylate oligomers and a lower crosslink density.

Table 4.2 Thermomechanical properties of UV-cured thiol-ene(-acrylate) films

Formulation	T_g (°C)	E (MPa)
TE	45	1740 ± 153
TEA5	34	994 ± 190
TEA10	27	440 ± 101
TEA25	5	13 ± 2
TEF	41	522 ± 38

[a] The standard deviations of tensile moduli were based on testing results of five samples for each formulation.

4.4.3 Surface Energy Reduction

The surface energy of thiol-ene coatings was modified using a fluorinated acrylic copolymer (F-PMMA), synthesized from methyl methacrylate and 1H, 1H, 2H, 2H-perfluorodecyl acrylate by free radical polymerization (details in the Supporting Information).¹²² The chemical structure of F-PMMA is composed of a

long fluorinated side chain to reduce the surface energy and an acrylate backbone to ensure good miscibility with the thiol-ene mixture. Specifically, THF was added with the F-PMMA to accelerate the dissolution of polymers in the thiol-ene mixture and to facilitate the migration of F-PMMA by lowering the viscosity of the formulation. The excess solvent was allowed to evaporate for 5 min after coating application and thus had negligible influence on the curing process.

SEC was employed to determine the molecular weight and dispersity of the fluorinated copolymer with THF as the mobile phase. Universal calibration was performed with the Mark-Houwink parameters of Poly(methyl methacrylate) $K = 8.97$, $\alpha = 0.71$ ¹²⁹. The SEC trace of synthesized F-PMMA is provided in Figure 4.9.

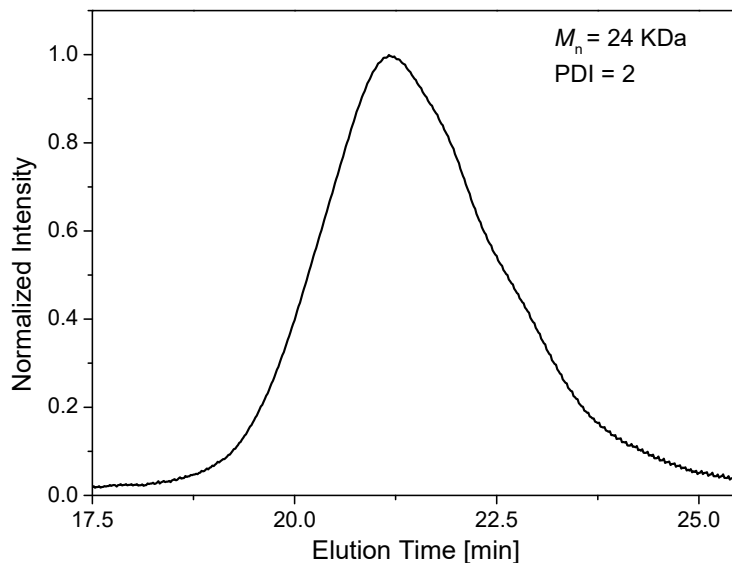


Figure 4.9 SEC trace of F-PMMA.

The incorporation of the fluorinated monomer in the copolymer was confirmed with ^1H NMR. Approximately 0.1g of copolymers were dissolved in

CDCl₃ with internal reference TMS and then NMR experiments were done using Bruker HD-500. The NMR trace is provided in Figure 4.10 with characteristic peaks assigned.

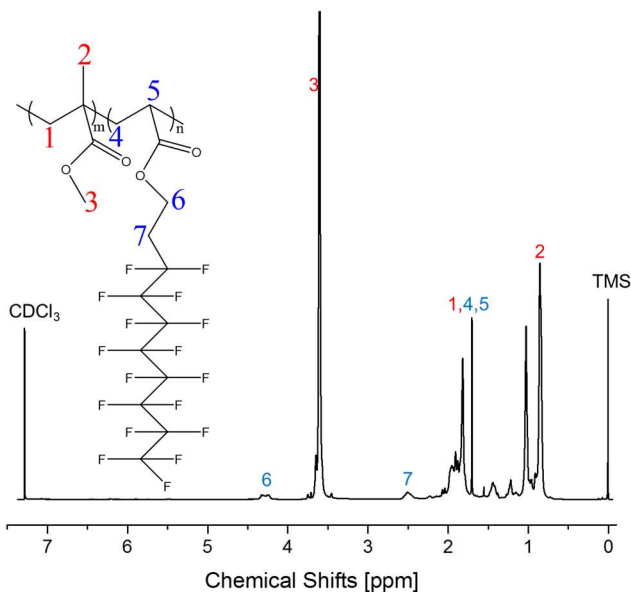


Figure 4.10 ¹H NMR trace of F-PMMA

The static contact angles of the thiol-ene coating (TE) and the fluorinated coating (TEF) were examined using water and diiodomethane (oil with a low polarity). Both the water contact angle (θ_w) and the diiodomethane contact angle (θ_i) significantly increased upon only 1 wt% addition of F-PMMA (Figure 4.11). Further increasing the F-PMMA loading resulted in marginal changes of contact angles, indicating that the surface coverage of fluorinated side groups saturates at a very low concentration. According to the surface elemental analysis by XPS (Figure 4.12), TEF exhibited strong signals related to the binding energy of F 1s at 688.6 eV¹³⁰, which did not exist in the spectrum of TE coatings. The results support the mechanism of surface energy reduction proposed in previous

studies^{131, 132}: fluorinated side groups tend to assemble at the air and liquid interface to reduce the surface tension of the coating system, forming a fluorocarbon-rich layer at the surface. The surface segregation of fluorinated groups is enthalpy driven due to the difference in surface tension between monomers and the fluorinated polymers.¹³³

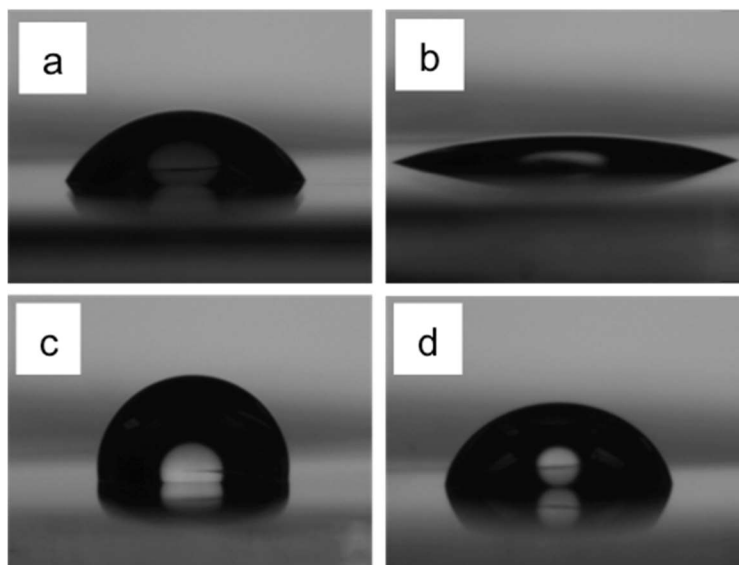


Figure 4.11 Contact angle measurement of TE and TEF coatings.

Cured TE surfaces with (a) a water droplet and (b) a diiodomethane droplet compared with cured TEF surfaces with (c) a water droplet and (b) a diiodomethane droplet.

The surface free energies (γ) of coatings were determined on the Owens-Wendt-Kaelble method (the calculation is described in the experimental section). According to **Table 4.3**, the surface energy of a TE coating is similar to that of PET films (49.8 mJ/m^2)¹³⁴, a relatively high value among polymeric surfaces. With fluorinated additives, TEF exhibits a remarkable low surface energy comparable to that of PDMS ($\sim 19.6 \text{ mJ/m}^2$)¹³⁵. Compared to a previous study¹³⁶ on the surface modification of thiol-ene coatings using a fluorinated monomer (at

~20 wt%), our approach based on the polymeric fluorinated additive is more environmentally friendly and works at much lower loadings.

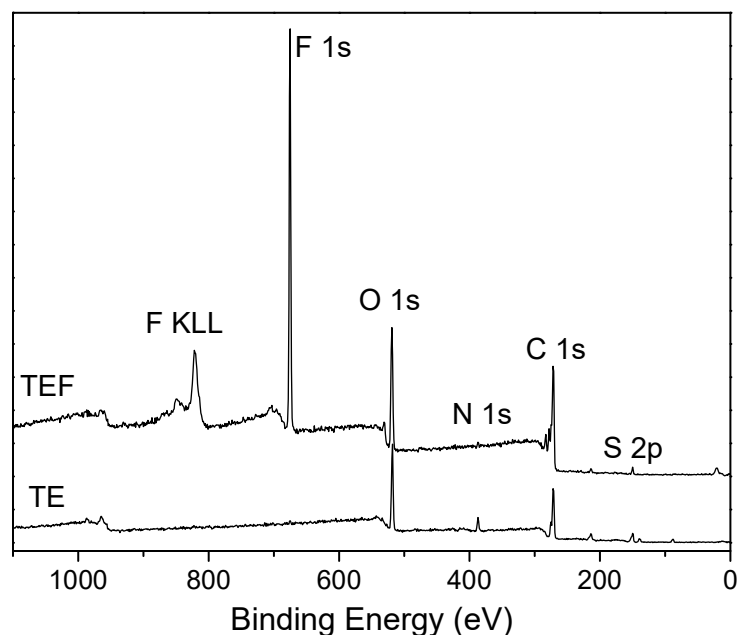


Figure 4.12 XPS survey spectra for cured TE and TEF coating surfaces.

Table 4.3 Surface properties of cured TE and TEF coatings.

Formulation	$\theta_w (^{\circ})$	$\theta_i (^{\circ})$	$\gamma \text{ (mJ/m}^2\text{)}$
TE	63.4 ± 2.3	19.5 ± 1.3	52.2
TEF	98.6 ± 0.8	76.5 ± 2.8	20.2

[a] Standard deviations of contact angles were calculated from 12 measurements.

Thermomechanical properties of films prepared from TEF were evaluated with DSC and tensile testing. Comparing the DSC curves of TE and TEF in Figure 4.7, the T_g value slightly decreased upon the addition of F-PMMA, which could be explained by the plasticization effect that the chain ends of F-PMMA enhance the mobility of the segments on polymer networks. Moreover, tensile testing results show that the fluorinated additives resulted in a lower elastic

modulus of the cured coating. Since F-PMMA is not expected to appreciably affect the crosslinking density of thiol-ene networks at such a low loading, it is inferred that the observed decrease of modulus comes from a higher level of heterogeneity due to the segregation of fluorinated polymers.

4.4.4 Thermal stability of thiol-ene(-acrylate) coatings

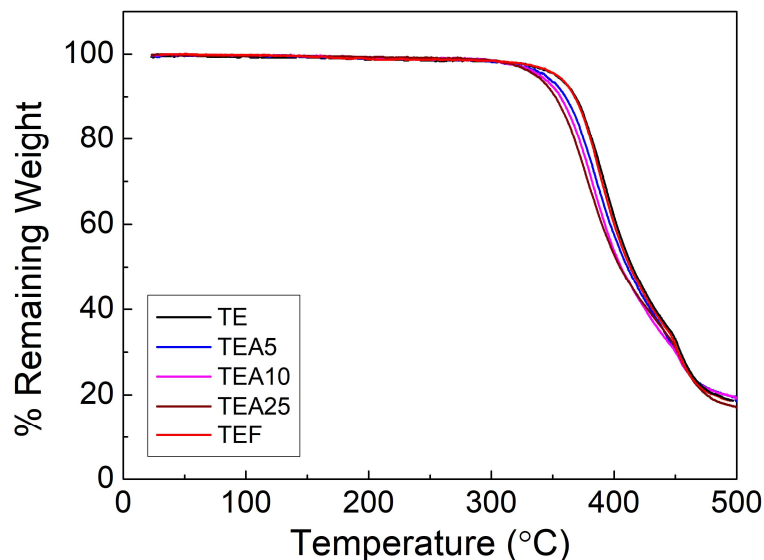


Figure 4.13 TGA thermograms of thiol-ene(-acrylate) cured coatings.

The thermal stability of thiol-ene(-acrylate) coatings was investigated with thermogravimetric analysis. All the thiol-ene based coatings are thermally stable up to ca. 350 °C. The TE network has a degradation temperature of 368°C, as determined by the temperature of 10% weight loss. The addition of acrylates leads to a slight decrease of the degradation temperature, which can be attributed to a decreased crosslink density and the chemical structure of acrylates. The degradation temperatures of TEF and TE are the same, suggesting that the

fluorinated polymer has negligible effects on the thermal stability of cured materials.

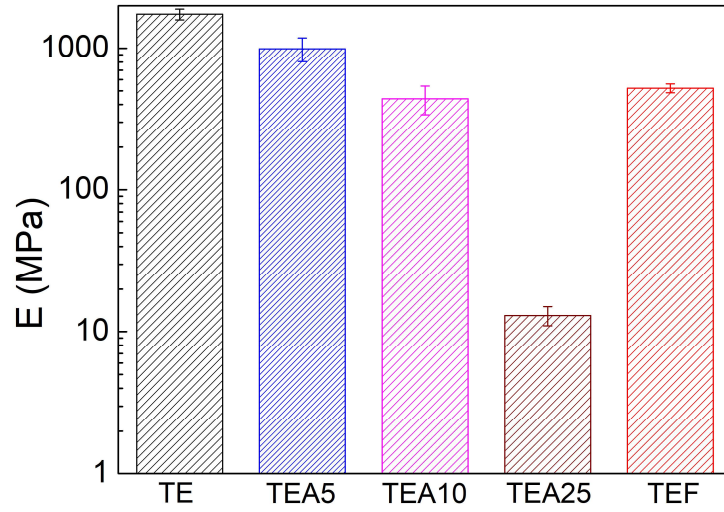


Figure 4.14 Modulus tunability of thiol-ene(acrylate) coating system.

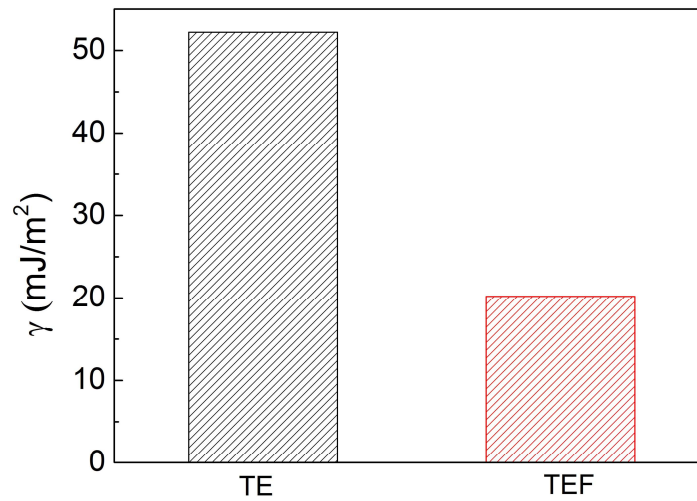


Figure 4.15 Surface energy tunability of the thiol-ene(acrylate) coating.

Before discussing the coating performances in the micromolding process, we summarize the materials properties of the prepared thiol-ene coating system

including the modulus and the surface energy (Figure 4.14 and Figure 4.15). The elastic moduli vary across two orders of magnitude with the change of the acrylate content. With 1 wt% of fluorinated copolymers, the surface energy of cured coating is reduced by more than a half. The ability to tune the modulus and the surface energy independently is critical to a better understanding of the roles of material properties in the micromolding process

4.4.5 Pattern Fidelity

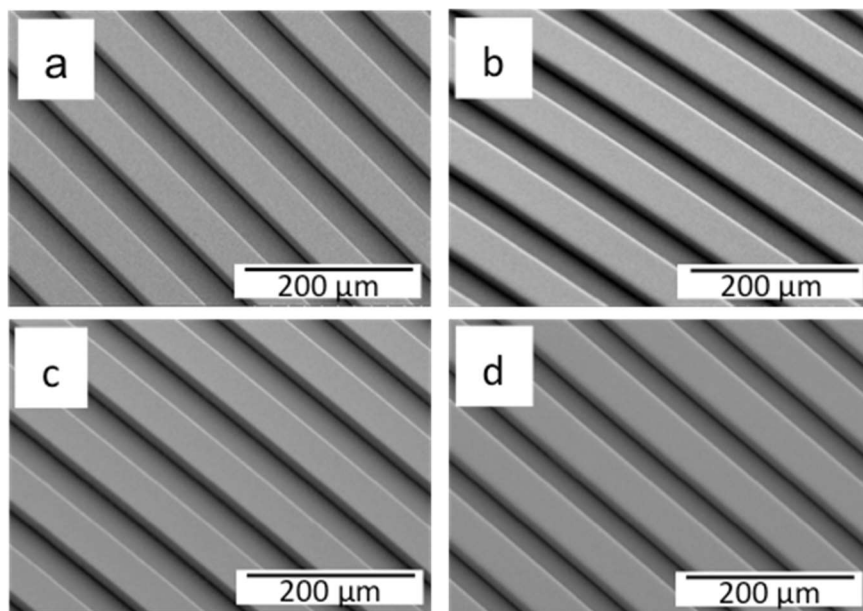


Figure 4.16 SEM images of the surface microstructures of thiol-ene(-acrylate) coatings with different moduli.

(a) TE coating with a modulus of 1.74 GPa, (b) TEA5 coating with a modulus of 994 MPa, (c) TEA10 coating with a modulus of 440 MPa, and (d) TEA25 coating with a modulus of 13 MPa. All pattern dimensions were 50 μm width by 50 μm spacing by 50 μm height. Images were taken at 45°.

To examine the pattern replication capability of the prepared thiol-ene(-acrylate) formulations, we tested microscale grating patterns with a high pattern-

density (a line width of 50 μm and a spacing of 50 μm). Typical replica molding procedures were performed under ambient conditions using a PDMS stamp, which was fabricated from an SU-8 master. For master fabrication, microstructures made of SU-8 photoresists on a silicon wafer were directly used and the feature height was determined by the coating thickness of SU-8. As opposed to the commonly used silicon masters (microstructures are fabricated by the etching of wafer and the subsequent removal of photoresists), SU-8 masters possess smoother sidewall profiles. It should be noted that the master and the mold were not subject to any surface treatment, e.g. silanization. The PET substrates were roughened to enhance the adhesion between coating and substrate.

Coating formulations with various acrylate concentrations were used to prepare gratings of 20- μm -height. The patterns were successfully replicated from the PDMS mold in all the formulations after 10 sec of UV exposure at 100 mW/cm^2 . The fast replication of patterns could be attributed to the efficiency of the photoinitiator (DMPA), the high reactivity of the monomers, and the high light intensity of the LED source. Moreover, the replicated surface microstructures showed straight lines, sharp corners, and smooth sidewalls; no significant difference was observed among the patterns in spite of the vastly different moduli of cured coatings (Figure 4.16). Therefore, combining the LED curing technique and a UV curable thiol-ene(-acrylate) coating system, we achieved the fabrication of microscale patterns within seconds at high accuracy and expanded the achievable material properties in UV micromolding processes.

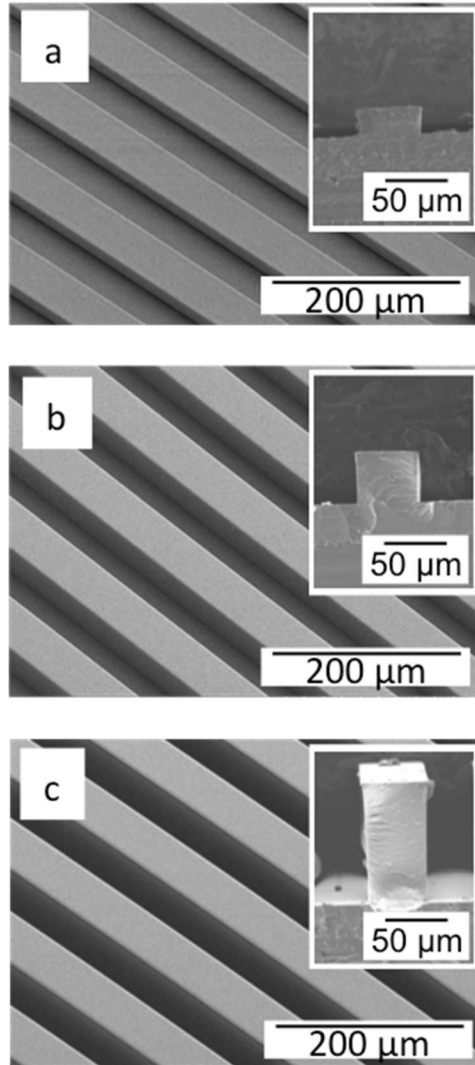


Figure 4.17 SEM images of microstructured TEF coatings with various grating heights: (a) 20 μm , (b) 50 μm , and (c) 100 μm .

All the gratings were 50 μm wide and 50 μm spaced. Inset images are the cross sections of the microstructures.

The performance of TEF in the UV micromolding process was evaluated, with the goal of eliminating demolding-related defects by lowering the surface energy of the coating. With 10 seconds of UV illumination, cured TEF coatings could be easily peeled off from the mold. Gratings of the same pattern density but

higher aspect ratios (with 50 μm and 100 μm heights) were successfully replicated using TEF. The resulting microstructures showed well-defined shapes as presented in typical SEM images (Figure 4.17).

Table 4.4 Modulus and surface energy values of elastomeric mold materials used in UV micromolding processes

Material	Modulus (MPa)	Surface energy (mN/m ²)
TEF	522	20.2
PDMS (Sylgard 184) ¹³⁷	2.0	19.6
Polyurethane acrylate (PUA) ¹¹¹	20 - 320	20 - 60
Ethylene tetrafluoroethylene (ETFE) ^{78, 138}	1200	15.6
Perfluoropolyether (PFPE) ^{135, 139}	155	23.6

In addition to the direct application as UV curable resins, the TEF-based formulation represents an exciting alternative to the traditional mold material PDMS. It is known that the attainable pattern resolution of a mold material is determined by the modulus and the surface energy; typically, a high modulus helps maintain the integrity of surface features while a low surface energy is required for clean mold release. Table 4.4 compares the modulus and the surface energy values of TEF to those of mold materials currently used in UV micromolding processes. Accordingly, TEF outperforms PDMS by a much higher modulus, and it is comparable to other newly developed mold materials in consideration of the theoretically achievable resolution.

4.4.6 Demolding Analysis

In the replication of 100 μm tall gratings, the demolding failure occurred in all the formulations except for TEF: TEF patterned coatings were peeled off

from the PDMS mold without any contamination of the mold; on the contrary, coatings without the fluorine addition were completely removed from the PET substrate, adhering to the mold surface. In the thiol-ene(-acrylate) coating system, the modulus and the surface energy of cured coatings can be adjusted independently, allowing for an investigation of their roles during demolding. In the subsequent discussion, we quantitatively compared the demolding performances of different coating formulations using peel tests. Because the peel strength is known to correlate with the peeling angle and the peeling rate¹⁴⁰, we ensured the reproducibility of tests by controlling the peeling rate at 30 mm/min and the peeling angle at 90° (with an approximated variance of $\pm 1.2^\circ$ in each measurement).

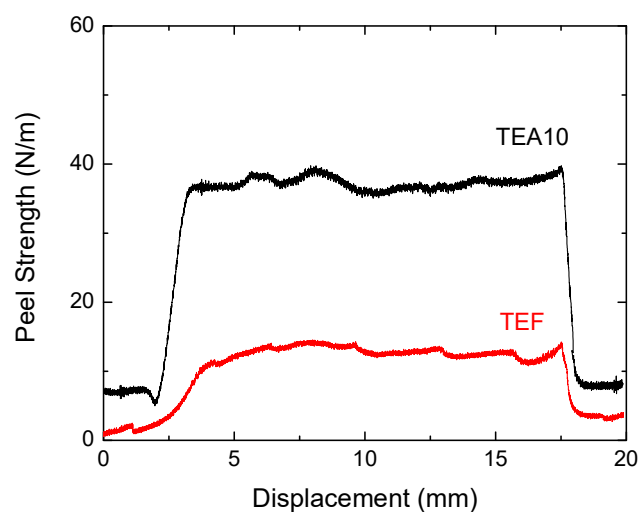


Figure 4.18 Representative peel strength versus displacement of the peel front of patterned TEA10 and TEF, which have different surface energies but similar moduli. Grating height: 50 μm .

The effects of surface energy on the peel strength were investigated using formulations of TEF ($\gamma = 20.2 \text{ mJ/m}^2$, $E = 522 \text{ MPa}$) and TEA10 ($\gamma = 50.1 \text{ mJ/m}^2$, $E = 440 \text{ MPa}$) with the peeling direction perpendicular to the gratings. Typical curves for the peel strength as a function of the displacement of the peel front is shown in Figure 4.18. For both coatings, the peel strength rises sharply when the peel front reaches the patterned area and remains at the plateau value across the patterned region.

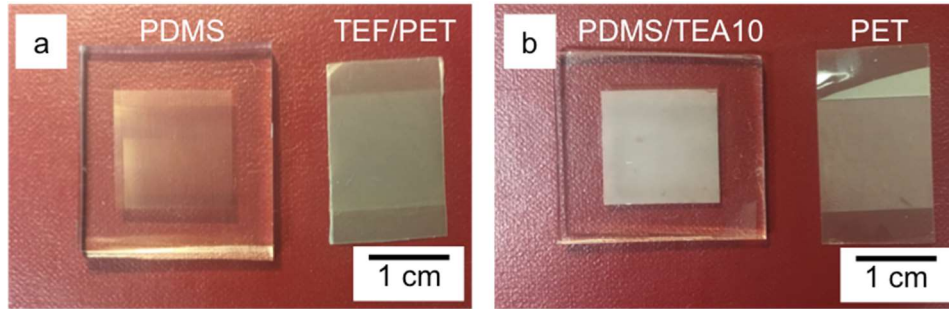


Figure 4.19 (a) Clean release of the TEF coating and (b) demolding failure of the TEA10 coating.

Especially, in the case of TEA10 coating with a $100 \mu\text{m}$ grating height, the strength needed to separate the coating from the mold exceeds the adhesion strength between coating and substrate. As a result, fracture occurs at the coating/substrate interface, which explains the demolding failure observed during the previous micromolding experiments. Figure 4.19 shows representative images of microstructured coatings after demolding. Figure 4.19a shows the PDMS mold with a delaminated TEA10 coating (the opaque region is the backside of the patterned coating due to the roughness of the original coating/PET interface). Figure 4.19b shows the PET substrate used to hold the coating. The

PDMS molds in both pictures were patterned with gratings that were 50 μm wide, 50 μm spaced, and 100 μm high.

The demolding behavior of TEF (1% F_f) and TEA10 (no F_f) were compared at different grating heights and summarized in **Figure 4.20**. The peel strength is lower with the fluorine addition because of the reduced surface energy of a coating. Moreover, patterns with higher aspect ratios result in increased peel strength, which could be attributed to a larger interfacial area between the microstructured coating and the mold.

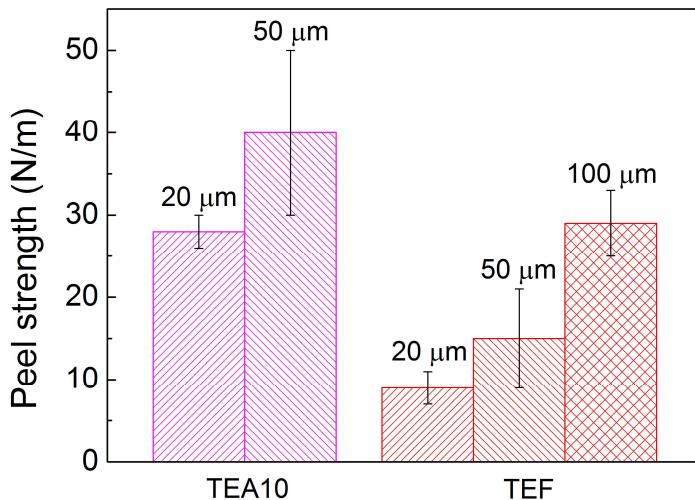


Figure 4.20 Averaged peel strength of TEA10 and TEF at grating heights of 20 μm , 50 μm , and 100 μm .

No peel strength is reported for TEA10 with 100 μm features because demolding failed. Error bars were based on repeated tests of 5 samples.

We further studied the effects of elastic modulus on the peeling strength of microstructured coatings. With an increase of the acrylate content, the elastic modulus of the cured coating decreases without a significant change in the surface energy. Figure 4.21 shows that peeling strengths decrease with increasing the

acrylate content in coating formulations. In Figure 4.22, similar trends were observed in coatings with 20 μm and 50 μm gratings (data for 100- μm -high gratings were not available because demolding failures occurred in coatings without any fluorine addition). Therefore, in addition to the surface energy, decreasing modulus of a coating also significantly reduces the demolding work (peel strength).

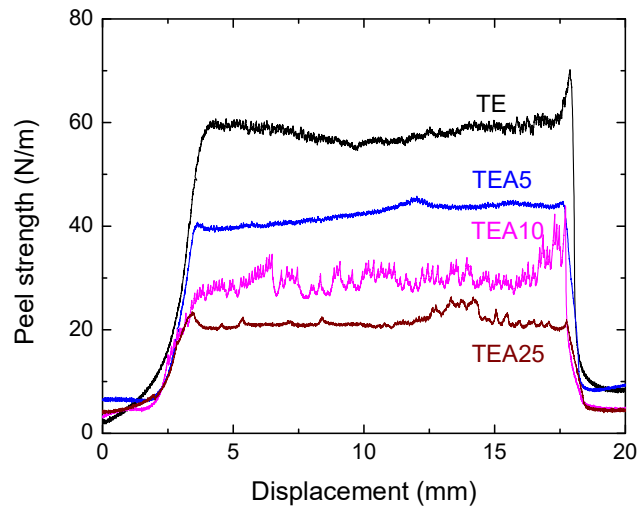


Figure 4.21 Representative peel strength *versus* displacement for TEAx coatings with various moduli but similar surface energies.

Grating height: 20 μm . Error bars were based on repeated tests of 5 samples.

We propose the following explanation: the work done by the external peel force is mainly consumed by the work of adhesion and the elastic energy stored in the system during demolding. Gratings on the coating surface need to deform elastically to be released from the mold. As the coating get softer, less energy is consumed during the elastic deformation of surface features, and thus the apparent work done by the external force is smaller.

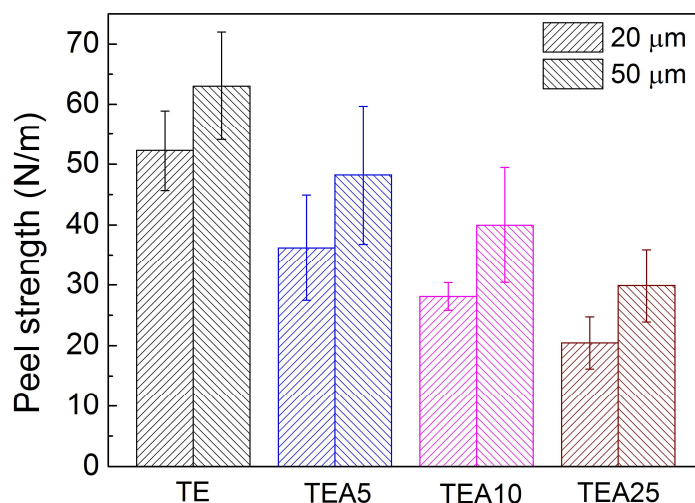


Figure 4.22 Averaged peel strength plotted against TEAx coatings at grating heights of 20 μm and 50 μm .

All the patterns investigated are 50 μm wide and 50 μm spaced and the peel direction was perpendicular to the gratings. Error bars were based on repeated tests of 5 samples.

4.4.7 *One illustration of the promise of this approach: fabricating superhydrophobic microstructured TEF coatings*

Superhydrophobic surfaces have attracted growing interests due to their great potential in applications such as self-cleaning surfaces and catalyst supports.

A low-surface energy TEF coating was patterned with 10 μm wide and 10 μm spaced micro-gratings using the micromolding process demonstrated in Figure 4.23.

The fabricated microstructured TEF coating shows superhydrophobic wetting, as evidenced by a blue-dyed water droplet sitting on the surface; the surface contact angle of the patterned coating reaches 153° (Figure 11b). The superhydrophobicity can be attributed to the inherent low surface energy of TEF and to the densely packed microscale surface topography. Moreover, the

patterned TEF surface is mechanically robust with an elastic modulus of 500 MPa and thermally stable up to ca. 370°C. The combination of the UV LED micromolding and the modified thiol-ene chemistry provides a powerful approach with high throughput potential for the fabrication of superhydrophobic surfaces.

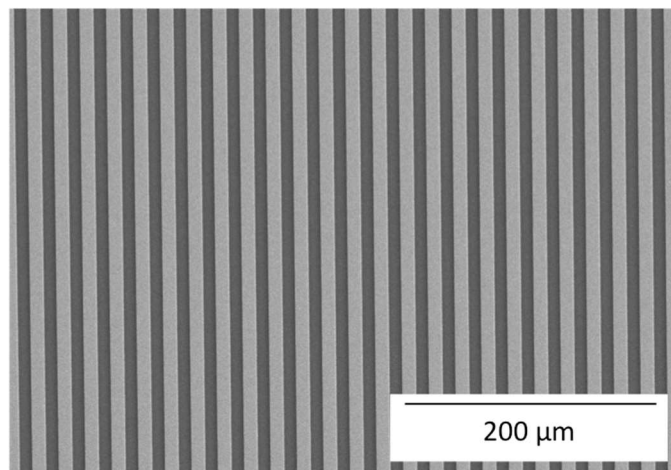


Figure 4.23 SEM image of the surface patterns of TEF.

Gratings width is 10 μm, grating spacing is 10 μm, and grating height is 20 μm.

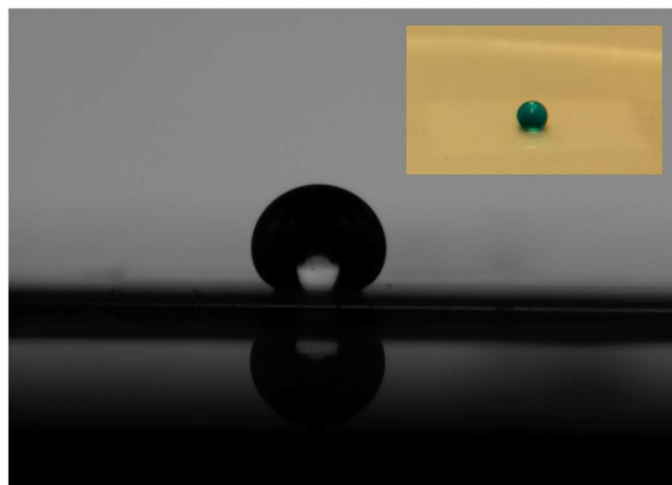


Figure 4.24 Static water contact angle for TEF coatings patterned with micro grating arrays. Inset: photograph of a blue-dyed water droplet on the surface of a patterned TEF coating.

4.5 Summary

In summary, we developed a UV curable coating system based on the thiol-ene chemistry to achieve high-throughput micromolding processes compatible with R2R manufacturing. Starting from commercially available monomers, thiol-ene(-acrylate) coatings cured into materials with drastically different mechanical properties, with Young's moduli tunable over two orders of magnitude through the variation of the acrylate concentration. A fluorinated acrylic polymer was designed for the surface modification of thiol-ene coatings, which has not been realized in previous studies of thiol-ene systems. The thiol-ene coating attained excellent hydrophobicity and oleophobicity at only 1 wt% loading of fluorinated additives, achieving a surface energy value as low as that of PDMS. With 10 seconds of UV exposure, densely spaced microstructures were accurately replicated in various thiol-ene(-acrylate) coatings of vastly different elastic moduli. Using the fluorinated coating formulation, we replicated surface microstructures of high aspect ratios without any defect formation, which was typically observed during the demolding of tall features. At controlled peeling angle and rate, the demolding strengths of micro-gratings were measured with 90° peel tests. It was suggested that failures to release the structured coating from the mold would occur when the demolding strength between the coating and the mold exceeded adhesion strength between coating and substrate. Coatings with high moduli or/and surface energies and tall features resulted in increased demolding strengths and thus demolding defects.

5 Roll-to-Roll Micromolding of UV Curable Coatings

5.1 Background and Motivation

Polymer films or coatings with surface nano-/microstructures are attracting growing research interests and finding a wide range of applications within optical films¹⁴¹, electronic devices^{61, 80}, and microfluidics. Imprinting (also known as embossing or micromolding) is one of the most promising techniques for the mass production of structured polymer materials, offering both high resolution and low cost.¹¹ Depending on the nature of polymer materials, imprinting processing falls into two main categories of thermal and UV imprinting. Thermal imprinting involves heating up a thermoplastic above its glass transition temperature, imprinting with a patterned stamp (or mold), and subsequent cooling to lock surface patterns. In UV imprinting, a UV curable liquid material is pressed with a mold and then solidified with UV light. Starting from a low-viscosity liquid material, UV imprinting can be performed at room temperature and moderate pressures. Compared to thermal imprinting, which involves time-consuming heating/cooling cycles and thermal expansion of patterns, UV imprinting has greater potential in terms of process speed and pattern replication fidelity. With a roller mold, Roll-to-roll (R2R) imprinting enables large-area and continuous fabrication of structured films and coatings, achieving throughputs potentially matching the demands of industrial applications.

During the past decade, the development in R2R imprinting has enjoyed great momentum. Guo *et al.*¹³⁸ pioneered the research in pilot-scale R2R nanoimprinting on flexible substrates, demonstrating the continuous fabrication of patterns down to 70 nm feature dimensions with a UV curable epoxysilicone material, which finds applications as wire-grid polarizers. Furthermore, they presented a thorough investigation on the residual layer thickness of imprinted coatings as a function of the web speed and the applied force.⁷⁸ Carter and his group reported R2R imprinting at sub-100 resolution with a commercial UV curable resin¹⁴² and successfully fabricated infrared sensors by subsequent deposition of carbon nanotubes¹⁴³. Recently, Peng *et al.* reported the implementation of anodic aluminum oxide molds in R2R nanoimprinting and the fabrication of multiscale features, achieving polymer surfaces with both antireflective and superhydrophobic properties.

These studies shed light on the great potential of R2R imprinting stepping into industrial applications, but available UV curable materials are still limited currently. Most previous studies are based on traditional UV curable materials, acrylates and epoxies. Acrylate materials cure fast and are readily available with a large number of monomers and oligomers. However, acrylates are known to suffer from oxygen inhibition and require inert atmospheres for high process speeds. In addition, the volume shrinkage of acrylates during curing can be as high as 10%, leading to loss of pattern accuracy and defects due to internal stress buildup. The curing of epoxies is not inhibited by oxygen and the volume shrinkage is smaller after curing, but the reaction speed is much lower compared

to acrylates. Another concern with epoxy materials in imprinting is their strong adhesion, which may lead to demolding failures and defects in replicated patterns.

Thiol-ene chemistry, as an alternative UV curable system, cures as fast as acrylates under ambient conditions and the level of shrinkage are lower.¹⁴⁴ There are only a few previous studies on the application of thiol-ene in R2R imprinting processing.¹⁴⁵ Li *et al.*¹⁴⁶ fabricated superhydrophobic coatings based on multifunctional thiol and ene monomers. Recently, Leitgeb *et al.*¹¹⁶ demonstrated the application of the thiol-ene-acrylate ternary system in R2R NIL processing and achieved the replication of multi-length scale patterns at high accuracy and process speed.

The research mentioned above demonstrated that thiol-ene chemistry is a promising candidate for high-throughput R2R NIL processing. However, the influence of processing variables on the quality of imprinted patterns is not fully understood. Especially, the curing content of imprinted films and coatings is of great importance from both processing and application perspectives. Insufficient cure of coatings lead to a lower modulus and result in permanent deformation during the demolding step. Additionally, residual reactive species in the patterned polymers can migrate to the surface over time, leading to long-term stability issues and raising potential health concerns.

This chapter aims to expand the material variety for R2R imprinting processing and unveil the effects of processing parameters on the curing of the patterned coating. We demonstrate a continuous and large-area R2R imprinting with a UV curable thiol-ene based coating system. The material system offers

great flexibility in achievable materials properties, including the liquid viscosity and the mechanical property of cured materials. All the coatings were sufficiently cured within a second under ambient conditions. Furthermore, the curing extents of patterned coatings were quantitatively analyzed with Fourier Transform Infrared Spectroscopy (FTIR) as a function of the lamp power, the lamp distance, and the web speed. Microscale surface patterns with various shapes and dimensions were successfully fabricated on a 5-inch wide flexible web at a web speed up to 1 cm/s.

5.2 Materials and Methods

5.2.1 Materials

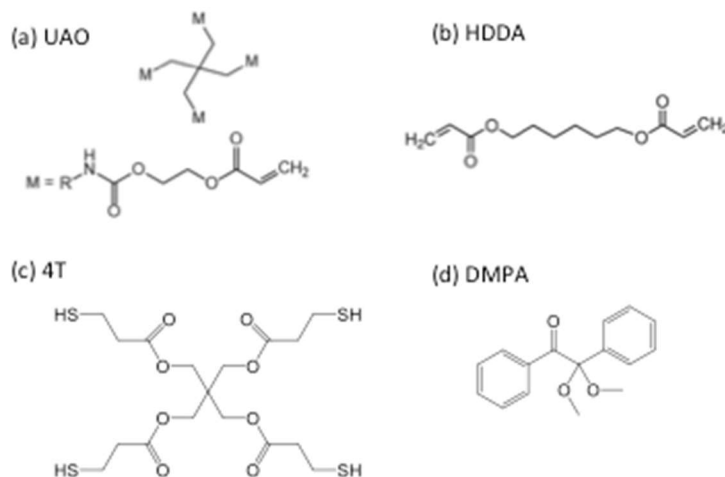


Figure 5.1 Materials of R2R UV imprinting coating formulations.

(a) Ebecryl 8210 (UAQ), (b) hexanediol diacrylate (HDDA), (c) pentaerythritol tetrakis(3-mercaptopropionate) (4T), and 2,2-dimethoxy-2-phenylacetophenone (DMPA).

Figure 5.1 shows the chemical structure of materials utilized in UV curable formulations. Ebecryl 8210 (UAQ) was a tetrafunctional acrylate oligomer ordered from Allnex. Hexanediol diacrylate (HDDA) was provided by

Sartomer. Pentaerythritol tetrakis(3-mercaptopropionate) (4T) and 2,2-dimethoxy-2-phenylacetophenone (DMPA) were purchased from Sigma-Aldrich. All the materials were used as received.

Table 5.1 summarizes the compositions of liquid formulations, percentages shown based on the total amount of functional groups (4T_f represents the thiol groups of the tetrathiol monomer, HDDA_f represents the double bonds of HDDA, and UAO_f corresponds to the double bonds of UAO). All the formulations contain 3 wt.% of DMPA as photoinitiators. All the components were added to a glass vial wrapped with aluminum foil and stirred for 4 h at room temperature.

Table 5.1 Compositions of R2R UV imprinting formulations

Formulation	4T _f (mol%)	HDDA _f (mol%)	UAO _f (mol%)
15-85_UAO50	15	42.5	42.5
20-80_UAO50	20	40	40
25-75_UAO50	25	37.5	37.5
30-70_UAO50	30	35	35
50-50_UAO50	50	25	25
20-80_UAO25	20	60	20
20-80_UAO75	20	20	60

5.2.2 Dynamic Viscosity Measurement

The dynamic viscosity of liquid coating formulations was measured on an AR-G2 rheometer (TA Instruments). The parallel plate geometry was used with a plate diameter of 25 mm and a gap of 1 mm. The measurements were performed at room temperature with the shear rate ranging from 1 to 100 s⁻¹.

5.2.3 FTIR spectroscopy

The curing kinetics of UV curable formulation was analyzed with on a Nicolet 6700 FTIR spectrometer in the transmission mode. Samples were prepared by sandwiching uncured resin between two sodium chloride plates. The sample thickness was 25 μm controlled by a steel spacer. Samples were exposed to UV at 210 mW/cm^2 with a mercury lamp (OmniCure 1500, Excelitas Technologies) inside of the IR chamber. A series of IR spectra were taken during at a sample interval of 0.02s. The spectrometer was operated at a resolution of 32 and 1 scan per spectrum.

The conversion of cured samples from the R2R experiment was determined with FTIR-ATR spectroscopy. Cured samples were placed in contact with a diamond crystal on the FTIR spectrometer. The peak areas of thiol (2570 cm^{-1}) and for acrylate double bond (1635 and 1619 cm^{-1}) were analyzed, normalized using the carbonyl IR peak (1725 cm^{-1}) as an internal reference. The conversion (x) of a functional group (thiol group at or double bonds) was determined by using equation 1:

$$x = \frac{A_0 - A_t}{A_0} \times 100\% \quad \text{Equation 5.1}$$

where A_0 is the peak area before curing and A_t is that after curing.

5.2.4 Photo-rheology measurement

The development of rheological behaviors of the resin during UV curing was characterized on a Discovery Hybrid Rheometer (DHR) with a UV curing accessory (TA Instruments). The parallel plate geometry was used for the

measurements with a diameter of 20 mm and a gap of 0.1 mm. A disposable aluminum plate was used as the top plate and a UV transparent quartz plate was used as the bottom. UV light was exposed through the bottom plate through the light guide to the OmniCure S2000 light source. The light source is a mercury lamp with peak illumination at 365 nm and light intensity adjustable through the power level setting. At power levels of 1%, 2%, 4%, 7%, and 10%, the measured UV intensities was 0.3, 1.3, 3.8, 7.2, and 11.6 mW/cm², respectively. A controlled strain of 1% was imposed on the sample at a frequency of 5 Hz. Rheological baseline was collected at the beginning of each measurement and UV light was turned on after 10 s. All measurements were performed at the ambient temperature.

5.2.5 *Dynamic mechanical analysis*

The dynamic mechanical analysis was conducted on an RSA-G2 solid analyzer (TA instruments) with a tension fixture. Samples were cured materials with dimensions of 20 mm (length) × 5 mm (width) × 0.18 mm (thickness). Curing conditions were UV curing at 500 mW/cm² for 2 min followed by thermal cure at 120°C overnight in the oven. A temperature ramp was performed from 25°C to 200°C at a heating rate of 3°C/min and a frequency of 1 Hz. The oscillation strain was 0.02% and was allowed for auto adjustment from 0.001% to 3%.

5.2.6 *Preparation of roller mold*

PDMS imprinting molds were prepared from master patterns fabricated on 4-inch diameter silicon wafers prepared by traditional photolithography processes (details of the fabrication conditions were described in Section 4.3.6). These patterns consisted of parallel raised lines and square dots 15 μm in depth, the lateral dimensions of which range from 10 μm to 80 μm . 30 grams of liquid PDMS (Sylgard 184, Dow Corning) at 10:1 base: curing agent by weight was mixed thoroughly and vacuum degassed to remove all air bubbles. The liquid PDMS was then poured over the silicon wafer master pattern in a petri dish and cured at 75 °C for 2 hours in an oven before demolding. The PDMS was then thermally annealed at 120 °C for 2 hours and 210 °C for two hours. The cured PDMS stamps were secured to a piece of silicone coated PET (Hotpress) using PDMS mixed at a 10:4 base: curing agent ratio as an adhesive. The assembled stamp was then cured for 24 hours at 45 °C. After curing, the stamp was clamped to the imprinting roller in the roll-to-roll imprinting line.



Figure 5.2 Roll-to-roll UV imprinting line at the University of Minnesota.

5.2.7 *Roll-to-roll imprinting line operation*

Roll-to-roll imprinting was performed on a commercial roll-to-roll nanoimprinting machine from Carpe Diem Technologies (shown in Figure 5.2). A clear 127 μm thick PET web was unwound and passed through a web cleaner. Then, reverse gravure coating was used to deposit a 25 μm thick layer of the UV-curable resin onto the web. The coated web then passed to the imprinting station where web tension pressed the UV-curable resin into the features of the imprinting stamp as the coated web passed around the imprinting drum. Web tension was maintained at 8.9 N during the imprinting process, and speed was varied to test imprinting conditions. While the web passed around the imprinting drum, it was illuminated through the PET web with a mercury arc lamp UV light source. The length of web illuminated (L) was controlled by adjusting the distance separating the light source from the web. Light intensity was also adjusted to test imprinting conditions. After curing, the web was delaminated from the imprinting drum and rewound on a collection drum.

5.3 **Results and Discussion**

We constructed UV curable coating formulations based on four main components. A tetrafunctional thiol monomer, pentaerythritol tetrakis(3-mercaptopropionate) (4T), was selected due to its fast cure and the capability to reduce oxygen inhibition. A tetrafunctional urethane acrylate oligomer (UAO) was selected because of the high functionality and relatively low molar mass in consideration of the cure speed and the liquid coating viscosity. The selected

UAO has been widely used as a crosslinker in UV curable acrylate systems to provide fast cure and good mechanical properties in applications such as protective coatings^{147, 148} and 3D printing¹⁴⁹. In addition, an acrylate monomer, hexanediol diacrylate (HDDA) was used as a reactive thinner to reduce the formulation viscosity to facilitate mold filling. Last, 2,2-dimethoxy-2-phenylacetophenone (DMPA) was used as the photoinitiator to induce photopolymerization. Two sets of formulations were prepared to optimize for R2R UV imprinting applications. First, the molar ratio between thiol groups and double bonds was varied from 15:85 to 50:50, with the molar ratio of double bonds from UAO kept at 50% for all formulations. Second, the molar ratio between UAO and the acrylate monomer was varied while the thiol and double bond ratio were constant.

For the optimization towards R2R UV NIL applications, three criteria were considered: liquid coating viscosity, cure speed, and the modulus of cured materials. A relatively low viscosity was preferred to facilitate mold filling but too low a viscosity can decrease the liquid coating thickness, which may lead to unfilled defects. For UV curing, high cure speeds are highly demanded because it is considered as the current bottle neck for further enhancing the total process speed. Additionally, coatings need to reach sufficient cure extents after curing to avoid the existence of excess free monomers. Furthermore, the modulus of the cured coating should be high enough to withstand the mechanical deformation during demolding. At the same time, a certain extent of flexibility is necessary to allow for the release of surface microstructures from the mold.

5.3.1 Characteristics of Liquid Formulations

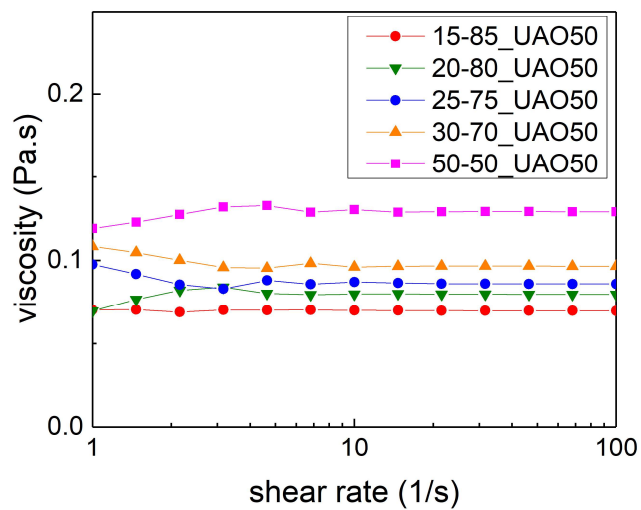


Figure 5.3 Dynamic viscosity for coating formulations with different ratios of thiol groups and acrylate double bonds.

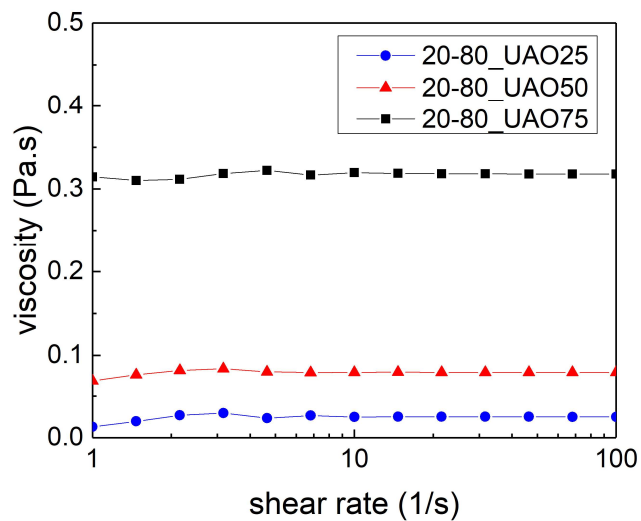


Figure 5.4 Dynamic viscosity for formulations with various UAO contents.

All the formulations are Newtonian liquids in the range of shear rates investigated. The coating viscosity was adjustable over a wide range from 0.03 Pa·s to 0.3 Pa·s, which increased with the content of acrylate mixtures and was dominantly affected by the amount of UAO (Shown in Figure 5.3 and 5.4). It is comparable to the viscosities of commercial benchmarks of UV curable resists and much lower than those of resins during thermal imprinting.¹⁰⁹

5.3.2 *Curing kinetics*

Curing kinetics is important to R2R UV imprinting applications because high cure speeds enable high-throughput production and sufficient cure extents guarantee application-related requirements, such as safety concerns, hardness of cured materials, and long-term stability. In thiol-ene chemistry, the curing kinetics are influenced by the functionality of monomers and oligomers, the reactivity of functional groups, the stoichiometric ratio of thiol-to-ene functional groups, and the viscosity of formulations.¹⁷

In this research, monomers and oligomers with high functionalities and reactivities were selected to formulate coating materials. The ratio between different components was adjusted to investigate the effects of thiol-to-ene ratio and the coating viscosity on curing behaviors.

To quantitatively investigate how the curing speed and extent vary with different formulations, real-time FTIR was performed on the aforementioned coating formulations at UV intensity comparable to that used on the R2R imprinting line, i.e. 500 mW/cm². The UV light was turned on 5 seconds after the

start of IR spectrum collection. Both the thiol group and the double bond conversion were analyzed according to their characteristic IR peaks at 2570 and 810 cm^{-1} , respectively.

In Figure 5.5, the double bond conversion was plotted against the exposure time for coatings with various concentrations of thiol groups, ranging from 15% (for 15-85_UAO50) to 50% (for 50-50_UAO50) based on the molar ratio of functional groups. All the coating formulations react instantly upon UV exposure, reaching the limiting conversion within a second. As the thiol-to-ene ratio increases, both the reaction speed and the limiting conversion of double bonds increase. Similar trends were observed in previous studies on thiol-ene curing kinetics at lower light intensities.³⁴ The presence of thiol accelerates the reaction of acrylate double bonds by reducing the oxygen inhibition effects.¹⁵⁰ Moreover, the formulation viscosity decreases with the addition of thiols, which increases the mobility of reactive species and decreases the tendency of trapping radicals in solidified polymer networks, therefore leading to higher reaction rate and conversions.¹¹⁶

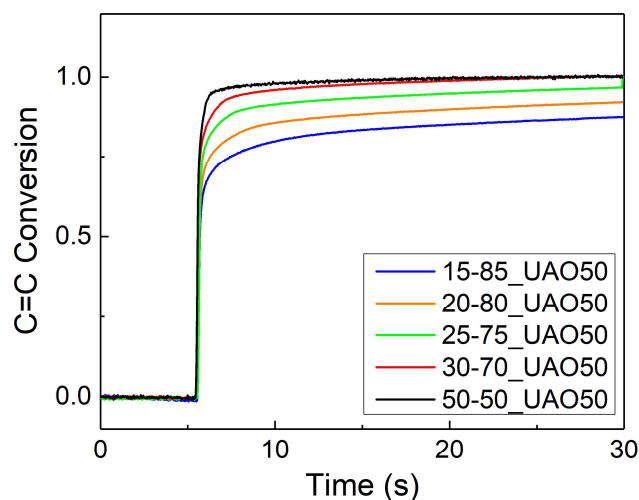


Figure 5.5 Double bond conversion for formulations with different thiol-to-ene ratio recorded by real-time FTIR.

Experiments were performed at a light intensity of 500 mW/cm². The ratio between UAO and HDDA was constant. Coatings were exposed to air at a thickness of 20 μ m.

According to **Figure 5.6**, the thiol groups were sufficiently cured with a conversion of about 80% except for the formulation containing 50% thiol groups (50-50_UAO50), which is due to the completion between the thiol-acrylate reaction and the acrylate homopolymerization. Typically, a conversion of about 80% is considered to guarantee acceptable material properties with respect to the final application. Therefore, for UV curable thiol-acrylate formulations, a thiol group concentration of 20 to 30% is optimal for both the reaction rate and curing extent considerations.

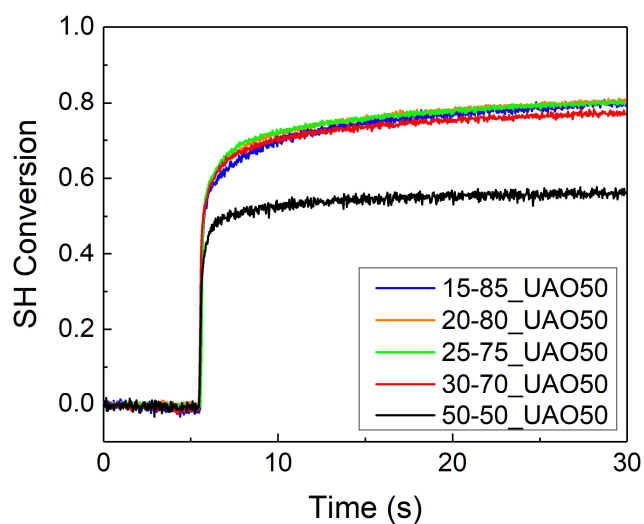


Figure 5.6 Thiol conversion for formulations with different thiol-to-ene ratio recorded by real-time FTIR.

Experiments were performed at a light intensity of 500 mW/cm^2 . The ratio between UAO and HDDA was constant. Coatings were exposed to air at a thickness of $20 \mu\text{m}$.

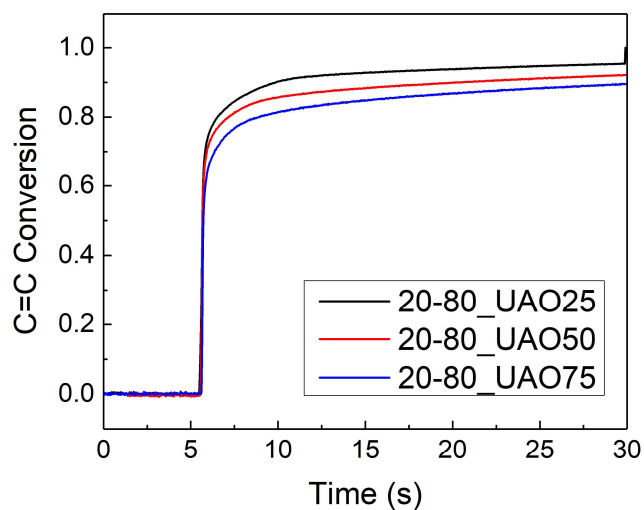


Figure 5.7 Double bond conversion coating formulations with various UAO content.

Experiments were performed at UV intensity of 500 mW/cm^2 . The thiol-to-ene

ratio was kept constant. Coatings were exposed to air at a thickness of 20 μm .

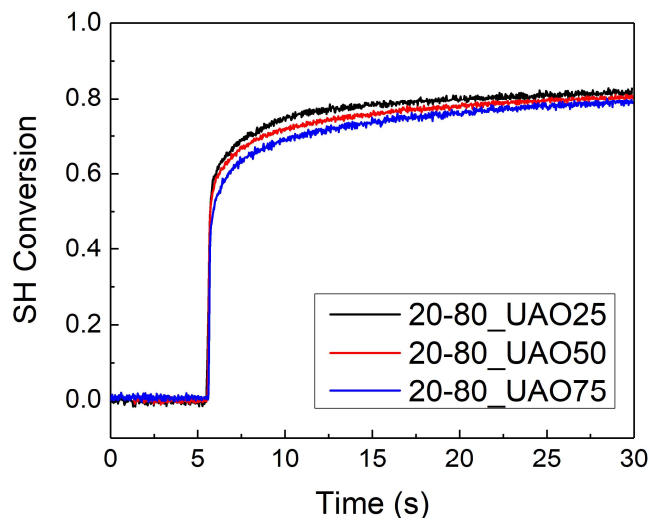


Figure 5.8 Thiol group conversion for coating formulations with various UAO content.

Experiments were performed at UV intensity of 500 mW/cm^2 . The thiol-to-ene ratio was kept constant. Coatings were exposed to air at a thickness of 20 μm .

Another series of thiol-acrylate formulations were prepared with a controlled thiol-acrylate ratio (20% thiol group) but various UAO-to-HDDA ratios. In the nomenclature of formulations, the number following UAO indicates the percentage of double bonds from UAO out of the total amount of double bonds. According to **Figure 5.7** and Figure 5.8, all the formulations exhibit high cure speeds, reaching sufficient cure in less than a second. However, the limiting conversions of double bonds and thiol groups slightly decrease with increasing the oligomer concentration. This could be explained by the fact that the higher viscosity of the oligomer restricts the mobility of propagating radicals.

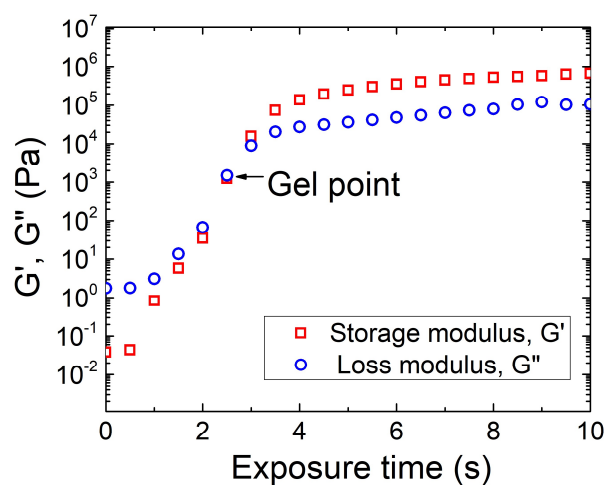


Figure 5.9 Dynamic storage and loss moduli versus UV exposure time measured by photo-rheology.

The measurement was performed with the 20-80_UAO50 formulation at a light intensity of 1.3 mW/cm², a film thickness of 0.2 mm, and ambient temperature.

Representative photo-rheology results for the formulation of 20-80_UAO50 were shown in **Figure 5.9**. The storage modulus (G') and the loss modulus (G'') increase with the exposure time. The mechanical gelation is defined as the crossover of $G'=G''$.¹⁵¹ Therefore, the gel time at an intensity of 1.3 mW/cm² was 2.7 s for the formulation of 20-80_UAO50. After gelation, the growth of storage and loss moduli slowed down and reached their plateau values.

Table 5.2 Gel times of coating formulations at different light intensities.

Coating formulation	Power level, %	Light intensity, mW/cm ²	Gel time, s
20-80_UAO25	1	0.3	5.1
	2	1.3	3.6
	4	3.8	2
20-80_UAO50	1	0.3	3.1
	2	1.3	2.7
	4	3.8	1.7
20-80_UAO75	1	0.3	3
	2	1.3	2.7
	4	3.8	1.8

Coating formulations with different oligomer concentrations but the same thiol-to-ene ratio were investigated, results shown in Table 5.2. As expected, for each formulation, the time to reach the gel point decreases with increasing the light intensity because of the fast photopolymerization. However, as the concentration of oligomers increase, the gel time decreases at a comparable light intensity. With more oligomers in the coating formulation, although the reaction is slowed down due to the increased formulation viscosity, the polymer networks are more crosslinked due to the high functionality of the oligomers. In the investigated series of formulations, the effects coming from polymer network structures appear to have larger effects on the observed gel time. Additionally, it should be mentioned in the roll-to-roll imprinting experiments as discussed below, the light intensity was higher and the coating thickness was lower compared to those in photo-rheology measurements, so the gel time is expected to be shorter. For all the formulations, the gelation took place within seconds, confirming their high throughput potential.

5.3.3 *Mechanical properties of cured materials*

Figure 5.10 shows the temperature-dependent viscoelastic properties of cured coating formulations with various UAO content. The three formulations have the same thiol-to-ene ratio (20% thiol groups) and the percentage of double bonds from UAO was varied from 25% to 75%.

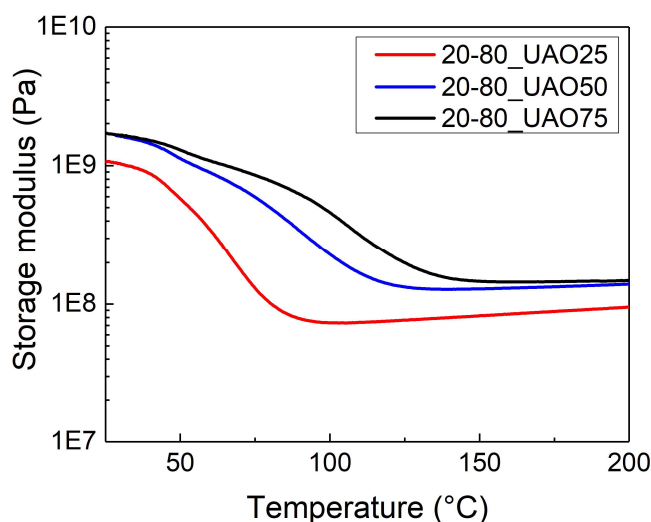


Figure 5.10 Storage modulus as a function of temperature for cured materials with different UAO concentrations.

After curing, the materials develop high elastic moduli of 1-2 GPa at the room temperature and exhibit glass transition temperatures higher than room temperatures, indicating the formation of hard and glassy materials. According to **Figure 5.10**, the plateau storage modulus at high temperatures increases with the UAO content. Based on the ideal rubber elasticity theory, it is suggested that the crosslinking density of cured polymer networks increase with the addition of high-functionality oligomers.¹⁵²

From $\tan\delta$ curves shown in Figure 5.11, the T_g values were 75°C, 95°C, and 115°C for formulations containing 25%, 50%, and 75% UAO double bonds, respectively. Furthermore, $\tan\delta$ peaks broaden as UAO content increases, suggesting a lower degree of network homogeneity due to the heavily cross-linked polymer networks.³⁷

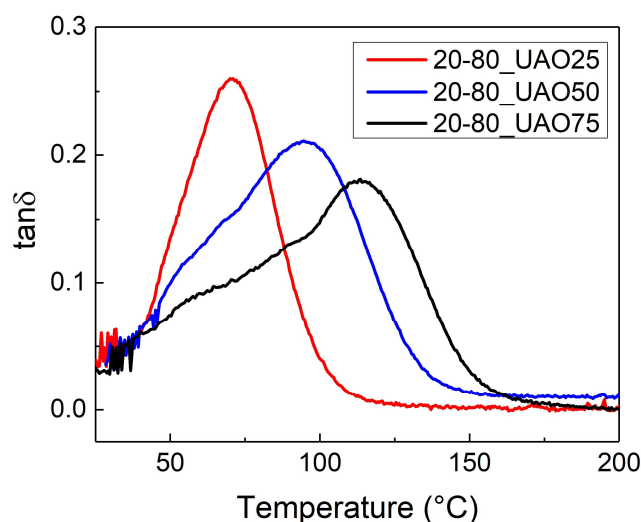


Figure 5.11 Tan δ as a function of temperature for cured materials with different UAO concentrations.

5.4 R2R UV Imprinting

5.4.1 Effects of thiol and oligomer contents on conversions

R2R UV imprinting experiments were performed with in-house prepared thiol-ene coating formulations. All the formulations were coated using a reverse gravure coating unit, forming a uniform liquid coating on a PET web. The roller mold was wrapped with a PDMS mold, which imprints coatings continuous with microscale regular patterns. Due to the relatively low viscosities of thiol-ene formulations, 0.03 to 0.3 Pa·s, the mold cavities were successfully filled without significant bubble defects on the cured coating. In addition, cured coatings were peeled off from the mold without any problems, due to the low surface energy of the PDMS mold and the sufficient mechanical strength of cured materials.

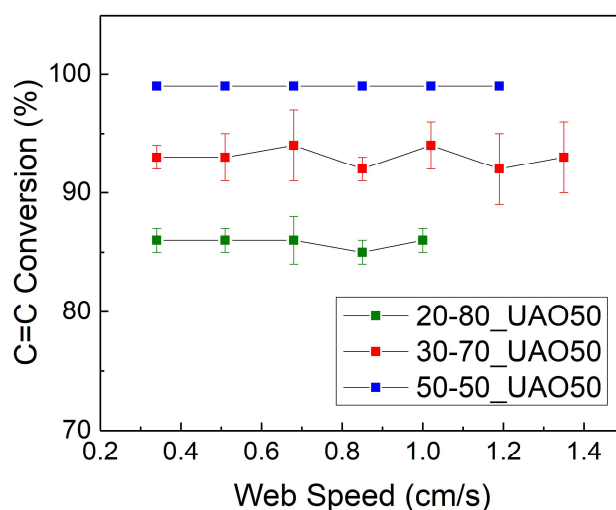


Figure 5.12 Double bond conversions of thiol-ene coatings plotted against the web speed of R2R imprinting for formulations with different thiol-to-ene ratios.

Conversions were measured with FTIR-ATR on the top surface of the coating in contact with mold and averaged over three parallel measurements.

The curing extents of the UV imprinted coatings were characterized with FTIR ATR and plotted against the web speed. Due to a limited penetration depth of the ATR technique (c.a. 1 μm from the coating surface) and the relatively small amounts of thiol groups in the formulation, the thiol peaks were noisy and thus not employed for the analysis in this section. The curing extents of imprinted coatings were represented by the double bond conversion and plotted against the web speed in Figure 5.12. It is suggested that all the coating formulations were sufficiently cured in the invested range of web speeds. According to Figure 5.12, the limiting double bond conversion increases with the thiol-to-ene ratio increases, similar to the trend observed in the real-time kinetic study shown in Figure 5.5. This suggests that the addition of thiol monomers facilitate the curing

of acrylates, which could be attributed to a reduced oxygen inhibition effects and a lower viscosity of the formulation. However, the limiting conversion values of imprinted coatings measured by ATR (Figure 5.12) were slightly lower compared to those measured in the transmission mode (Figure 5.5) for the same formulation, respectively. The observed difference may come from the characterization technique and a depth-wise conversion gradient. The ATR data represents the coating surface conversion while in the FTIR technique the average conversion throughout the coating thickness is characterized. Therefore, it is suggested that the surface conversion was slightly lower, which could be attributed to the presence of oxygen in the PDMS mold inhibiting the polymerization. In addition, because the coating was exposed to UV from the surface in contact with the web, the light intensity at the top surface was lower due to the UV light attenuation, leading to a lower conversion. As discussed previously, the thiol conversion was not complete in a stoichiometric mixture of thiol and ene groups (50-50_UAO50) although the double bond conversion was higher. The thiol-ene ratio was kept at 30 to 70 in the following study of oligomer contents on R2R imprinting.

As shown in Figure 5.13, lowering the oligomer content of a formulation raises the double bond conversion, especially at high web speeds. With the formulation containing 25% oligomer (30-60_UAO25), a web speed of 2.7 cm/s was achieved at high pattern fidelity while at the same time maintaining a high curing extent (85% conversion of double bonds). As the ratio between UAO (molar mass, $M=400$ g/mol; functionality, $f=4$) and HDDA ($M=230$; $f=2$) varies, the initial double bond concentration (proportional to f/M) was similar. The main

difference among these formulations results from an increase formulation viscosity associated with higher UAO content, which slows down UV curing because of the limited mobility of reactive species. In comparison, the attainable web speed was 0.17 cm/s with a commercially available optical adhesive

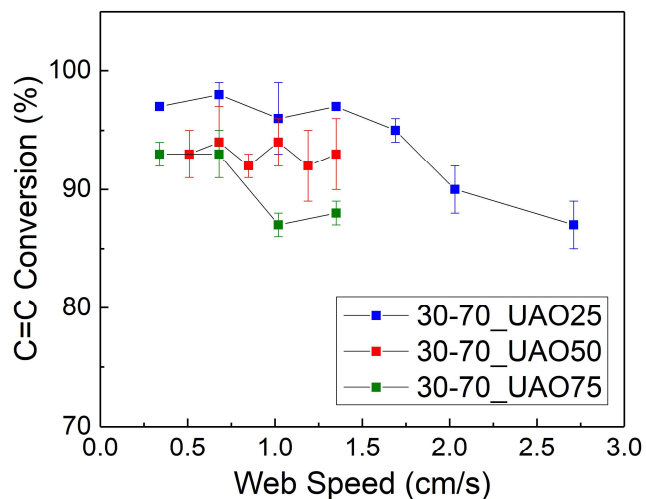


Figure 5.13 Double bond conversions of thiol-ene coatings plotted against the web speed of R2R imprinting for formulations with different oligomer contents.

Conversions were measured with FTIR-ATR on the top surface of the coating in contact with mold and averaged over three parallel measurements.

(NOA73) under same imprinting conditions, which is 15 times slower than a thiol-ene based formulation.

3.2.2. Effects of processing variables on conversions

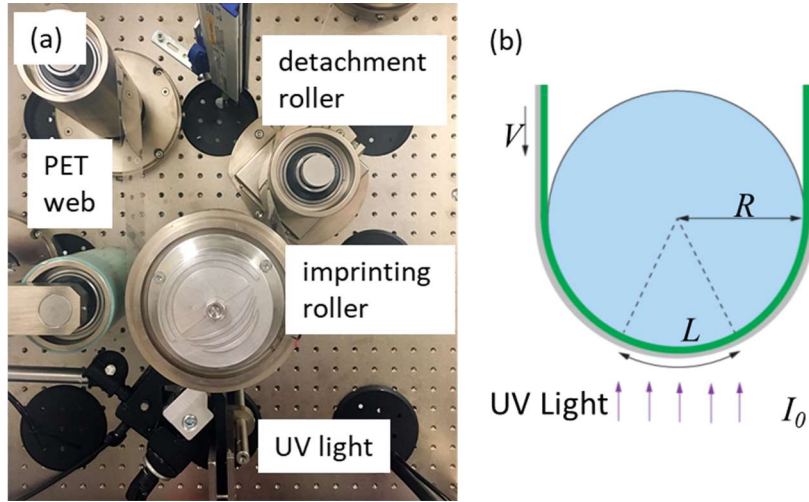


Figure 5.14 (a)UV imprinting unit of the R2R pilot coating line. (b) Schematic of the imprinting unit.

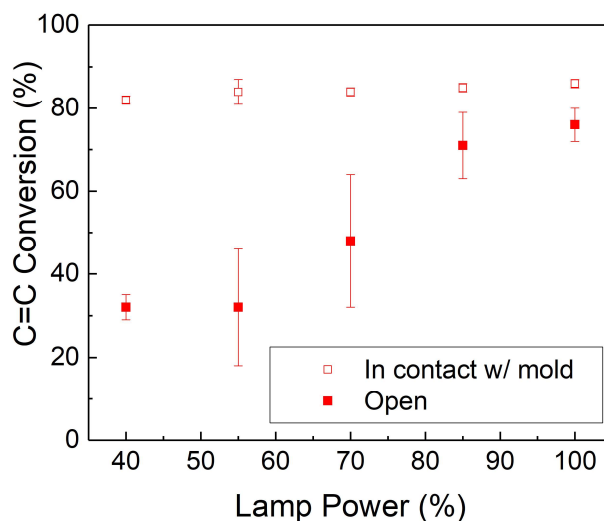
The UV curing of the coating during the roll-to-roll micromolding process is crucial to the successful fabrication of the surface microstructures, affecting both the microstructure integrity, mechanical properties, and long-term stability. The curing extent is determined by the UV dosage received by the coating, which can be calculated by the following:

$$J = I_a \times t = \frac{I_0 L}{V} (1 - e^{-d/d_p}) \quad \text{Equation 5.2}$$

Here, J is the curing dosage, I_a and I_0 are the absorbed light intensity and the initial light intensity, respectively, L is the length of UV exposure area on the roller mold (shown in Figure 5.14), d and d_p are the coating thickness and its penetration depth respectively. As demonstrated in equation 5.2, the curing extents depend on both process parameters ($I_0 L/V$) and coating characteristics (d/d_p).

Table 5.3 Base processing conditions for UV R2R Imprinting

Parameter	Base condition
Lamp power (%)	100%
Lamp distance (cm)	0.75 cm
Web speed (cm/s)	0.34 cm/s

**Figure 5.15 Effect of lamp power on conversion of imprinted coatings.**

The lamp distance was 0.34 cm and the web speed was 0.34 cm/s.

The influence of light intensity on the double bond conversion was investigated with FTIR-ATR. As the lamp power was varied from 40% to 100%, the UV intensity increased proportionally with the lamp power from 220 mW/cm² to 500 mW/cm². As shown in **Figure 5.15**, different conversions were observed across the cured coating: the area in contact with mold reached a plateau conversion at the lowest lamp power, and in contrast, the curing of the open area needs a much higher lamp power due to oxygen inhibition. In the presence of oxygen, increasing the intensity leads to not only a faster initiation rate but also

suppressed oxygen inhibition due to the faster viscosity build-up, both contributing to the strong dependence of conversion on UV intensity.

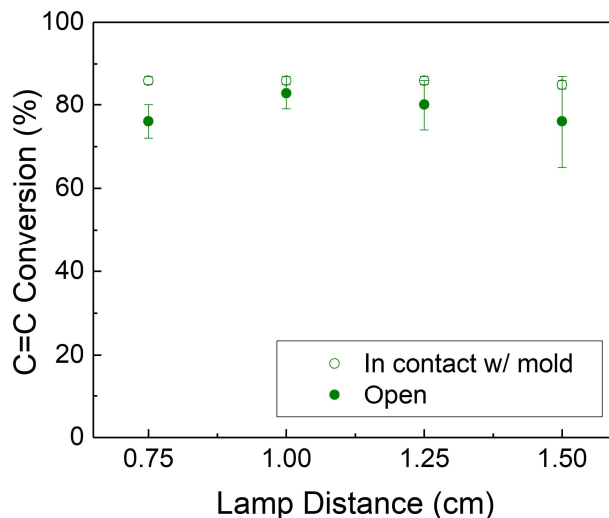


Figure 5.16 Effect of lamp distance on the imprinted coating conversion at a lamp power of 100% and a web speed of 0.34 cm/s.

The effect of lamp distance on the conversion of imprinted coatings was investigated. As the distance from lamp to web was varied from 0.75 cm to 1.5 cm, the UV intensity decreased from 500 mW/cm² to 220 mW/cm² and the exposure length along the web moving direction expanded from 1.6 cm to 3.1 cm. Therefore, the UV light distribution rather than the total UV dosage will change with the lamp distance. The double bond conversions as a function of lamp distance for the area in contact with mold and the open area were shown in Figure 5.16. The conversion is invariant to the lamp distance, indicating the curing extent of coating depends on the total UV dosage and is insensitive to the light distribution.

At controlled UV exposure conditions (lamp power and lamp distance), the effect of web speed on the imprinted coating conversion was studied. As shown in Figure 5.17, the patterned area of coating (in contact w/ mold) can be sufficiently cured at a web speed up to 1 cm/s. However, the unpatterned area of the coating was tacky at high web speeds. The corresponding double bond conversion decreased significantly from 80% to 30% when increasing the web speed because of less exposure time and the resulting insufficient UV dosage.

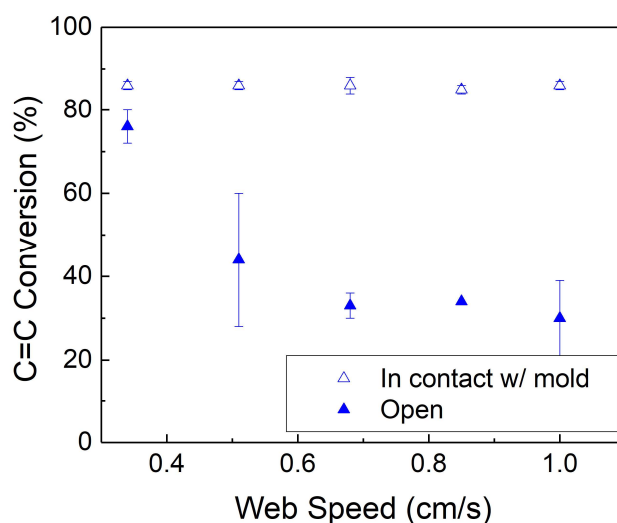


Figure 5.17 Effect of web speed on the imprinted coating conversion at a lamp power of 100% and lamp distance of 0.34 cm.

Overall, curing with higher lamp powers and reduced web speeds produces a similar effect on the imprinted coating conversions. There is a lack of dependence of conversion on the lamp distance assuming the total UV energy received by the materials is the same. According to Equation 5.2, the UV dosage is proportional to $\frac{I_0 L}{v}$ for a specific coating system in the roll-to-roll imprinting process. Further study of coatings imprinted with different processing variables

(lamp power, lamp distance, and web speed) show that the coating conversion was predominately determined by the exposure dosage as shown in Figure 5.18. The critical exposure dose for the coating system to reach the plateau conversion is less than 800 mJ/cm² on the patterned area. For the area of coating cured in air, the critical dose significantly climbed to 2000 mJ/cm² due to oxygen inhibition. Given the curing conditions (intensity and exposed web length), the achievable web speed can be estimated with the critical exposure dosage. In addition, by improving the mold design to avoid any open area of the coating, we can further ramp up the roll-to-roll process speed without sacrificing the curing extent.

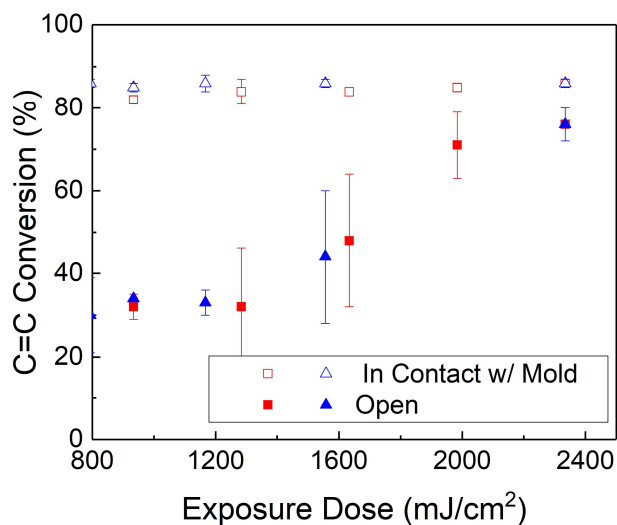


Figure 5.18 Influence of exposure dosage on the imprinted coating conversion.

3.3. Continuous Fabrication of Microstructured Coatings

The patterning process with thiol-ene based formulations was successfully scaled up on an R2R UV micromolding pilot line. The 20-80_UAO50 formulation was selected for the large-area fabrication of microstructured coatings

and a web speed of 0.6 m/min was achieved. Figure 5.19 displays SEM images of microstructures on the surface of cured coatings. Surface microstructures with various shapes, square dots, and channels, were replicated. The patterns are 10 μm in depth and the lateral dimensions of which range from 10 μm to 80 μm . The exact pattern replication from the roller mold to the UV curable thiol-ene coating demonstrates the excellent pattern replication fidelity of the R2R micromolding process and the scale-up capability of the custom coating formulations.

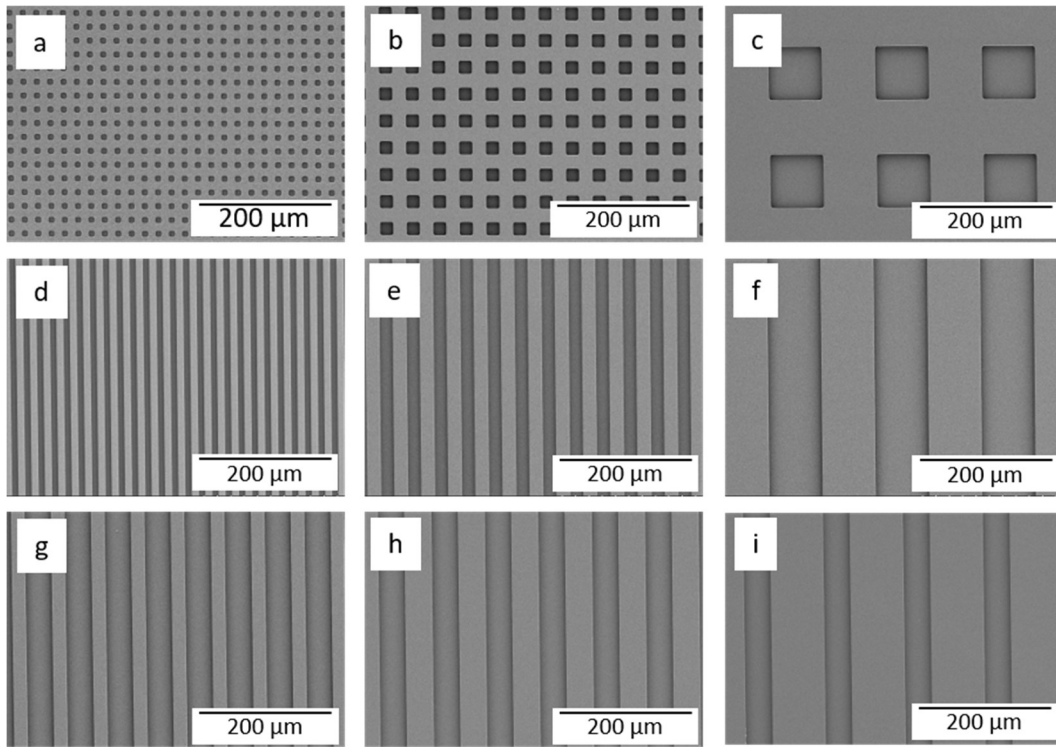


Figure 5.19 R2R micromolding fabricated patterns with the 20-80_UAO50 coating formulation

(a-c) square dots with pattern widths of 10, 20, 80 μm , respectively; (d-f) microchannel arrays with channel widths of 10, 20, 80 μm , respectively, and width: spacing = 1:1 for all three patterns; (g-i) microchannel arrays with width: spacing = 2:1, 1:1, and 1:2, respectively, a channel width of 40 μm for all three patterns. All the surface microstructures were 10 μm in depth.

5.5 Summary

In this chapter, the continuous fabrication of microstructured coatings with UV curable thiol-ene formulations was demonstrated. The liquid viscosity and the elastic modulus of cured materials were tunable over a wide range by adjusting the thiol-to-ene ratio and the oligomer content. All the coating formulations cured fast under UV exposure, achieving high double bond conversions, c.a. 80%, within seconds. Roll-to-roll imprinting was achieved with the formulated thiol-ene-acrylate coatings at ambient conditions. The limiting double bond conversions increase with increasing the thiol-to-ene ratio and decreasing the urethane acrylate content. In addition, the effects of processing variables on the curing conversions for a representative coating formulation were investigated. FTIR results revealed that the curing extent increase with the UV exposure dose, which is proportional to the light intensity and the exposure length, and inversely proportional to the web speed. The maximum achievable web speed with the custom thiol-ene-acrylate formulations was 0.8 mm/min. Compared to a commercial benchmark (NOA73), the achievable web speed leads to a 6-fold increase under the same processing conditions.

6 Summary and Future Directions

6.1 Summary

First, this work presented in this thesis advances the understanding of the UV curing kinetics under intense pulsed irradiation. Ultrafast photopolymerization of acrylate resin is attained within a few milliseconds with a single pulse from the xenon flash lamp, which is among the fastest curing processes recorded. In our model coating system, the achievable conversion with IPL curing is determined by the total irradiation dose, which increases and then levels off at a specific dose. The maximum achievable conversion is comparable to that attained with low-intensity mercury lamps and insensitive to changes in other variables, including the average dose rate and the PI concentration. IPL curing process with multiple pulse patterns cures acrylate coatings at a higher energy efficiency compared to the single pulse curing, and the time to maximum achievable conversion can be reduced to a few seconds with higher irradiation dose rates, attained by increasing the lamp voltage, the pulse duration and decreasing the pulse width. The achievable extent of cure can be increased effectively by curing at elevated temperatures, owing to the restored mobility of reactive species, but the advantage of the ambient cure of IPL curing is lost.

Second, a robust micro molding approach integrating the thiol-ene polymerization and the UV LED curing has been demonstrated. The moduli of cured thiol-ene coatings were tuned over two orders of magnitude by simply

adjusting the acrylate concentration of a coating formulation, and curing was complete within 10 seconds of LED exposure. Surface properties were modified with a fluorinated polymer, achieving a surface energy reduction of more than a half at a loading of 1 wt%. Densely packed 50- μm -wide gratings were faithfully replicated in coatings from soft materials to stiff highly crosslinked networks. 100- μm -tall defect-free patterns were attained with the introduction of fluorinated additives. The demolding strengths of microstructured coatings were quantitatively compared using peel testing, which increased with the coating surface energy, the coating modulus, and the grating height. This micromolding process combined with the tunability in thermomechanical and surface properties makes thiol-ene microstructured coatings attractive candidates for functional optical films, superhydrophobic surfaces, and flexible electronics.

Finally, the continuous fabrication of microstructured coatings and films were demonstrated on a roll-to-roll imprinting system with thiol-ene-acrylate coating formulations. The liquid and cured properties and their influences on the imprinting process were systematically investigated. The maximum achievable conversion increased with increasing the relative thiol content and decreasing the viscous urethane acrylate oligomer content. Furthermore, the UV lamp power, the lamp distance, and the web speed were systematically varied to elucidate the parameter interactions affecting the process throughput. Defect-free and well-cured microstructured coatings were formed only given sufficient exposure dosage, which is proportional to the lamp power, inversely proportional to the web speed, and independent of the lamp distance. Microscale channel and dot

arrays with various dimensions and pattern densities were continuously fabricated at web speeds up to 2.7 cm/s. Our findings expand the available materials space and can serve as a predictive guideline for the selection of processing conditions for the manufacturing of microstructures using roll-to-roll imprinting processes, opening up potential applications in areas of textured coatings, superhydrophobic surfaces, and printed electronics.

6.2 Future Directions

6.2.1 Metal-polymer nanocomposite

Metal-polymer composites are an interesting class of materials for UV curing applications. Traditionally, metal-polymer composites are fabricated via top-down approach, where metal nanoparticles are dispersed into the polymer matrix. However, achieving good dispersion of nanoparticles remains a challenge. Alternatively, nanoparticles can be synthesized within a UV curable system with UV exposure.¹⁵³⁻¹⁵⁵ Specifically, in this bottom-up approach, metal salts can be mixed with a UV curable formulation and then photochemically reduced to form nanoparticles upon UV exposure. The *in situ* formation of nanoparticles can avoid agglomeration and limit the particle size. Careful control of the metal salt concentration and processing conditions may allow for the preparation of UV curable conductive materials. Combined with surface replication technology, the metal-polymer composite system is a promising candidate to fabricate flexible electronics. Moreover, it is possible to prepare

microfluidic chips combining the antimicrobial characteristic of silver-polymer composite materials^{156, 157} and surface replication techniques.

6.2.2 *Inorganic-organic hybrid materials*

Polyhedral oligomeric silsesquioxanes (POSS), composed of a siloxane cage structure and pendant functional groups, is emerging as a class of inorganic-organic hybrid materials.^{41, 115, 158} The rigid core imparts POSS with excellent thermal stability and mechanical strength. At the same time, the pendant functional groups make POSS compatible with a variety of polymer matrix. Especially, POSS with pendant acrylate double bonds can be incorporated in thiol-ene based formulations and used in UV imprinting applications. The UV curable materials containing POSS been shown to have good optical clarity, high etch resistance, and thermal stability. In addition, because the dimension of POSS is on the order of nanometers, good pattern fidelity of replicated surface nano/microstructures can be achieved is POSS is well dispersed.

Phase separated composite

Polymer composite materials can be fabricated by phase separation of two interpenetrating networks with different crosslinking densities and glass transition temperatures.³⁷ Phase separation can take place during UV curing between UV networks and the materials properties can be tailored by monomer structures, functionalities, and processing conditions. Phase-separated hybrid materials may exhibit high toughness due to the increased interfacial area. Employing phase-

separated materials in UV imprinting processes will allow for the fabrication of microstructured films with improved toughness.

6.2.3 *Fluorinated mold materials*

The fabrication of roller molds with high replication accuracy and low cost is highly demanded the fabrication of microstructured films and coatings at large area. Currently, silicon, quartz, nickel, and silicon nitride have been utilized to fabricate hard molds for roll-to-roll imprinting.¹⁵⁹ However, their fabrication requires a clean room environment and etching process and thus relatively high cost. Alternatively, soft polymer molds can be fabricated at lower costs but may suffer from limited timespan and resolution issues at high pressure.¹⁶⁰ The thiol-ene UV curable formulation containing fluorinated additives (TEF) can serve as a promising mold material. It can be patterned at room temperature by the roll-to-roll imprinting process to produce microstructured coating at large-area. The flexible TEF coating on polymer substrates can be wrapped around a steel roller as the roller mold. Due to a high crosslinking density and high modulus (500 MPa), the TEF based mold is expected to have a longer lifetime. In addition, the low surface energy can allow for the clean release of the surface pattern. In the future, fluorinated polymers with pendant double bonds can be synthesized as a reactive additive for the flexible mold fabrication. In this case, the additives can polymerize with the UV curable monomers and be covalently bonded to the polymer network, thus increasing the wear resistance of the fluorinated material.

6.2.4 *Multilevel patterns*

Currently, process overlay and long-range placement accuracy are still challenging for the application of roll-to-roll imprinting process in flexible electronics. This is mainly due to the flexibility of the web and thus its tendency to deform especially at high processing speeds. To address this challenge, self-aligned imprinting lithography (SAIL) has been developed which utilizes a stamp with multilevel patterns for imprinting. The stamp encodes all the geometric information into pre-aligned structures, enabling the entire device fabrication process into one step and significantly reducing the process complexity and cost. Although R2R manufacturing with SAIL has been demonstrated in a previous study¹⁶¹, a robust UV curable material is demanded to understand the fundamentals and to enable the wide application of the process. Due to the presence of multilevel surface features, the clean release of patterns will be more challenging. It is possible to design a dual-cure coating system to facilitate the mold release process without sacrificing the final mechanical properties, which include a UV curable phase and a thermally curable phase in the coating formulation. Upon UV exposure, the UV phase solidifies to a soft layer with a relatively crosslinking density and transfers the pattern from the mold. In the following post-processing step, a second thermal cure step takes place to significantly enhance the mechanical properties.

7 References

- (1) Weiss, K. D. Paint and Coatings: A Mature Industry in Transition. *Progress in Polymer Science* **1997**, 22, 203-245.
- (2) Park, Y. J.; Lim, D. H.; Kim, H. J.; Park, D. S.; Sung, I. K. Uv- and Thermal-Curing Behaviors of Dual-Curable Adhesives Based on Epoxy Acrylate Oligomers. *International Journal of Adhesion and Adhesives* **2009**, 29, 710-717.
- (3) Park, Y. J.; Chae, K. H.; Rawls, H. R. Development of a New Photoinitiation System for Dental Light-Cure Composite Resins. *Dental Materials* **1999**, 15, 120-127.
- (4) Kats, M. A.; Blanchard, R.; Genevet, P.; Capasso, F. Nanometre Optical Coatings Based on Strong Interference Effects in Highly Absorbing Media. *Nature Materials* **2013**, 12, 20-24.
- (5) Zhang, X.; Shi, F.; Niu, J.; Jiang, Y. G.; Wang, Z. Q. Superhydrophobic Surfaces: From Structural Control to Functional Application. *Journal of Materials Chemistry* **2008**, 18, 621-633.
- (6) Unger, M. A.; Chou, H. P.; Thorsen, T.; Scherer, A.; Quake, S. R. Monolithic Microfabricated Valves and Pumps by Multilayer Soft Lithography. *Science* **2000**, 288, 113-116.
- (7) Thorsen, T.; Maerkl, S. J.; Quake, S. R. Microfluidic Large-Scale Integration. *Science* **2002**, 298, 580-584.
- (8) Hu, L. B.; Kim, H. S.; Lee, J. Y.; Peumans, P.; Cui, Y. Scalable Coating and Properties of Transparent, Flexible, Silver Nanowire Electrodes. *Acs Nano* **2010**, 4, 2955-2963.
- (9) Forrest, S. R. The Path to Ubiquitous and Low-Cost Organic Electronic Appliances on Plastic. *Nature* **2004**, 428, 911-918.
- (10) Crone, B.; Dodabalapur, A.; Lin, Y. Y.; Filas, R. W.; Bao, Z.; LaDuca, A.; Sarpeshkar, R.; Katz, H. E.; Li, W. Large-Scale Complementary Integrated Circuits Based on Organic Transistors. *Nature* **2000**, 403, 521-523.
- (11) Liddle, J. A.; Gallatin, G. M. Nanomanufacturing: A Perspective. *Acs Nano* **2016**, 10, 2995-3014.
- (12) Xia, Q. F.; Pease, R. F. Nanoimprint Lithography 20 Years On. *Nanotechnology* **2015**, 26, 3.
- (13) Decker, C.; Viet, T. N. T.; Decker, D.; Weber-Koehl, E. Uv-Radiation Curing of Acrylate/Epoxy Systems. *Polymer* **2001**, 42, 5531-5541.
- (14) Pease, R. F.; Chou, S. Y. Lithography and Other Patterning Techniques for Future Electronics. *Proceedings of the Ieee* **2008**, 96, 248-270.

- (15) Andrzejewska, E.; Andrzejewski, M. Polymerization Kinetics of Photocurable Acrylic Resins. *Journal of Polymer Science Part a-Polymer Chemistry* **1998**, 36, 665-673.
- (16) Andrzejewska, E. Photopolymerization Kinetics of Multifunctional Monomers. *Progress in Polymer Science* **2001**, 26, 605-665.
- (17) Hoyle, C. E.; Bowman, C. N. Thiol-Ene Click Chemistry. *Angewandte Chemie-International Edition* **2010**, 49, 1540-1573.
- (18) Studer, K.; Decker, C.; Beck, E.; Schwalm, R. Overcoming Oxygen Inhibition in Uv-Curing of Acrylate Coatings by Carbon Dioxide Inerting, Part I. *Progress in Organic Coatings* **2003**, 48, 92-100.
- (19) Du, Y.; Williams, B. A.; Francis, L. F.; McCormick, A. V. Pulsed Irradiation for High-Throughput Curing Applications. *Progress in Organic Coatings* **2017**, 104, 104-109.
- (20) Hageman, H. J. Photoinitiators for Free-Radical Polymerization. *Progress in Organic Coatings* **1985**, 13, 123-150.
- (21) Xu, F.; Yang, J. L.; Gong, Y. S.; Ma, G. P.; Nie, J. A Fluorinated Photoinitiator for Surface Oxygen Inhibition Resistance. *Macromolecules* **2012**, 45, 1158-1164.
- (22) Baudin, G.; Jung, T., Process for Producing Coatings Using Surface-Active Photoinitiators. Google Patents: 2007.
- (23) El-Roz, M.; Lalevee, J.; Morlet-Savary, F.; Allonas, X.; Fouassier, J. P. Radical and Cationic Photopolymerization: New Pyrylium and Thiopyrylium Salt-Based Photoinitiating Systems. *Journal of Polymer Science Part a-Polymer Chemistry* **2008**, 46, 7369-7375.
- (24) Lalevee, J.; Morlet-Savary, F.; El Roz, M.; Allonas, X.; Fouassier, J. P. Thiyl Radical Generation in Thiol or Disulfide Containing Photosensitive Systems. *Macromolecular Chemistry and Physics* **2009**, 210, 311-319.
- (25) Matsushima, H.; Shin, J.; Bowman, C. N.; Hoyle, C. E. Thiol-Isocyanate-Acrylate Ternary Networks by Selective Thiol-Click Chemistry. *Journal of Polymer Science Part a-Polymer Chemistry* **2010**, 48, 3255-3264.
- (26) Green, W. A., *Industrial Photoinitiators: A Technical Guide*. CRC Press: 2010.
- (27) Wen, M.; Scriven, L. E.; McCormick, A. V. Differential Scanning Calorimetry and Cantilever Deflection Studies of Polymerization Kinetics and Stress in Ultraviolet Curing of Multifunctional (Meth)Acrylate Coatings. *Macromolecules* **2002**, 35, 112-120.
- (28) Vaessen, D. M.; Ngantung, F. A.; Palacio, M. L. B.; Francis, L. F.; McCormick, A. V. Effect of Lamp Cycling on Conversion and Stress Development in Ultraviolet-Cured Acrylate Coatings. *Journal of Applied Polymer Science* **2002**, 84, 2784-2793.

- (29) Song, J. O.; McCormick, A. V.; Francis, L. F. Depthwise Viscosity Gradients in Uv-Cured Epoxy Coatings. *Macromolecular Materials and Engineering* **2013**, 298, 145-152.
- (30) Allen, N. S. Photoinitiators for Uv and Visible Curing of Coatings: Mechanisms and Properties. *Journal of Photochemistry and Photobiology a-Chemistry* **1996**, 100, 101-107.
- (31) Decker, C. Kinetic-Study of Light-Induced Polymerization by Real-Time Uv and Ir Spectroscopy. *Journal of Polymer Science Part a-Polymer Chemistry* **1992**, 30, 913-928.
- (32) Sangermano, M.; Razza, N.; Crivello, J. V. Cationic Uv-Curing: Technology and Applications. *Macromolecular Materials and Engineering* **2014**, 299, 775-793.
- (33) Li, T.; Heinzer, M. J.; Redline, E. M.; Zuo, F.; Bates, F. S.; Francis, L. F. Microstructure and Performance of Block Copolymer Modified Epoxy Coatings. *Progress in Organic Coatings* **2014**, 77, 1145-1154.
- (34) Senyurt, A. F.; Wei, H. Y.; Hoyle, C. E.; Piland, S. G.; Gould, T. E. Ternary Thiol-Ene/Acrylate Photopolymers: Effect of Acrylate Structure on Mechanical Properties. *Macromolecules* **2007**, 40, 4901-4909.
- (35) Reddy, S. K.; Okay, O.; Bowman, C. N. Network Development in Mixed Step-Chain Growth Thiol-Vinyl Photopolymerizations. *Macromolecules* **2006**, 39, 8832-8843.
- (36) Northrop, B. H.; Coffey, R. N. Thiol-Ene Click Chemistry: Computational and Kinetic Analysis of the Influence of Alkene Functionality. *Journal of the American Chemical Society* **2012**, 134, 13804-13817.
- (37) Jin, K. L.; Wilmot, N.; Heath, W. H.; Torkelson, J. M. Phase-Separated Thiol-Epoxy-Acrylate Hybrid Polymer Networks with Controlled Cross-Link Density Synthesized by Simultaneous Thiol-Acrylate and Thiol-Epoxy Click Reactions. *Macromolecules* **2016**, 49, 4115-4123.
- (38) Jin, K. L.; Heath, W. H.; Torkelson, J. M. Kinetics of Multifunctional Thiol-Epoxy Click Reactions Studied by Differential Scanning Calorimetry: Effects of Catalysis and Functionality. *Polymer* **2015**, 81, 70-78.
- (39) Prasath, R. A.; Gokmen, M. T.; Espeel, P.; Du Prez, F. E. Thiol-Ene and Thiol-Yne Chemistry in Microfluidics: A Straightforward Method Towards Macroporous and Nonporous Functional Polymer Beads. *Polymer Chemistry* **2010**, 1, 685-692.
- (40) Carlborg, C. F.; Haraldsson, T.; Oberg, K.; Malkoch, M.; van der Wijngaart, W. Beyond Pdms: Off-Stoichiometry Thiol-Ene (Oste) Based Soft Lithography for Rapid Prototyping of Microfluidic Devices. *Lab on a Chip* **2011**, 11, 3136-3147.

- (41) Lin, H.; Wan, X.; Jiang, X. S.; Wang, Q. K.; Yin, J. A Nanoimprint Lithography Hybrid Photoresist Based on the Thiol-Ene System. *Advanced Functional Materials* **2011**, 21, 2960-2967.
- (42) Hagberg, E. C.; Malkoch, M.; Ling, Y. B.; Hawker, C. J.; Carter, K. R. Effects of Modulus and Surface Chemistry of Thiol-Ene Photopolymers in Nanoimprinting. *Nano Letters* **2007**, 7, 233-237.
- (43) Campos, L. M.; Truong, T. T.; Shim, D. E.; Dimitriou, M. D.; Shir, D.; Meinel, I.; Gerbec, J. A.; Hahn, H. T.; Rogers, J. A.; Hawker, C. J. Applications of Photocurable Pmms Thiol-Ene Stamps in Soft Lithography. *Chemistry of Materials* **2009**, 21, 5319-5326.
- (44) Decker, C. Kinetic Study and New Applications of Uv Radiation Curing. *Macromolecular Rapid Communications* **2002**, 23, 1067-1093.
- (45) Rutsch, W.; Dietliker, K.; Leppard, D.; Kohler, M.; Misev, L.; Kolczak, U.; Rist, G. Recent Developments in Photoinitiators. *Progress in Organic Coatings* **1996**, 27, 227-239.
- (46) Goodner, M. D.; Lee, H. R.; Bowman, C. N. Method for Determining the Kinetic Parameters in Diffusion-Controlled Free-Radical Homopolymerizations. *Industrial & Engineering Chemistry Research* **1997**, 36, 1247-1252.
- (47) Francis, L. F.; McCormick, A. V.; Vaessen, D. M.; Payne, J. A. Development and Measurement of Stress in Polymer Coatings. *Journal of Materials Science* **2002**, 37, 4717-4731.
- (48) Kostov, G.; Holan, M.; Ameduri, B.; Hung, M. H. Synthesis and Characterizations of Photo-Cross-Linkable Telechelic Diacrylate Poly(Vinylidene Fluoride-Co-Perfluoromethyl Vinyl Ether) Copolymers. *Macromolecules* **2012**, 45, 7375-7387.
- (49) Yu, Q.; Nauman, S.; Santerre, J. P.; Zhu, S. Uv Photopolymerization Behavior of Dimethacrylate Oligomers with Camphorquinone/Amine Initiator System. *Journal of Applied Polymer Science* **2001**, 82, 1107-1117.
- (50) Jindal, K.; Bhattacharya, D.; Francis, L. F.; McCormick, A. V.; Germinario, L. T.; Williams, C. Structure and Property Development During Solidification of Voc Compliant Automotive Refinish Clearcoats. *Progress in Organic Coatings* **2010**, 67, 296-301.
- (51) Decker, C.; Moussa, K. Photopolymerization of Multifunctional Polymers .5. Polyurethane-Acylate Resins. *European Polymer Journal* **1991**, 27, 881-889.
- (52) Decker, C.; Moussa, K. Photopolymerization of Multifunctional Monomers in Condensed Phase. *Journal of Applied Polymer Science* **1987**, 34, 1603-1618.
- (53) Kloosterboer, J. G.; Vandehei, G. M. M.; Gossink, R. G.; Dortant, G. C. M. The Effects of Volume Relaxation and Thermal Mobilization of Trapped Radicals on the Final Conversion of Photopolymerized Diacrylates. *Polymer Communications* **1984**, 25, 322-325.

- (54) Bowman, C. N.; Peppas, N. A. Coupling of Kinetics and Volume Relaxation During Polymerizations of Multiacrylates and Multimethacrylates. *Macromolecules* **1991**, 24, 1914-1920.
- (55) Decker, C.; Decker, D.; Morel, F., Light Intensity and Temperature Effect in Photoinitiated Polymerization. In *Photopolymerization: Fundamentals and Applications*, Scranton, A. B.; Bowman, C. N.; Peiffer, R. W., Eds. Amer Chemical Soc: Washington, 1997; Vol. 673, pp 63-80.
- (56) Decker, C.; Elzaouk, B.; Decker, D. Kinetic Study of Ultrafast Photopolymerization Reactions. *Journal of Macromolecular Science-Pure and Applied Chemistry* **1996**, A33, 173-190.
- (57) Gauthier, M. A.; Stangel, I.; Ellis, T. H.; Zhu, X. X. Oxygen Inhibition in Dental Resins. *Journal of Dental Research* **2005**, 84, 725-729.
- (58) Belon, C.; Allonas, X.; Croutxe-Barghorn, C.; Lalevee, J. Overcoming the Oxygen Inhibition in the Photopolymerization of Acrylates: A Study of the Beneficial Effect of Triphenylphosphine. *Journal of Polymer Science Part a-Polymer Chemistry* **2010**, 48, 2462-2469.
- (59) Bolon, D. A.; Webb, K. K. Barrier Coats Versus Inert Atmospheres - Elimination of Oxygen Inhibition in Free-Radical Polymerizations. *Journal of Applied Polymer Science* **1978**, 22, 2543-2551.
- (60) Yang, Y.; Mielczarek, K.; Aryal, M.; Zakhidov, A.; Hu, W. Nanoimprinted Polymer Solar Cell. *Acs Nano* **2012**, 6, 2877-2892.
- (61) Mahajan, A.; Hyun, W. J.; Walker, S. B.; Rojas, G. A.; Choi, J. H.; Lewis, J. A.; Francis, L. F.; Frisbie, C. D. A Self-Aligned Strategy for Printed Electronics: Exploiting Capillary Flow on Microstructured Plastic Surfaces. *Advanced Electronic Materials* **2015**, 1, 9.
- (62) Ahn, S.; Choi, M.; Bae, H.; Lim, J.; Myung, H.; Kim, H.; Kang, S. Design and Fabrication of Micro Optical Film by Ultraviolet Roll Imprinting. *Japanese Journal of Applied Physics Part 1-Regular Papers Brief Communications & Review Papers* **2007**, 46, 5478-5484.
- (63) Quere, D., Wetting and Roughness. In *Annual Review of Materials Research*, 2008; Vol. 38, pp 71-99.
- (64) Wang, L.; Yang, C. H.; Gai, S.; Wen, J. Current Status and Future Prospects of Conventional Recording Technologies for Mass Storage Applications. *Current Nanoscience* **2014**, 10, 638-659.
- (65) Zhang, Q.; Xu, J.; Song, Q.; Li, N.; Zhang, Z. L.; Li, K. Y.; Du, Y. Y.; Wu, L. Q.; Tang, M. L.; Liu, L. W.; Cheng, G. S.; Liu, J. Synthesis of Amphiphilic Reduced Graphene Oxide with an Enhanced Charge Injection Capacity for Electrical Stimulation of Neural Cells. *Journal of Materials Chemistry B* **2014**, 2, 4331-4337.

- (66) Olson, J.; Manjavacas, A.; Basu, T.; Huang, D.; Schlather, A. E.; Zheng, B.; Halas, N. J.; Nordlander, P.; Link, S. High Chromaticity Aluminum Plasmonic Pixels for Active Liquid Crystal Displays. *Acs Nano* **2016**, 10, 1108-1117.
- (67) Hiltunen, J.; Hiltunen, M.; Puustinen, J.; Lappalainen, J.; Karioja, P. Fabrication of Optical Waveguides by Imprinting: Usage of Positive Tone Resist as a Mould for Uv-Curable Polymer. *Optics Express* **2009**, 17, 22813-22822.
- (68) Chang, C. Y.; Yang, S. Y.; Huang, L. S.; Hsieh, K. H. Fabrication of Polymer Microlens Arrays Using Capillary Forming with a Soft Mold of Micro-Holes Array and Uv-Curable Polymer. *Optics Express* **2006**, 14, 6253-6258.
- (69) Abu Talip, N. B.; Taniguchi, J. Fabrication of Self-Supporting Antireflection-Structured Film by Uv-Nil. *Microelectronic Engineering* **2013**, 110, 163-166.
- (70) Liu, C. H.; Sung, C. K.; Chang, E. C.; Lo, C. Y.; Fu, C. C. Fabricating a Silver Soft Mold on a Flexible Substrate for Roll-to-Roll Nanoimprinting. *Ieee Transactions on Nanotechnology* **2014**, 13, 80-84.
- (71) Langer, R.; Peppas, N. A. Advances in Biomaterials, Drug Delivery, and Bionanotechnology. *Aiche Journal* **2003**, 49, 2990-3006.
- (72) Sun, Q.; Lv, Z. F.; Du, Y. Y.; Wu, Q. M.; Wang, L.; Zhu, L. F.; Meng, X. J.; Chen, W. Z.; Xiao, F. S. Recyclable Porous Polymer-Supported Copper Catalysts for Glaser and Huisgen 1,3-Diolar Cycloaddition Reactions. *Chemistry-an Asian Journal* **2013**, 8, 2822-2827.
- (73) Liu, S. J.; Roeder, G.; Aygun, G.; Motzek, K.; Evanschitzky, P.; Erdmann, A. Simulation of 3d Inclined/Rotated Uv Lithography and Its Application to Microneedles. *Optik* **2012**, 123, 928-931.
- (74) Takahashi, H.; Heo, Y. J.; Arakawa, N.; Kan, T.; Matsumoto, K.; Kawano, R.; Shimoyama, I. Scalable Fabrication of Microneedle Arrays Via Spatially Controlled Uv Exposure. *Microsystems & Nanoengineering* **2016**, 2.
- (75) Soper, S. A.; Brown, K.; Ellington, A.; Frazier, B.; Garcia-Manero, G.; Gau, V.; Gutman, S. I.; Hayes, D. F.; Korte, B.; Landers, J. L.; Larson, D.; Ligler, F.; Majumdar, A.; Mascini, M.; Nolte, D.; Rosenzweig, Z.; Wang, J.; Wilson, D. Point-of-Care Biosensor Systems for Cancer Diagnostics/Prognostics. *Biosensors & Bioelectronics* **2006**, 21, 1932-1942.
- (76) Chan-Park, M. B.; Yan, Y. H.; Neo, W. K.; Zhou, W. X.; Zhang, J.; Yue, C. Y. Fabrication of High Aspect Ratio Poly(Ethylene Glycol)-Containing Microstructures by Uv Embossing. *Langmuir* **2003**, 19, 4371-4380.
- (77) Jouane, Y.; Enami, Y. Nanolayer-Transfer Method of Tio2 Slot Layers and Its Application for Fabricating Hybrid Electro-Optic Polymer/Tio2 Vertical Slot Waveguide Modulators. *Optics and Laser Technology* **2017**, 94, 146-153.
- (78) Ahn, S. H.; Guo, L. J. Large-Area Roll-to-Roll and Roll-to-Plate Nanoimprint Lithography: A Step toward High-Throughput Application of Continuous Nanoimprinting. *Acs Nano* **2009**, 3, 2304-2310.

- (79) Mahajan, A.; Hyun, W. J.; Walker, S. B.; Lewis, J. A.; Francis, L. F.; Frisbie, C. D. High-Resolution, High-Aspect Ratio Conductive Wires Embedded in Plastic Substrates. *Acs Applied Materials & Interfaces* **2015**, 7, 1841-1847.
- (80) Hyun, W. J.; Secor, E. B.; Rojas, G. A.; Hersam, M. C.; Francis, L. F.; Frisbie, C. D. All-Printed, Foldable Organic Thin-Film Transistors on Glassine Paper. *Advanced Materials* **2015**, 27, 7058-+.
- (81) Bartels, R. A.; Paul, A.; Green, H.; Kapteyn, H. C.; Murnane, M. M.; Backus, S.; Christov, I. P.; Liu, Y. W.; Attwood, D.; Jacobsen, C. Generation of Spatially Coherent Light at Extreme Ultraviolet Wavelengths. *Science* **2002**, 297, 376-378.
- (82) Schiff, H. Nanoimprint Lithography: An Old Story in Modern Times? A Review. *Journal of Vacuum Science & Technology B* **2008**, 26, 458-480.
- (83) Guo, L. J. Nanoimprint Lithography: Methods and Material Requirements. *Advanced Materials* **2007**, 19, 495-513.
- (84) Quan, C.; Tay, C. J.; Chen, W. Determination of Displacement Derivative in Digital Holographic Interferometry. *Optics Communications* **2009**, 282, 809-815.
- (85) Chu, Z. L.; Seeger, S. Superamphiphobic Surfaces. *Chemical Society Reviews* **2014**, 43, 2784-2798.
- (86) Qiao, W.; Huang, W. B.; Liu, Y. H.; Li, X. M.; Chen, L. S.; Tang, J. X. Toward Scalable Flexible Nanomanufacturing for Photonic Structures and Devices. *Advanced Materials* **2016**, 28, 10353-10380.
- (87) Zhang, J.; Shen, S.; Dong, X. X.; Chen, L. S. Low-Cost Fabrication of Large Area Sub-Wavelength Anti-Reflective Structures on Polymer Film Using a Soft Pua Mold. *Optics Express* **2014**, 22, 1842-1851.
- (88) Seubert, C. M.; Nichols, M. E. Alternative Curing Methods of Uv Curable Automotive Clearcoats. *Progress in Organic Coatings* **2004**, 49, 218-224.
- (89) Kim, H. S.; Dhage, S. R.; Shim, D. E.; Hahn, H. T. Intense Pulsed Light Sintering of Copper Nanoink for Printed Electronics. *Applied Physics a-Materials Science & Processing* **2009**, 97, 791-798.
- (90) Stropp, J. P.; Wolff, U.; Kernaghan, S.; Loffler, H.; Osterhold, M.; Thomas, H. Uv Curing Systems for Automotive Refinish Applications. *Progress in Organic Coatings* **2006**, 55, 201-205.
- (91) Maag, K.; Lenhard, W.; Loffles, H. New Uv Curing Systems for Automotive Applications. *Progress in Organic Coatings* **2000**, 40, 93-97.
- (92) Riggs, B. C.; Elupula, R.; Grayson, S. M.; Chrissey, D. B. Photonic Curing of Aromatic Thiol-Ene Click Dielectric Capacitors Via Inkjet Printing. *Journal of Materials Chemistry A* **2014**, 2, 17380-17386.
- (93) Cui, H. W.; Jiu, J. T.; Nagao, S.; Sugahara, T.; Suganuma, K.; Uchida, H.; Schroder, K. A. Ultra-Fast Photonic Curing of Electrically Conductive Adhesives

Fabricated from Vinyl Ester Resin and Silver Micro-Flakes for Printed Electronics. *Rsc Advances* **2014**, 4, 15914-15922.

(94) Green, W. A., *Industrial Photoinitiators : A Technical Guide*. Boca Raton : CRC Press: Boca Raton, 2010.

(95) [Http://Www.Internationalcrystal.Net/Optics_16.Htm](http://Www.Internationalcrystal.Net/Optics_16.Htm).

(96) Decker, C.; Moussa, K. A New Method for Monitoring Ultra-Fast Photopolymerizations by Real-Time Infrared (Rtir) Spectroscopy. *Makromolekulare Chemie-Macromolecular Chemistry and Physics* **1988**, 189, 2381-2394.

(97) Johansson, M.; Hult, A. Synthesis, Characterization, and Uv Curing of Acrylate Functional Hyperbranched Polyester Resins. *Journal of Coatings Technology* **1995**, 67, 35-39.

(98) Williams, B. A.; Smeaton, M. A.; Holgate, C. S.; Trejo, N. D.; Francis, L. F.; Aydil, E. Intense Pulsed Light Annealing of Copper Zinc Tin Sulfide Nanocrystal Coatings. *J. Vac. Sci and Tech. in review*

(99) Bowman, C. N.; Kloxin, C. J. Toward an Enhanced Understanding and Implementation of Photopolymerization Reactions. *Aiche Journal* **2008**, 54, 2775-2795.

(100) Payne, J. A.; Francis, L. F.; McCormick, A. V. The Effects of Processing Variables on Stress Development in Ultraviolet-Cured Coatings. *Journal of Applied Polymer Science* **1997**, 66, 1267-1277.

(101) Charlot, V.; Ibrahim, A.; Allonas, X.; Croutxe-Barghorn, C.; Delaite, C. Photopolymerization of Methyl Methacrylate: Effects of Photochemical and Photonic Parameters on the Chain Length. *Polymer Chemistry* **2014**, 5, 6236-6243.

(102) Chandra, D.; Crosby, A. J. Self-Wrinkling of Uv-Cured Polymer Films. *Adv. Mater.* **2011**, 23, 3441-3445.

(103) Basu, S. K.; Scriven, L. E.; Francis, L. F.; McCormick, A. V. Mechanism of Wrinkle Formation in Curing Coatings. *Prog. Org. Coat.* **2005**, 53, 1-16.

(104) Chattopadhyay, S.; Huang, Y. F.; Jen, Y. J.; Ganguly, A.; Chen, K. H.; Chen, L. C. Anti-Reflecting and Photonic Nanostructures. *Mater. Sci. Eng. R-Rep.* **2010**, 69, 1-35.

(105) Li, X. M.; Reinhoudt, D.; Crego-Calama, M. What Do We Need for a Superhydrophobic Surface? A Review on the Recent Progress in the Preparation of Superhydrophobic Surfaces. *Chem. Soc. Rev.* **2007**, 36, 1350-1368.

(106) Xia, Y. N.; Rogers, J. A.; Paul, K. E.; Whitesides, G. M. Unconventional Methods for Fabricating and Patterning Nanostructures. *Chemical Reviews* **1999**, 99, 1823-1848.

- (107) Dumond, J. J.; Low, H. Y. Recent Developments and Design Challenges in Continuous Roller Micro- and Nanoimprinting. *Journal of Vacuum Science & Technology B* **2012**, 30, 28.
- (108) Ok, J. G.; Ahn, S. H.; Kwak, M. K.; Guo, L. J. Continuous and High-Throughput Nanopatterning Methodologies Based on **Mechanical Deformation**. *Journal of Materials Chemistry C* **2013**, 1, 7681-7691.
- (109) Yi, P. Y.; Wu, H.; Zhang, C. P.; Peng, L. F.; Lai, X. M. Roll-to-Roll Uv Imprinting Lithography for Micro/Nanostructures. *Journal of Vacuum Science & Technology B* **2015**, 33, 23.
- (110) Thesen, M. W.; Ruttloff, S.; Limberg, R. P. F.; Vogler, M.; Nees, D.; Grutzner, G. Photo-Curable Resists for Inkjet Dispensing Applied in Large Area and High Throughput Roll-to-Roll Nanoimprint Processes. *Microelectronic Engineering* **2014**, 123, 121-125.
- (111) Choi, S. J.; Kim, H. N.; Bae, W. G.; Suh, K. Y. Modulus- and Surface Energy-Tunable Ultraviolet-Curable Polyurethane Acrylate: Properties and Applications. *Journal of Materials Chemistry* **2011**, 21, 14325-14335.
- (112) Cheng, X.; Guo, L. J.; Fu, P. F. Room-Temperature, Low-Pressure Nanoimprinting Based on Cationic Photopolymerization of Novel Epoxysilicone Monomers. *Advanced Materials* **2005**, 17, 1419-+.
- (113) Kasprzak, S. E.; Martin, B.; Raj, T.; Gall, K. Synthesis and Thermomechanical Behavior of (Qua)Ternary Thiol-Ene(/Acrylate) Copolymers. *Polymer* **2009**, 50, 5549-5558.
- (114) Campos, L. M.; Meinel, I.; Guino, R. G.; Schierhorn, M.; Gupta, N.; Stucky, G. D.; Hawker, C. J. Highly Versatile and Robust Materials for Soft Imprint Lithography Based on Thiol-Ene Click Chemistry. *Advanced Materials* **2008**, 20, 3728-+.
- (115) Lin, H.; Wan, X.; Jiang, X. S.; Wang, Q. K.; Yin, J. A "Thiol-Ene" Photo-Curable Hybrid Fluorinated Resist for the High-Performance Replica Mold of Nanoimprint Lithography (Nil). *Journal of Materials Chemistry* **2012**, 22, 2616-2623.
- (116) Leitgeb, M.; Nees, D.; Ruttloff, S.; Palfinger, U.; Gotz, J.; Liska, R.; Belegatis, M. R.; Stadlober, B. Multilength Scale Patterning of Functional Layers by Roll-to-Roll Ultraviolet-Light Assisted Nanoimprint Lithography. *Acs Nano* **2016**, 10, 4926-4941.
- (117) Kim, B. G.; Jeong, E. J.; Kwon, K. H.; Yoo, Y. E.; Choi, D. S.; Kim, J. Controlling Mold Releasing Propensity-the Role of Surface Energy and a Multiple Chain Transfer Agent. *Acs Applied Materials & Interfaces* **2012**, 4, 3465-3470.
- (118) Kawata, H.; Ishihara, J.; Tanabe, T.; Yasuda, M.; Hirai, Y. A Consideration of Important Factor on Demolding Force for Various Molds. *Journal of Photopolymer Science and Technology* **2012**, 25, 223-226.

- (119) Shiotsu, T.; Uemura, K.; Tochino, T.; Ooi, S.; Onishi, Y.; Yasuda, M.; Kawata, H.; Kobayashi, T.; Hirai, Y. Simulation of the Template Release Process Based on Fracture Mechanics in Nanoimprint Lithography. *Microelectronic Engineering* **2014**, 123, 105-111.
- (120) Poulard, C.; Restagno, F.; Weil, R.; Leger, L. Mechanical Tuning of Adhesion through Micro-Patterning of Elastic Surfaces. *Soft Matter* **2011**, 7, 2543-2551.
- (121) Lee, T. Y.; Smith, Z.; Reddy, S. K.; Cramer, N. B.; Bowman, C. N. Thiol-Allyl Ether-Methacrylate Ternary Systems. Polymerization Mechanism. *Macromolecules*. **2007**, 40, 1466-1472.
- (122) Gan, Y. C.; Yin, J.; Jiang, X. S. Self-Wrinkling Induced by the Photopolymerization and Self-Assembly of Fluorinated Polymer at Air/Liquid Interface. *Journal of Materials Chemistry A* **2014**, 2, 18574-18582.
- (123) Cramer, N. B.; Bowman, C. N. Kinetics of Thiol-Ene and Thiol-Acrylate Photopolymerizations with Real-Time Fourier Transform Infrared. *Journal of Polymer Science Part a-Polymer Chemistry* **2001**, 39, 3311-3319.
- (124) Matthew, E. D.; David, E. H. Analysis and Characterization of Demolding of Hot Embossed Polymer Microstructures. *Journal of Micromechanics and Microengineering* **2011**, 21, 085024.
- (125) Li, Q.; Zhou, H.; Hoyle, C. E. The Effect of Thiol and Ene Structures on Thiol-Ene Networks: Photopolymerization, Physical, Mechanical and Optical Properties. *Polymer* **2009**, 50, 2237-2245.
- (126) Yoo, P. J.; Choi, S. J.; Kim, J. H.; Suh, D.; Baek, S. J.; Kim, T. W.; Lee, H. H. Unconventional Patterning with a Modulus-Tunable Mold: From Imprinting to Microcontact Printing. *Chemistry of Materials* **2004**, 16, 5000-5005.
- (127) Dietlin, C.; Schweizer, S.; Xiao, P.; Zhang, J.; Morlet-Savary, F.; Graff, B.; Fouassier, J. P.; Lalevee, J. Photopolymerization Upon Leds: New Photoinitiating Systems and Strategies. *Polymer Chemistry* **2015**, 6, 3895-3912.
- (128) Hiemenz, P. C., *Polymer Chemistry*. 2nd ed. ed.; Boca Raton, FL : CRC Press: Boca Raton, FL, 2007.
- (129) Jackson, C.; Chen, Y. J.; Mays, J. W. Size Exclusion Chromatography with Multiple Detectors: Solution Properties of Linear Chains of Varying Flexibility in Tetrahydrofuran. *Journal of Applied Polymer Science* **1996**, 61, 865-874.
- (130) Xiong, L.; Kendrick, L. L.; Heusser, H.; Webb, J. C.; Sparks, B. J.; Goetz, J. T.; Guo, W.; Stafford, C. M.; Blanton, M. D.; Nazarenko, S.; Patton, D. L. Spray-Deposition and Photopolymerization of Organic-Inorganic Thiol-Ene Resins for Fabrication of Superamphiphobic Surfaces. *Acs Applied Materials & Interfaces* **2014**, 6, 10763-10774.
- (131) Vitale, A.; Bongiovanni, R.; Ameduri, B. Fluorinated Oligomers and Polymers in Photopolymerization. *Chemical Reviews* **2015**, 115, 8835-8866.

- (132) Yoshida, N.; Abe, Y.; Shigeta, H.; Nakajima, A.; Ohsaki, H.; Hashimoto, K.; Watanabe, T. Sliding Behavior of Water Droplets on Flat Polymer Surface. *Journal of the American Chemical Society* **2006**, 128, 743-747.
- (133) Thomas, R. R.; Anton, D. R.; Graham, W. F.; Darmon, M. J.; Sauer, B. B.; Stika, K. M.; Swartzfager, D. G. Preparation and Surface Properties of Acrylic Polymers Containing Fluorinated Monomers. *Macromolecules* **1997**, 30, 2883-2890.
- (134) Pinto, G.; de Abreu, C. A. M.; Knoechelmann, A.; de Almeida, Y. M. B. Effect of the Corona Treatment and of the 1,4-Cyclohexanedimethanol on the Surface Characteristics of the Poly(Ethylene Terephthalate) Film. *Macromolecular Symposia* **1999**, 148, 333-343.
- (135) Williams, S. S.; Retterer, S.; Lopez, R.; Ruiz, R.; Samulski, E. T.; DeSimone, J. M. High-Resolution Pfp-Based Molding Techniques for Nanofabrication of High-Pattern Density, Sub-20 Nm Features: A Fundamental Materials Approach. *Nano Letters* **2010**, 10, 1421-1428.
- (136) Mulazim, Y.; Cakmakci, E.; Kahraman, M. V. Properties of Thiol-Ene Photocurable Highly Hydrophobic and Oleophobic Nanocomposite Coatings on Abs and Hips Substrates. *Advances in Polymer Technology* **2013**, 32, E416-E426.
- (137) Johnston, I. D.; McCluskey, D. K.; Tan, C. K. L.; Tracey, M. C. Mechanical Characterization of Bulk Sylgard 184 for Microfluidics and Microengineering. *Journal of Micromechanics and Microengineering* **2014**, 24.
- (138) Ahn, S. H.; Guo, L. J. High-Speed Roll-to-Roll Nanoimprint Lithography on Flexible Plastic Substrates. *Advanced Materials* **2008**, 20, 2044-+.
- (139) John, J.; Tang, Y. Y.; Rothstein, J. P.; Watkins, J. J.; Carter, K. R. Large-Area, Continuous Roll-to-Roll Nanoimprinting with Pfp Composite Molds. *Nanotechnology* **2013**, 24.
- (140) Peng, Z.; Wang, C.; Chen, L.; Chen, S. Peeling Behavior of a Viscoelastic Thin-Film on a Rigid Substrate. *International Journal of Solids and Structures* **2014**, 51, 4596-4603.
- (141) Wu, H.; Gao, J.; Yi, P. Y.; Peng, L. F.; Lai, X. M. Investigation of Reflective Performance for Micro-Pyramid Arrays by Roll-to-Roll Uv Imprinting Process. *Microelectronic Engineering* **2017**, 182, 61-67.
- (142) John, J.; Tang, Y. Y.; Rothstein, J. P.; Watkins, J. J.; Carter, K. R. Large-Area, Continuous Roll-to-Roll Nanoimprinting with Pfp Composite Molds. *Nanotechnology* **2013**, 24, 9.
- (143) John, J.; Muthee, M.; Yogeesh, M.; Yngvesson, S. K.; Carter, K. R. Suspended Multiwall Carbon Nanotube-Based Infrared Sensors Via Roll-to-Roll Fabrication. *Advanced Optical Materials* **2014**, 2, 581-587.
- (144) Du, Y.; Xu, J.; Sakizadeh, J. D.; Weiblen, D. G.; McCormick, A. V.; Francis, L. F. Modulus- and Surface-Energy-Tunable Thiol-Ene for Uv

Micromolding of Coatings. *ACS Applied Materials & Interfaces* **2017**, 9, 24976-24986.

(145) Du, Y. Y.; Xu, J.; Sakizadeh, J.; McCormick, A.; Francis, L. Scalable Fabrication of Microstructured Coatings with Thiol-Ene Photopolymers and Uv Led Curing. *Abstracts of Papers of the American Chemical Society* **2017**, 254.

(146) Li, Y. Y.; John, J.; Kolewe, K. W.; Schiffman, J. D.; Carter, K. R. Scaling up Nature: Large Area Flexible Biomimetic Surfaces. *Acs Applied Materials & Interfaces* **2015**, 7, 23439-23444.

(147) Lichte, Y.; Wonnemann, H., Coating Material Which Is Thermally Curable and Curable by Means of Actinic Radiation and Method for Coating Microporous Surfaces. Google Patents: 2007.

(148) Hong, J. W.; Cheon, H. K.; Kim, S. H.; Hwang, K. H.; Kim, H. K. Synthesis and Characterization of Uv Curable Urethane Acrylate Oligomers Containing Ammonium Salts for Anti-Fog Coatings. *Progress in Organic Coatings* **2017**, 110, 122-127.

(149) Vyatskikh, A.; Kudo, A.; Delalande, S.; Greer, J. R. Additive Manufacturing of Polymer-Derived Titania for One-Step Solar Water Purification. *Materials Today Communications* **2018**, 15, 288-293.

(150) O'Brien, A. K.; Cramer, N. B.; Bowman, C. N. Oxygen Inhibition in Thiol-Acrylate Photopolymerizations. *Journal of Polymer Science Part a-Polymer Chemistry* **2006**, 44, 2007-2014.

(151) Golaz, B.; Michaud, V.; Leterrier, Y.; Manson, J. A. E. Uv Intensity, Temperature and Dark-Curing Effects in Cationic Photo-Polymerization of a Cycloaliphatic Epoxy Resin. *Polymer* **2012**, 53, 2038-2048.

(152) McNair, O. D.; Sparks, B. J.; Janisse, A. P.; Brent, D. P.; Patton, D. L.; Savin, D. A. Highly Tunable Thiol-Ene Networks Via Dual Thiol Addition. *Macromolecules* **2013**, 46, 5614-5621.

(153) Roppolo, I.; Bozzo, A. D.; Castellino, M.; Chiappone, A.; Perrone, D.; Bejtka, K.; Bocchini, S.; Sangermano, M.; Chiolerio, A. Dual Step Irradiation Process for in Situ Generation and Patterning of Silver Nanoparticles in a Photocured Film. *Rsc Advances* **2016**, 6, 14832-14843.

(154) Nazar, R.; Ronchetti, S.; Roppolo, I.; Sangermano, M.; Bongiovanni, R. M. In Situ Synthesis of Polymer Embedded Silver Nanoparticles Via Photopolymerization. *Macromolecular Materials and Engineering* **2015**, 300, 226-233.

(155) Fantino, E.; Chiappone, A.; Roppolo, I.; Manfredi, D.; Bongiovanni, R.; Pirri, C. F.; Calignano, F. 3d Printing of Conductive Complex Structures with in Situ Generation of Silver Nanoparticles. *Advanced Materials* **2016**, 28, 3712-3717.

- (156) Sangermano, M.; Yagci, Y.; Rizza, G. In Situ Synthesis of Silver-Epoxy Nanocomposites by Photoinduced Electron Transfer and Cationic Polymerization Processes. *Macromolecules* **2007**, 40, 8827-8829.
- (157) Abdali, Z.; Yeganeh, H.; Solouk, A.; Gharibi, R.; Sorayya, M. Thermoresponsive Antimicrobial Wound Dressings Via Simultaneous Thiol-Ene Polymerization and in Situ Generation of Silver Nanoparticles. *Rsc Advances* **2015**, 5, 66024-66036.
- (158) Fang, Y. C.; Ha, H.; Shanmuganathan, K.; Ellison, C. J. Polyhedral Oligomeric Silsesquioxane-Containing Thiol-Ene Fibers with Tunable Thermal and Mechanical Properties. *Acs Applied Materials & Interfaces* **2016**, 8, 11050-11059.
- (159) Lan, H. B.; Liu, H. Z. Uv-Nanoimprint Lithography: Structure, Materials and Fabrication of Flexible Molds. *Journal of Nanoscience and Nanotechnology* **2013**, 13, 3145-3172.
- (160) Choi, S.; Kook, Y.; Kim, C.; Yoo, S.; Park, K. S.; Kim, S. M.; Kang, S. The Effect of Mold Materials on the Overlay Accuracy of a Roll-to-Roll Imprinting System Using Uv Led Illumination within a Transparent Mold. *Journal of Micromechanics and Microengineering* **2016**, 26.
- (161) Kim, H. J.; Almanza-Workman, M.; Garcia, B.; Kwon, O.; Jeffrey, F.; Braymen, S.; Hauschildt, J.; Junge, K.; Larson, D.; Stieler, D.; Chaiken, A.; Cobene, B.; Elder, R.; Jackson, W.; Jam, M.; Jeans, A.; Luo, H.; Mei, P.; Perlov, C.; Taussig, C. Roll-to-Roll Manufacturing of Electronics on Flexible Substrates Using Self-Aligned Imprint Lithography (Sail). *Journal of the Society for Information Display* **2009**, 17, 963-970.